MODEL-BASED RANDOMS CORRECTION FOR 3D POSITRON EMISSION TOMOGRAPHY

by

BARRY WILLIAM POINTON

B.Sc., The University of British Columbia, 1985
M.Sc., Simon Fraser University, 1990
Dip.C.S., Regent College, 1996

A THESIS SUBMITTED IN PARTIAL FULFILLMENT OF
THE REQUIREMENTS FOR THE DEGREE OF

DOCTOR OF PHILOSOPHY

in

THE FACULTY OF GRADUATE STUDIES

(Physics)

THE UNIVERSITY OF BRITISH COLUMBIA

April 2007

ABSTRACT

Random coincidences (randoms) are frequently a major source of image degradation and quantitative inaccuracies in positron emission tomography. Randoms occurring in the true coincidence window are commonly corrected for by subtracting the randoms measured in a delayed coincidence window. This requires additional processing demands on the tomograph and increases the noise in the corrected data. A less noisy randoms estimate may be obtained by measuring individual detector singles rates, but few tomographs have this capability. This work describes a new randoms correction method that uses the singles rates from an analytic calculation, rather than measurements. This is a logical and novel extension of the model-based methods presently used for scatter correction.

The singles calculation uses a set of sample points randomly generated within the preliminary reconstructed radioactivity image. The contribution of the activity at each point to the singles rate in every detector is calculated using a single photon detection model, producing an estimate of the singles distribution. This is scaled to the measured global singles rate and used to calculate the randoms distribution which is subtracted from the measured image data.

This method was tested for a MicroPET R4 tomograph. Measured and calculated randoms distributions were compared using count profiles and quantitative figures of merit for a set of phantom and animal studies. Reconstructed images, corrected with measured and calculated randoms, were also analysed.

The calculation reproduced the measured randoms rates to within $\leq 1.4\%$ for all realistic studies. The calculated randoms distributions showed excellent agreement with the measured, except that the calculated sinograms were smooth. Images corrected with both methods showed no significant differences due to biases. However, in the situations tested, no significant difference in the noise level of the reconstructed images was detected due to the low randoms fractions of the acquired data.

The model-based method of randoms correction uses only the measured image data and the global singles rate to produce smooth and accurate random distributions and therefore has much lower demands on the tomograph than other techniques. It is also expected to contribute to noise reduction in situations involving high randoms fraction.

TABLE OF CONTENTS

LIST OF TABLES

LIST OF FIGURES

ACKNOWLEDGMENTS

I would like to especially thank Dr. Vesna Sossi for her guidance, help, and support throughout this long, winding and arduous road. Her keen insights, wise direction and coolness in crisis were invaluable in moving the research, and this thesis, forward. I would also like to thank Dr. Anna Celler, Dr. Alex MacKay and Dr. Tom Ruth for their sage advice and patience in serving on my committee. As well, I would like to thank those at the UBC/TRIUMF PET Physics group for all their assistance and discussions, especially Eric Vandervoort, Marie-Laure Camborde, Siobhan McCormick, Dr. Stephan Blinder, Katie Dinelle, and Dr. Kelvin Raywood. Most helpful for the experimental work were Carolyn English and Caroline Williams and the TRIUMF PET cyclotron group, especially Ken Buckley.

My colleagues at BCIT in the Physics and Nuclear Medicine Technology departments were also supportive and helpful. I am also grateful for the financial support from BCIT through the Applied Research and Development Fund, as well as the BCIT Professional Development Fund.

DEDICATION

This work is dedicated, with love, to my wife Fiona, for her love and longsuffering. It is also dedicated to my two treasures, Isabelle and Lucy, who missed their daddy while he worked so hard. I also offer special thanks to my parents and in-laws for all their help through this academic trial.

εις τον δοξαν θεου

Chapter 1

The Principles of Positron Emission Tomography

1.1 Overview and Motivation

1.1.1 Overview and Motivation of this Work

This thesis describes the investigation of a new approach to randoms correction in positron emission tomography (PET). PET is an advanced medical imaging technology that measures the amount and distribution of a radioactive tracer in a subject using the radiation from positron decays. The accuracy and precision of PET measurements depends on the quantitative corrections that are applied to the data. These corrections are necessary to account for the physical interactions of the emitted radiation in the subject and in the tomograph detectors.

The "randoms correction" is used to remove the counts caused by erroneous coincidence events that degrade the accuracy of PET data. The standard method of randoms correction requires the acquisition and processing of additional data during the PET scan. As well, the correction itself increases the noise in the image data set, reducing the measurement precision. Alternate randoms correction methods have been investigated to minimize the effects of image noise. These generally also require additional data acquisition, storage and processing and may introduce significant biases into the corrected image data.

This new method of randoms correction is based on modeling the physical processes involved in the counting of the erroneous randoms events. A model-based approach is already successfully used for other PET data corrections, such as scatter and normalization, and so model-based randoms correction is a novel and logical extension. This scheme is straightforward, in that it does not require the additional measurements or data storage necessary for the other methods, reducing the hardware requirements for a PET scanner. This correction is applied post-acquisition and therefore does not interfere with the acquisition. As well, the correction produces smooth randoms distributions and should contribute to noise reduction in the image.

1.1.2 Thesis Overview

This thesis first presents the principles and technology of PET imaging and then describes the justification, theory, development and testing of the model-based randoms correction. **Chapter**

One begins with a description of the field of medical imaging and the function and place of PET imaging within it. The basic physical principles of the positron decay, annihilation and detection are then explained in the context of positron imaging. **Chapter Two** describes in detail the dedicated detector systems used for PET imaging. The physical layout, components, features and performance of tomographs are given. These details are incorporated in the detector modeling in the randoms correction calculation, and, therefore, require explanation. The form of the acquired PET data, as well as the quantitative corrections and image reconstruction methods are also discussed, as these may influence the accuracy of the randoms correction. **Chapter Three** explains the basic causes and effects of random coincidences. The commonly used delayed coincidence method is described. Then, current randoms corrections are compared, showing the advantages and disadvantages that need to be addressed in any new randoms correction method.

Chapter Four presents the theory behind the new model-based randoms correction method. The single photon detection model is described. As well, the scaling method and other corrections are discussed. **Chapter Five** details the present implementation of the model-based randoms correction, beginning with an explanation of the algorithm and computer code. Then, the specific tomograph used for testing, the MicroPET R4™, is described, along with ways this specific design is modeled in the calculation. **Chapter Six** describes the experimental phantom and animal measurements used to test randoms correction calculation. The results of the tests and figures of merit used in the validation are then presented. **Chapter Seven** gives a final discussion of the results of the validation tests. The thesis then concludes with a summary of the work and potential future directions.

1.2 The Realm of Medical Imaging

1.2.1 Introduction

The human body is one of the most complex physical systems in the universe. The body consists of many varied dynamic systems which interact with each other and with the environment. The

intricate chemical and biochemical reactions give rise to many apparently unique emergent properties including self-consciousness. The exploration of this beautiful and intricate world is one of the greatest and most rewarding challenges to modern science.

The detailed, systematic study of the human body began with mapping of the large and small morphological and structural characteristics and relationships. These studies, such as those undertaken by Leonardo DaVinci (**Figure 1-1**), belong to the discipline of Anatomy.

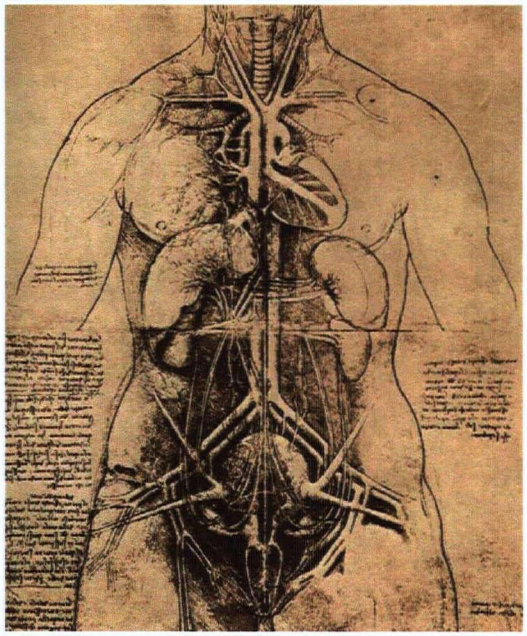

Figure 1-1 Classical anatomical study of a dissected body by Leonardo DaVinci. These dissection studies and sketches showed the beginnings of anatomy as a serious discipline.

Physiology is the study of the macroscopic properties of the dynamic physical and biochemical systems and has been pursued since the late nineteenth century. The microscopic interactions responsible for physiological processes have begun to be investigated in vivo with the use of functional medical imaging devices.

Since the beginning of the twentieth century, imaging techniques have greatly enhanced the study of the systems of the human body for both research and clinical purposes. These include radiography (planar and computed tomography (CT)), magnetic resonance imaging (MRI), ultrasound, standard nuclear medicine (planar and single photon emission computed tomography (SPECT)) and positron emission tomography (PET). These employ complex detector systems, similar to those employed elsewhere in physics and astronomy, each optimized to detect the different types of signals used to probe the physical and chemical characteristics of the human body. The main task of medical imaging is to provide the tools to assist in answering research and clinical questions in anatomy, physiology and pathophysiology. The imaging disciplines also provide interesting and fruitful research questions for radiation and detector physics, as well as image data and information analysis. Thus, medical imaging physics provides a fertile cross-disciplinary field to which physicists have made, and will continue to make, vital contributions.

1.2.2 X-ray, MRI and Ultrasound

The details of medical imaging physics are described in references [1] and [2] with only a short overview provided here.

In radiography, X-rays are produced on one side of the subject by a high efficiency generator tube and detected on the opposite side. The detectors vary in sophistication, from simple photographic film plates to arrays of high pressure Xenon proportional chambers. X-rays interact in the body mainly through photoelectric absorption and Compton scatter, and thus probe the local mass densities and atomic numbers of tissue. The differential attenuation of the X-rays in the non-uniform media of the body may be used to produce simple, qualitative planar images or sophisticated tomographic slice images when CT is employed. Radiographic studies yield mainly anatomic information.

In magnetic resonance imaging, the densities and local environments of the nuclear dipole moments of the constituent atoms in tissue are probed using nuclear magnetic resonance techniques. The subject is placed in a large external magnetic field to align the magnetic moments

and create a magnetization vector. A spin flip or sequence of spin flips is induced in one nuclear species, usually ^1H, by the application of an external radiofrequency (RF) pulse(s) at the appropriate resonance frequency. Relaxation spin-flips then induce a signal in the RF coils that depends on the local ^1H densities, due, for example, to H_2O or lipids. Gradient magnetic fields are applied to measure the signal from particular volumes within the subject. Slice images are formed using tomographic image reconstruction. Contrast enhancement may be performed using measurements that weight the signal by the longitudinal and/or transverse relaxation times (T1 and T2). MRI images show tissue properties, but advanced techniques, such as functional MRI (fMRI) and magnetic resonance spectroscopy (MRS), are able to derive functional information, such as regional blood flow.

In ultrasound imaging, the acoustic properties of tissue are probed using high frequency sound waves produced by a transducer coupled to the subject. Ultrasound measures the signal from the reflection and refraction in the tissue and produces an image based on tissue density. Advanced techniques, such as Doppler ultrasound, yield some functional information. Tomographic imaging is also being done using ultrasound.

1.2.3 Computed Tomography

Tomographic imaging is the calculation of the distribution of the signal generating material in a slice of an object from the set of projection data taken at many angles. Tomographic reconstruction techniques have been used in mathematics and physics since the practical implementation of computers. Computed tomography in medical imaging was first practically achieved by Godfrey Hounsfield in 1971 with the introduction of the X-ray CT imager [3]. This was immediately followed with the introduction of the first modern (that is, post CT) PET scanner [4]. The main benefits of tomographic imaging are twofold. First, tomography yields the proper three dimensional (3D) distribution of material in the subject, not a projection of it. This allows for quantification of the properties of the material. The other benefit is that tomography provides better signal contrast for visual interpretation. X-ray CT, for example, images soft tissue organs that would not be visualized in planar images due to the low contrast.

In planar imaging, the signal at each detector element is the line integral projection through the subject at a given angle. The projected data at a radial position, x_r, and azimuthal angle, θ, $p(x_r, \theta)$, are related to the two dimensional distribution in the subject, $f(x,y)$, by the Radon transform:

$$p(x_r, \theta) = \int_{-\infty}^{+\infty} \int_{-\infty}^{+\infty} f(x, y)\delta(x\cos\theta + y\sin\theta - x_r)dxdy \qquad (1.1)$$

The 2D distribution, $f(x,y)$, may be reconstructed from the acquired projection data by inverting the Radon transform. Each 2D distribution is a cross-sectional slice image of the object and the set of slices forms a 3D image volume. In practice, different mathematical techniques are used for tomographic image reconstruction, broadly categorized as analytic and iterative. Analytic reconstruction involves directly inverting the radon transform, and is linear, fast and robust. However, analytic reconstruction alone cannot model the physical and statistical properties of the detection process. Iterative reconstruction makes successive approximations to the image, updating it based on comparisons between the projections of the estimated image and the measured projection data. Some iterative methods model the detection process and may produce images with better noise and accuracy characteristics. However, the use of multiple iterations and added layers of modeling complexities increases the image reconstruction times. As well, these techniques are not linear and may not have good convergence criteria. Tomographic reconstruction in PET is described in more detail in **Section 2.3.4**.

1.3 Nuclear Medicine

1.3.1 Overview

Nuclear medicine uses nuclear tracer techniques to image the functional and biochemical systems of the body. Nuclear medicine includes planar single photon imaging, as well as, tomographic single photon and positron imaging. Routine clinical studies produce qualitative images for visual

interpretation. However, PET is able to quantitatively measure a wide variety of functional and biochemical information in vivo. These include such important parameters as regional blood flow, glucose and oxygen metabolism and receptor binding. Many of these measurements are only possible in human subjects through tracer imaging and only PET has the physical calibrations and corrections necessary for accuracy. Thus, PET has become an important tool for enhancing medicine with the capabilities of quantitative physical science. This is already leading to important advances in both basic medical research, (such as brain activation and neuroreceptor studies or tumour kinetics) and the clinical practice of human medicine (such as the whole body tumour detection or assessment of response to therapy). **Figure 1-2**, below shows a typical set of clinical PET images.

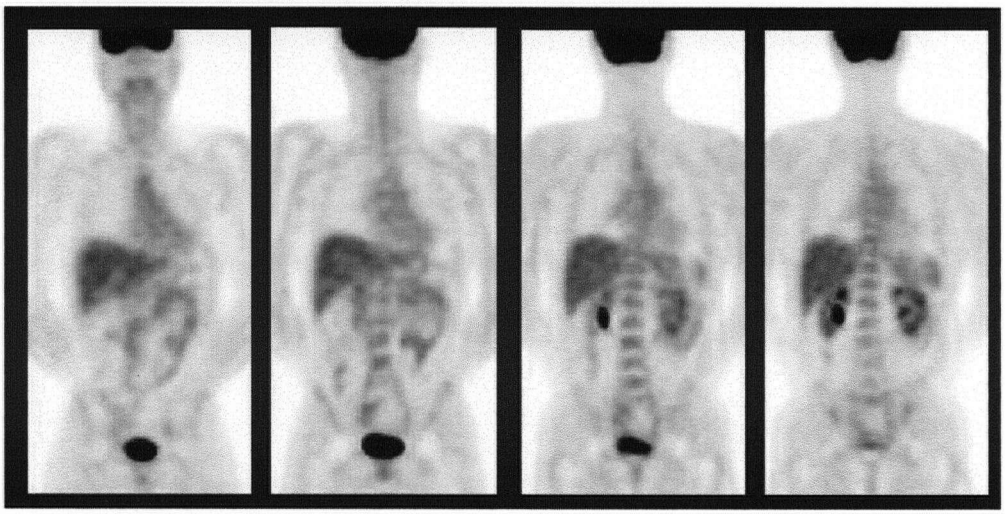

Figure 1-2 Four coronal views from a PET-FDG whole body scan. The tracer is seen to accumulate in a few organs, especially the brain and bladder. FDG also accumulates in tumours presenting in the image as hot spots. This image shows normal physiological response and no evidence of malignant tumours.

1.3.2 Tracer Imaging

Tracer techniques in chemistry, biology and biochemistry begin with the labelling of a compound with a different atom or molecule (called a "tag" or "label") that is not native to the original. Labels

are chosen so that they are detectable externally or following the process under investigation in some by-product. It was recognized in the early days of nuclear physics that radioactive isotopes would provide very suitable labels for the molecule or compounds ("tracers") used to study a specific chemical and biological system. Georg Hevesy first investigated this approach while working with Niels Bohr in Copenhagen in the 1920s and, therefore, Hevesy is considered the "Father" of nuclear medicine while Bohr has been given the title of the "Godfather" [5].

In nuclear medicine, the radiolabelled tracer is introduced into the subject and the physical distribution is measured by an external radiation detector. By measuring the time course of the tracer, temporal information about the tracer distribution may be determined, from which physiological parameters are extracted using various modeling techniques. **Figure 1-3** shows the tracer accumulation and detection process.

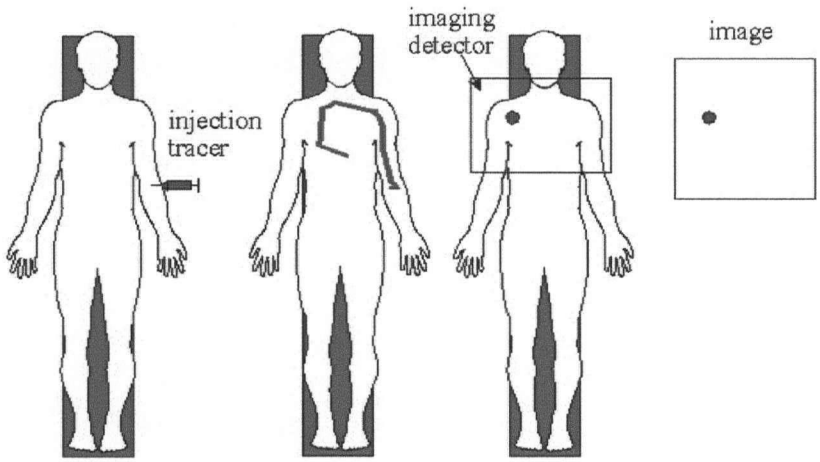

Figure 1-3 The tracer method illustrated. Radioactively labelled tracer is injected into a patient. Over time it accumulates in an organ or lesion where it may be imaged. The dynamic uptake process may also be studied by imaging the tracer distribution as a function of time.

The radionuclides used in nuclear medicine determine the appropriate imaging system. Single photon emitters, usually producing gamma rays from isomeric transitions (e.g. ^{99m}Tc) or following

electron capture decays (e.g. ^{123}I, ^{111}In and ^{67}Ga), are imaged with a large area, position sensitive NaI radiation detector called a "scintillation gamma camera." Images are formed on the detector using a lead parallel-hole collimator that selectively absorbs the gamma rays that are not perpendicular to the detector face. Acquisition times of several minutes are necessary to obtain adequate counts to form an image with a sufficient signal-to-noise ratio. In PET, positron emitting radionuclides are imaged with dedicated tomographs. The imaging principles of PET are described in **Section 1.4**.

Both PET and SPECT use tomographic reconstruction to produce 2D slice images of the spatial distribution of radioactive tracer in the subject. They are "emission tomography" because the radiation used for imaging is emitted from the tracer distribution; in contrast to X-ray CT where the radiation is transmitted through the subject ("transmission tomography"). In SPECT, reconstruction is done using planar image data which are acquired using a rotating gamma camera at a set of angles around a subject [6]. In PET, the projection data is measured from all angles simultaneously.

One of the major benefits of emission tomography is that by determining the spatial distribution of the radioactivity distribution in three dimensions, the resulting images may be quantified if all the appropriate corrections are applied to the acquired data. Thus, the values in each reconstructed voxel may be corrected and calibrated to obtain units of radioactivity concentration (Bq/ml.) More significantly, through the analysis of the spatial distribution or time course of the radioactive tracer, other physiological information, such as blood flow or neuroreceptor binding potential, may be measured. This involves mathematical modeling of the detailed biochemical processes and measuring the time course of a specific appropriate tracer through imaging the relevant biological structures. Measurements of the time dependent activity in the blood plasma or metabolites may also be necessary. To obtain quantitatively accurate values, the instrumentation calibration must be performed accurately and the effects of photon interactions in the subject (absorption and scatter) must be corrected, which requires additional measurements and processing. As well, PET also requires a correction for accidental or "random" coincidences that occur during data acquisition.

In SPECT, corrections for detector blurring are also important. The development and testing of accurate data corrections is the subject of ongoing research in medical physics.

1.4 Positron Emission Tomography

1.4.1 Introduction

The suitability of easily produced positron emitting radionuclides for biological tracer studies was recognized soon after their initial synthesis in the first cyclotrons during the 1930's [7]. The usefulness of the basic quartet of positron emitters, ^{11}C, ^{13}N, ^{15}O and ^{18}F, in biochemistry research was almost immediately recognized. The unique properties of positron annihilation radiation present the possibility of significant technical advantages over single photon imaging with collimated gamma cameras. The collimators on gamma cameras reduce the geometric efficiency to about 0.01%. They are also a significant source of image blurring. PET tomographs, which do not use collimators, have 50 – 100 times the counting efficiency of gamma cameras. As well, PET has superior spatial resolution.

1.4.2 The Physics of Positron Annihilation

Positron decay is a nuclear beta decay mode in which the weak interaction in the nucleus transform a proton into a neutron accompanied by the emission of a positron, β^+, and an electron neutrino, ν. Since positron decay occurs in proton-rich nuclei, positron emitters may be easily produced in cyclotrons using (p,n) or (d,n) reactions. The β^+s are emitted in a continuous spectrum up to a maximum energy, $E_{\beta,max}$. **Figure 1-4** shows the energy spectrum of β^+s from ^{18}F [8].

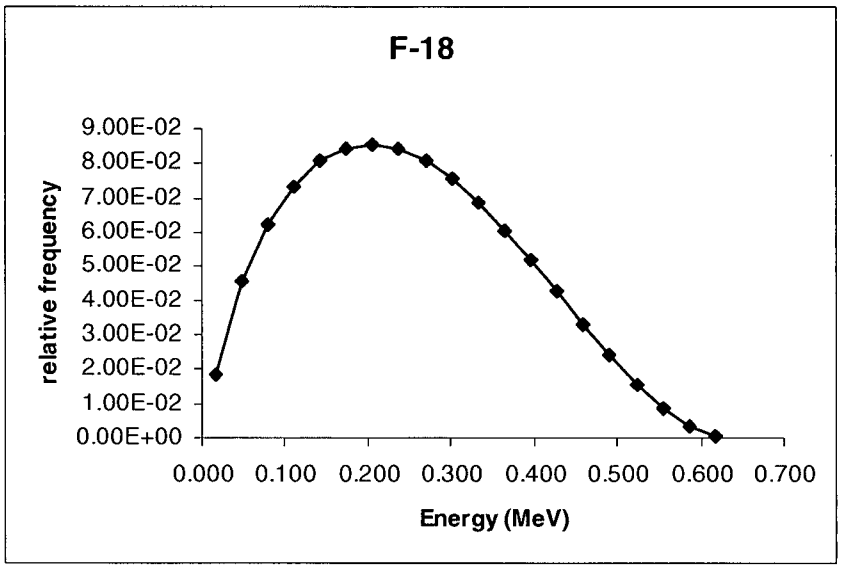

Figure 1-4 The energy spectrum of the positrons from ^{18}F. From ref [8].

The physics of positron annihilation is well known [9][10]. Positrons slow in matter through a series of elastic collisions with atomic electrons. Nearly all annihilations occur only after the positron has thermalized. The annihilation probability depends on the relative spins of the electron and positron upon interaction. If the spins are anti-parallel (singlet state), the probability of annihilation is ~1115 times more likely than for parallel spin (triplet state). Annihilation from the singlet state produces two photons because each photon has an angular momentum of $1\hbar$ and two polarization states. Annihilation from the triplet state produces three photons. Since triplet state collisions occur with three times the frequency of singlet state collisions, the final ratio of two to three photon annihilations is 372. More exotic processes have been discovered that produce more or less photons, but at very low branching ratios.

Alternately, the electron and positron may form a short-lived stable state positronium (Ps) before annihilating. The probability of positronium formation depends on the medium; in water-equivalent matter it occurs in only 36% of decays. Ps exists in either a singlet-state, with spins anti-parallel, $^1S_0$ (para-Ps), or a triplet state, with spins parallel, $^3S_1$ (ortho-Ps). The singlet state is

shorter-lived (mean lifetime =125 ps) than the triplet state (mean lifetime = 140 ns) and again mainly decays by producing a pair of photons.

The two photons emitted from the singlet annihilations with the electron and positron at rest each have an energy equal to the electron rest energy (E_0 = 511 keV) with exactly opposite momenta (nearly collinear in opposite directions) so that the null angular momentum of the singlet state is conserved. In reality, the distribution of positron energies causes small variations in the energies and the angles between the photons (**Section 1.4.5**). The triplet state decays to three photons (total angular momentum = $1\hbar$) and total energy equal to the sum of rest mass of the electron-positron pair (1022 keV). **Figure 1-5** shows a simplified view of the most frequent two-photon positron annihilation process.

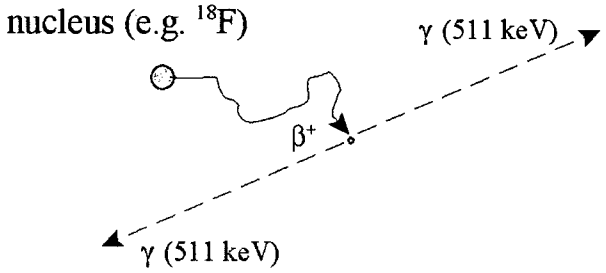

Figure 1-5 The basic process of positron decay and annihilation. A positron is emitted from a nucleus by beta decay. The positron slows by a series of elastic collisions and thermalizes. A collision of the thermal positron with an atomic electron results in annihilation. Alternately, the positron-electron pair may form Ps before annihilation.

1.4.3 Coincidence Detection of Annihilation Radiation

Positron emission tomography uses the coincidence detection of the nearly collinear annihilation photons as projection data from which tomographic images are produced. A PET tomograph is an array of radiation detectors surrounding an imaging volume. Each positron decay within this

volume produces two photons. When one detector is hit by a photon, the other detectors are polled for the detection of a second photon. If a second photon is detected within a coincidence time window (~6-15 ns), one coincidence event is counted. If no second photon is detected, no coincidence event is registered and the event is considered a single photon detection (a "single"). **Figure 1-6** shows a pair of detectors in coincidence.

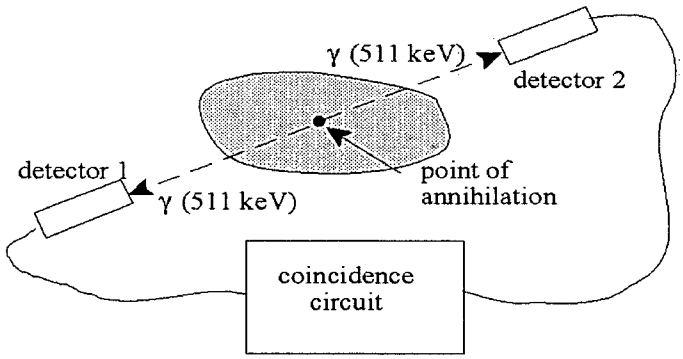

Figure 1-6 A pair of detectors in coincidence is used to detect positron annihilation events. The positron annihilation is assumed to have occurred on the line of response between the two detectors.

When two photons are detected in coincidence, it is assumed that they have both originated from the same annihilation and that the positron decay occurred somewhere along the line between the two hit detectors called the "line of response" (LOR). The LOR does not provide the exact location of the annihilation and decay. Nevertheless, the total number of events per LOR is proportional to the line integral of the radioactivity along the LOR. When multiple detectors are used, the coincidence counts from many lines of response are measured simultaneously to produce a spatial projection profile. A ring of detectors around the radioactivity distribution measures the counts in all the LORs needed to tomographically reconstruct one image slice of the radionuclide distribution. Multiple detector rings are used to measure the counts in the LORs through different slices of the radioactivity distribution. **Chapter 2** describes PET tomographs in detail.

1.4.4 Energy Thresholding

The detected events are not only tested for coincidence, they are also analyzed by an energy window. The detected events with energies below the lower threshold or above the upper threshold are rejected. **Figure 1-7** shows the thresholds in the energy spectrum.

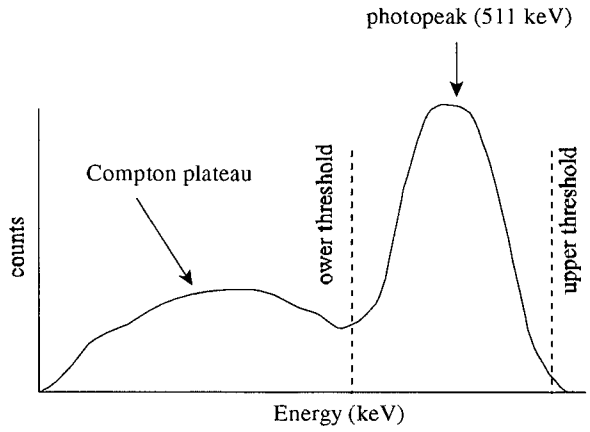

Figure 1-7 The upper and lower energy thresholds and the energy spectrum. The photopeak from the 511 keV photons is shown along with the Compton plateau. The thresholds bracket the photopeak and reject events with energies outside of the defined window.

The energy window is used to reject events due to the photons that have Compton scattered to lower energies in the object. In Compton scatter, photons are elastically scattered from the loosely bound atomic electrons and lose energy. The energy and scattering angle of the scattered photon are related by the Compton equation:

$$E_{sc} = \frac{E}{1+\alpha(1-\cos\theta_{sc})} \qquad (1.2)$$

where E_{sc} = energy of the scattered photon.
E = energy of the unscattered photon.
θ_{sc} = the photon scattering angle.
$\alpha = E/m_e$ = initial photon energy/electron rest mass (511 keV).

The finite energy resolution of the tomograph detectors causes significant overlap between the photopeak and the Compton plateau. Thus, the lower energy threshold may accept and reject both scattered and unscattered events. The choice of threshold value is, therefore, a compromise between counting sensitivity and scatter rejection. Typical values of the lower threshold are 250-350 keV. The optimal threshold depends on the tomograph design and the scanned object.

1.4.5 Positron-range and Photon Non-collinearity

Two details of the positron decay and annihilation process have an impact on the spatial resolution in PET imaging: the positron range and non-collinearity. The emitted positrons travel a short distance (up to a few mm) in the subject before annihilation. This displacement results in the annihilations occurring in a volume larger than the volume of the radionuclide distribution from which they were emitted. The distributions of annihilations from each point of the source overlap, blurring the spatial distribution and reducing the image spatial resolution. The positron range, and therefore the severity of the blurring, depends on the $E_{\beta,max}$ which is radionuclide dependent [11]. The mean positron range in water-equivalent matter for PET radionuclides vary from 0.6 mm for ^{18}F ($E_{\beta,max}$ = 0.630 MeV) to 5.9 mm for ^{82}Rb ($E_{\beta,max}$ = 3.36 MeV). **Figure 1-8** illustrates the effects of positron range.

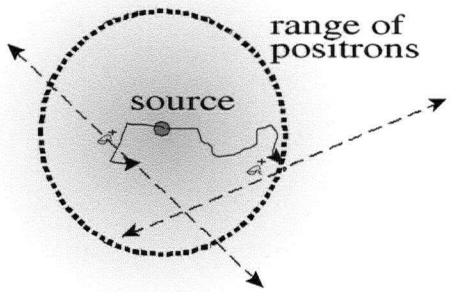

Figure 1-8 The effects of positron range. While the decays occurs within a volume defined by the source, the annihilations occurs within a larger volume defined by the positron range from the source.

The second physical factor that affects spatial resolution in PET imaging is the small non-collinearity of the annihilation radiation. Annihilation photons are perfectly collinear if the total momentum of the electron-positron pair before annihilation = 0. However, annihilation may occur when the positron-electron pair has a small, but finite momentum; thus, for momentum to be conserved, the angle between the annihilation photons is < 180°. The resulting distribution of angles has a FWHM of 0.5°, so that the angle between the photons is 180° ± 0.25°. Non-collinearity results in the errors in the measured LOR and incorrect positioning of the decay, as shown in **Figure 1-9**. The magnitude of the error depends on the design of the tomograph (**Section 2.2.1**).

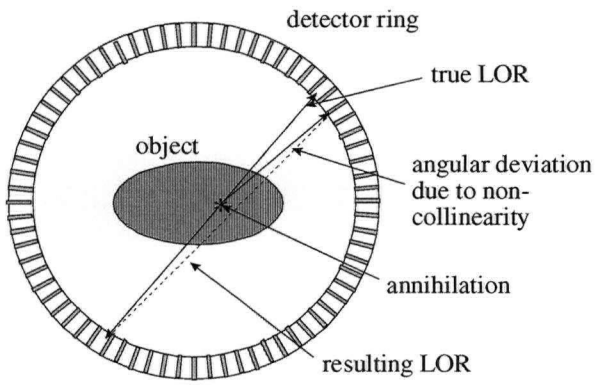

Figure 1-9 The deviation in the measured LOR due to non-collinearity.

1.4.6 Types of Detected Events

As described above, positron annihilation radiation consists of two nearly collinear 511 keV photons. The detection of an individual photon is a single event and the detection of two photons within the coincidence time window is a coincidence event. However, the physical meaning of a coincidence event depends on the histories of two photons involved. If neither photon interacts with the object containing the radioactivity before hitting the detectors the coincidence is a "true coincidence" or "true." Such coincidences measure counts on the true line of response along which the annihilation occurred, as shown in **Figure 1-10.**

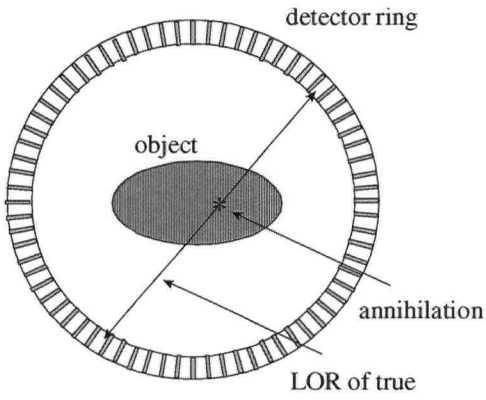

Figure 1-10 A true coincidence in the detector ring of a PET tomograph

However, one (or both) of the annihilation photons may Compton scatter in the object. If both photons are still detected after scattering, they may result in a coincidence event. This accurately reflects the detection of a single annihilation; however, the calculated line of response is incorrect because one (or both) of the photons has been displaced from the original LOR, as shown in **Figure 1-11**. Such events are called "scatter coincidences" or "scatters." Given that they result in an inaccurate LOR, scattered events degrade the image. A fraction of the scatter is eliminated by the energy threshold, but scatter rejection is incomplete.

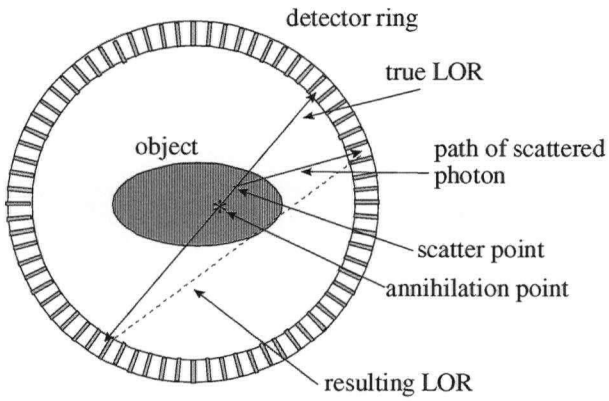

Figure 1-11 A scatter coincidence in the detector ring of a PET tomograph.

A third type of coincidence event occurs when single photons from unrelated annihilations are detected within the coincidence timing window and are counted. This is an "accidental" or "random" coincidence. Randoms incorrectly count the event as originating from a single annihilation and produce an incorrect LOR for the event, as shown in **Figure 1-12**. Randoms degrade image quality and measurement accuracy. The theory of random coincidences and their correction is described in detail in **Chapter 3**.

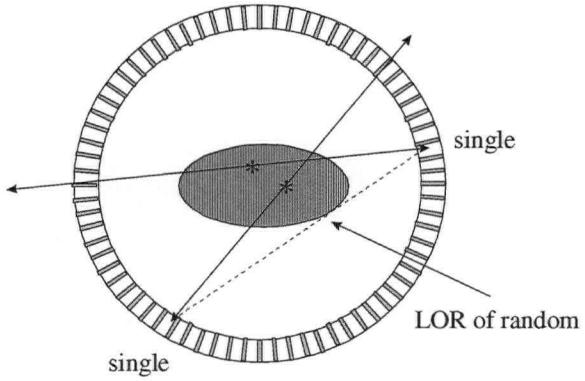

Figure 1-12 A random coincidence in the detector ring of a PET tomograph.

Chapter 2

Tomograph Design and Quantitative Corrections

2.1 PET Tomograph Design

2.1.1 Chapter Overview

This chapter describes the details of the PET detector system that are modeled in the randoms correction calculation. First, the physical design parameters and characteristics of the tomograph and the scintillation detectors are discussed. Then, the various performance characteristics of tomographs are given. Next, the structure of the acquired PET data and the methods of tomographic reconstruction are explained. The chapter ends with a description of the various quantitative corrections that are applied to PET data.

2.1.2 Tomograph Physical Parameters

The detector system used in PET is variously called a "tomograph," "scanner," or "camera." This system is designed to optimally detect the positron annihilation photon pairs emitted from the radioactivity inside a detection volume. Radiation detectors are positioned around this volume and coincidence events in detector pairs are counted. Many designs of positron imaging systems have been explored; including rotating opposing planar detectors[12] and partial rings [13]. Dual-head gamma cameras with upgraded detectors and coincidence acquisition electronics, called "dual head coincidence imaging" (DHCI) systems, have also been developed [14]. None of these designs are presently in common use.

The present standard design of a dedicated tomograph is a set of circular or polygonal rings of scintillation detectors, as shown in **Figure 2-1.** Tomographs vary in the size, type and number of detectors, as well as in the size and number of the detector rings [15][16]. The detector rings enclose the central detection volume, called the "aperture" or "port." This aperture is smaller than the diameter of the detector rings. A bed supports the subject to be imaged and moves them within the port.

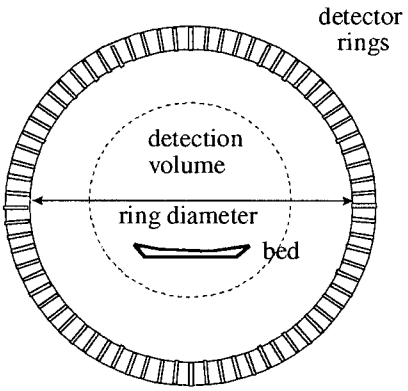

Figure 2-1 The basic layout of the detectors in a PET tomograph. Detector rings of a given diameter surround the detection volume (dashed line). The subject is positioned on a bed in the detection volume.

The size of the aperture determines what may be imaged. "Whole-body" scanners require an aperture large enough to image a human torso (56.2 - 70.0 cm). Head scanners have an aperture only large enough to image a human head; around 35.0 cm (CTI-Siemens HRRT™)[17] . Dedicated animal scanners have smaller apertures, varying from 12.0 cm for dedicated rodent scanners (Siemens MicroPET Focus 120™) to 22.0 cm for small primate scanners (Siemens MicroPET Focus 220™)[18]. The aperture size affects the tomograph performance because the solid angle and blurring effects of non-collinearity depend on the diameter of the detector rings. Larger apertures also increase the cost and complexity of a tomograph because many more detectors are required.

The other major aspect of tomograph geometry is the axial length of the detection volume or the "axial field of view" (AFOV). The size of the AFOV depends on the size of the individual detectors in the axial direction and on the number of detector rings. The AFOV determines the coverage of the subject that may be imaged at one bed position. Large axial extents are imaged by scanning at multiple overlapping bed positions and knitting the images together. Again, the values of the AFOV vary between tomograph types. Both the MicroPET Focus 120 and Focus 220 animal scanners have the AFOV = 7.8 cm. The HRRT dedicated brain scanner has AFOV = 25.2 cm, which is large enough to image the entire brain at one bed position. For whole-body dedicated

PET scanners the AFOV = 15.2 – 25.6 cm. **Figure 2-2** shows the aperture and axial FOV for a typical whole-body PET tomograph.

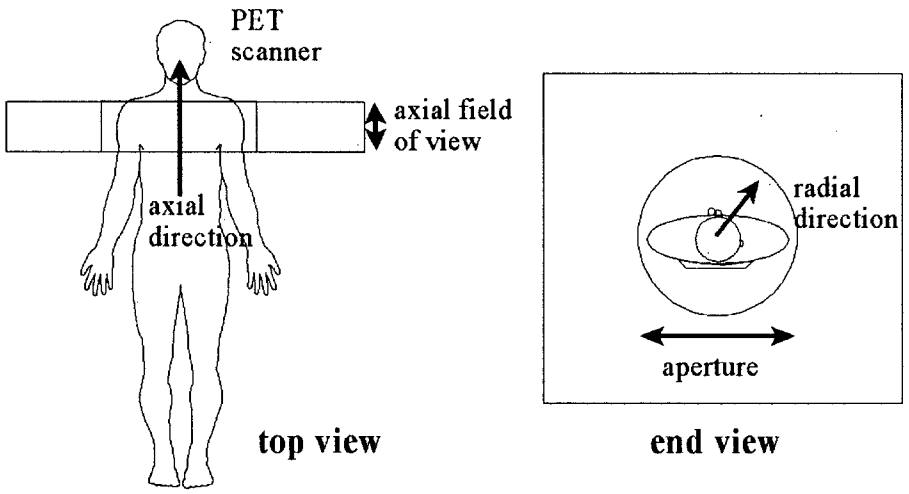

Figure 2-2 The aperture and axial field of view of a dedicated whole body PET scanner.

2.1.3 Detector Materials

The detectors in PET tomographs typically consist of inorganic scintillator crystals coupled to photomultiplier tubes (PMTs) [19]. Scintillators with high density and a high effective atomic number, Z_{eff}, are used because of their high attenuation properties for 511 keV photons. The most commonly used scintillators used in modern PET cameras are Lutetium Oxyorthosilicate (LSO), Gadolinium Oxyorthosilicate (GSO) or Bismuth Germanate (BGO), although Sodium Iodide (NaI), Cesium Fluoride (CsF) and Barium Fluoride (BaF_2) have been used in the past. The properties of PET scintillators are given in **Table 2-1** [20].

Table 2-1 Properties of scintillators used in PET.

Scintillator	Density (g/cm^2)	Z_{eff}	Attenuation Coefficient at 511 keV (cm^{-1})	Decay time (ns)	Light Output (photons/MeV)
BGO	7.1	75	0.95	300	9,000
NaI(Tl)	3.67	51	0.34	230	41,000
GSO(Ce)	6.71	59	0.70	60	8,000
CsF	4.61	52	0.42	2.5	25,000
BaF_2	4.89	54	0.44	0.6/620	1,600/8,200
LSO(Ce)	7.4	66	0.88	40	30,000

LSO, GSO and BGO all have the very good attenuation characteristics for gamma rays. In recent years, LSO has become the scintillator of choice because it also has a high scintillator light output (which influences the energy and spatial resolution) and a fast light output decay time (which influences the high count rate characteristics). The fast decay times also allow for a shorter coincidence timing window, which reduces the rate of random coincidences **(Section 3.2.1)**.

LSO is slightly radioactive due to the naturally occurring isotope ^{176}Lu. This has an abundance of 2.58% and a half-life of 3.8×10^{10} years [21]. ^{176}Lu emits one β^- ($E_{\beta,avg}$ = 420 keV) and three gamma rays with energies and branching fractions of E_γ = 306 keV (94%), 201 keV (78%) and 88 keV (15%) in a single cascade per decay. The total effect of the 306 keV and 201 keV gamma rays is a summed peak at 507 keV with an average yield of 88%. The intrinsic radiation creates a uniform background singles rate in the detector crystals that in turn causes random coincidences. The measured background singles rate in LSO is 240 cps/cc. Simultaneous detection of a beta and gamma from the same decay in different detectors also results in a true coincidence with a spurious LOR. The impact of the ^{176}Lu decays on tomograph count rates depends on the tomograph design and the energy window settings [22][23].

The total efficiency of each detector depends on the intrinsic efficiency, ε_{int}, modified by the effects of the energy window (**Section 1.4.4**). The intrinsic efficiency is given by:

$$\varepsilon_{int} = 1 - e^{-\mu_{det} x_{det}} \qquad (2.1)$$

where μ_{det} = detector scintillator attenuation coefficient.
x_{det} = detector scintillator thickness.

The energy window reduces the number of counted photons by rejecting those with energies outside the window, lowering the total detector efficiency. The effect of the window on efficiency depends on the characteristics of the detector (the energy resolution and photofraction). In an imaging situation, the effects of the window also depend on the photon scatter in the imaged object.

2.1.4 Detector Design

The major determining factor for spatial resolution is the size and spacing of the individual detectors. In early PET detector designs, a single scintillator crystal was coupled to a single PMT so that the minimum size of a detector was limited by the size of the PMT. Cut-block detectors were later developed in which many crystal elements could be read by a few PMTs [24]. In this design, a block of scintillator crystal material is cut into an array of elements. The saw cuts are done at various depths and filled with reflecting material. The cuts are designed to give a unique light pattern to the PMTs for annihilation photons interacting in different crystals, thus allowing the hit crystal to be identified. This increases the effective number of detectors (and reduces the effective detector size) without a corresponding increase in the number of PMTs. For example, the block detector in a typical whole body tomograph (CTI-Siemens ACCEL™) uses an 8 x 8 matrix of 6.45 x 6.45 x 25 mm crystals (64 detector elements total) read out by only four PMTs, as illustrated in **Figure 2-3**.

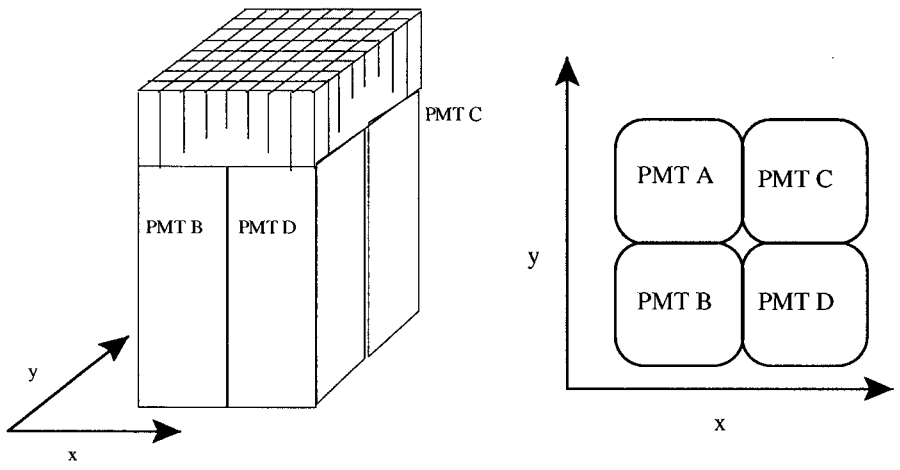

Figure 2-3 A cut-block detector from a PET tomograph. The scintillator is cut into channels which guide the light to the PMTs. The light from the photon interactions in each crystal produces a unique pattern in the PMTs. From this pattern, the hit detector element is identified.

The block addressing electronics calculates the interaction point of the detected photon by a simple analog ratio, similar to Anger logic used in scintillation gamma cameras. For four PMTs (A, B, C, and D), the event position within the block (x,y) is found from the ratios of the output signals:

$$x = \frac{i_A + i_B - (i_C + i_D)}{i_A + i_B + i_C + i_D}, \quad y = \frac{i_A + i_C - (i_B + i_D)}{i_A + i_B + i_C + i_D} \tag{2.2}$$

where i_A etc = signal from PMT A, etc

These position signals are then used to identify the hit detector element from preset crystal identification map. The summed signal, $i_Z = i_A + i_B + i_C + i_D$ is proportional to the total energy deposited in the detector block. In other designs, the cut-block crystal is optically coupled to a large position sensitive PMT that determines the hit detector element.

Decreasing the crystal sizes (by making more cuts) improves the spatial resolution. However, more cuts also results in less scintillator material being present in the block. This decreases the "packing fraction" of the detector and reduces the total counting efficiency of the tomograph.

2.1.5 Tomograph Structure and Electronics

The tomograph detector structure is built up from the basic unit of the detector block. In most designs, several blocks are combined into a "module" or "bucket" in which the detectors share a common enclosure and/or common electronics. The modules are arranged around the central aperture to form rings, and multiple rings of detector blocks are typically used. **Figure 2-4** shows a ring arrangement of detector blocks around a central aperture.

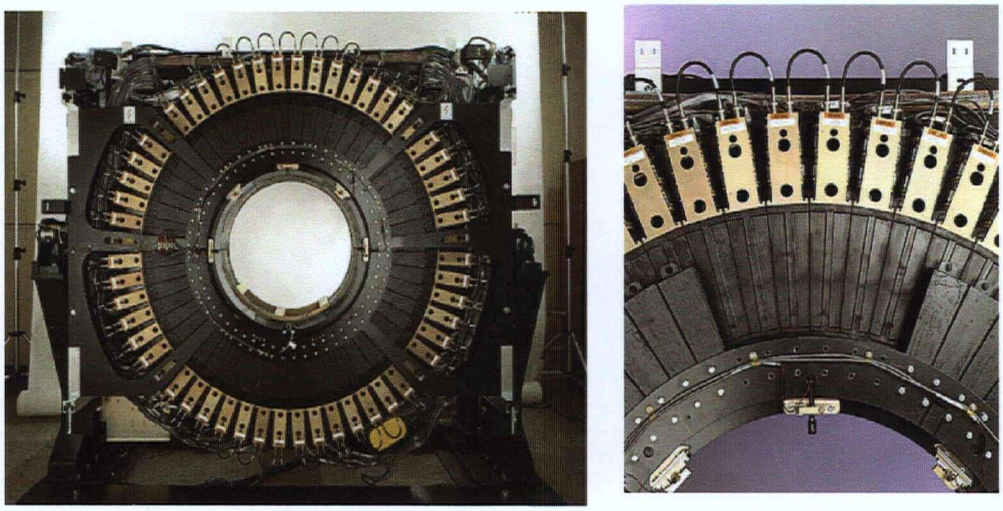

Figure 2-4 The detector ring of a whole body dedicated PET tomograph. Detector blocks form a ring around a central aperture and multiple rings increase the axial extent. (Courtesy G.E. Medical Systems)

Many layers of electronics are required to process events. The front-end electronics are responsible for anode signal integration and digitization. The PMT signals within a block detector are used to identify the hit crystal and are summed to yield an energy signal which is tested by an energy threshold. In older systems, each detector signal was tested for coincidence by dedicated

coincidence electronics. In modern tomographs, with a large number of detectors, testing each signal for coincidence with all other detectors is impractical. Instead, each detected event is given a time-stamp and sent to the digital coincidence processor. After a fixed time, each event in the buffer is tested for coincidence with every other event by comparing the differences in detection time to a predetermined coincidence timing window (CTW). The coordinates of the line of response (LOR) are calculated for each identified coincidence event from the positions of the detectors involved. The event may be counted by incrementing the value in a memory location that corresponds to its LOR. Alternately, the event information, including the detection time, may be stored in a list of the event-words ("list-mode").

Many aspects of the electronics are user controllable or have parameters in updatable look-up tables. For example, PMT voltages and pre-amplifier gains are usually adjustable through software for tuning. As well, crystal identification map parameters may be adjustable. The final energy window and coincidence timing windows are set as part of the acquisition parameters.

2.1.6 2D and 3D Acquisition modes

Potential coincidences between detectors in different rings may be processed in different ways. In "2D mode" acquisition, used in some clinical imaging protocols and older tomographs, thin annular lead shielding called "septa" are positioned axially between the rings of crystals. The septa absorb photons at large oblique angles, physically preventing true coincidences between all but the neighbouring rings. In addition, coincidences are electronically limited to detectors within the same ring or between neighbouring rings. 2D mode has the benefit of reducing the contribution from the scattered photons and photons from radioactivity outside the axial field of view of the tomograph, which contaminate the image data. As well, data acquired in 2D mode require simpler reconstruction methods.

Virtually all modern tomographs acquire data in "3D mode," in which no inter-slice septa are used and coincidences may be acquired between detectors in any rings. The 3D acquisition mode increases the sensitivity of the tomograph (6-7 times) by allowing events along the oblique LORs

to be counted; thus, increasing the total number of LORs sampled. This increases the total number of counts collected, improving the statistical quality of the acquired data. However, the increase in sensitivity is at the expense of increasing the contribution of scatter and random coincidences. The reconstruction of 3D data is also more complex because of the increased number of LORs and the difficulties caused by the oblique LORs intersecting multiple transverse slice planes. **Figure 2-5** compares 2D and 3D mode acquisition.

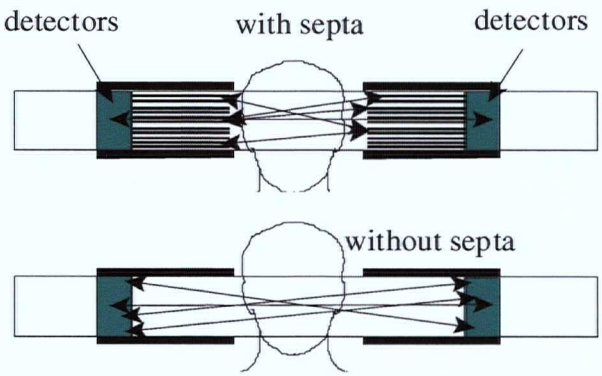

Figure 2-5 2D and 3D acquisition for a PET head tomograph. In 2D mode (top) the septa absorb the axially oblique photons. In 3D mode (bottom) oblique LORs are accepted, significantly increasing the number of LORs sampled and, therefore, the sensitivity.

2.2 Tomograph Performance Characteristics

The performance characteristics of a PET tomograph are determined by its design and by the acquisition parameters. The performance ultimately affects the qualitative and quantitative value of the data. The most important performance characteristics are:

- spatial resolution,
- sensitivity, and
- count rate performance.

Other important characteristics include energy resolution and scatter fraction. Standard performance measurements have been published in "NEMA NU-2 2001. Performance Measures of Positron Emission Tomographs." [25][26].

2.2.1 Spatial Resolution

The tomograph spatial resolution is defined as the amount of blurring in reconstructed image as characterized by the full width at half maximum (*FWHM*) of the point spread function (PSF). The most significant factors in the spatial resolution are the detector size and separation, but parallax, the block addressing accuracy, non-collinearity and positron range are also important. The reconstruction method and parameters also influence the resolution of the final reconstructed images.

The contribution of the detector crystal size, d, to the resolution, $FWHM_{crystal}$ varies with the radial position of the source. At the radial centre $FWHM_{crystal} = d/2$, but worsens as the source position moves off-axis due to parallax errors and other geometric effects. In cut-block detectors, addressing errors within the block, $FWHM_{block}$, further degrades the resolution. Photon non-collinearity (**Section 1.4.2**) causes additional blurring that depends on detector separation:

$$FWHM_{non-coll} = 0.0022 D_{ring} \qquad (2.3)$$

where D_{ring} = ring diameter.

The effect of non-collinearity on spatial resolution is on the order of 1.4-1.5 mm for a 50 cm detector ring and 2.0-3.0 mm for a 100 cm ring. The blurring also increases with positron range, which is radionuclide dependent (**Section 1.4.2**). The contribution to the *FWHM* varies from 0.2 mm, when imaging with ^{18}F, and increases to 2.6 mm for ^{82}Rb. Finally, the total *FWHM* of the PSF of the reconstructed image depends on the reconstruction method. The total system spatial resolution due to all of these effects is given by [27]:

$$FWHM_{sys} = k_{recon}\sqrt{FWHM^2_{crystal} + FWHM^2_{non-coll} + FWHM^2_{range} + FWHM^2_{block}} \quad (2.4)$$

where k_{recon} =a constant that depends on reconstruction method and parameters

In animal tomographs, spatial resolutions of ~1 mm have been achieved (MicroPET Focus™), but, for commercial whole body scanners, the transverse spatial resolution at 1.0 cm off-axis is 4.5 – 6.3 mm, depending on the tomograph and acquisition mode.

2.2.2 Sensitivity

The sensitivity of a tomograph is the ratio of the measured true coincidence count rate to the activity of the source within the sensitive volume. The sensitivity depends on the tomograph geometry (solid angle) and the detector efficiencies (2.1). The geometric efficiency of a tomograph in 3D mode for a point source at the axial centre is given by:

$$\varepsilon_{geo,point} = \sin(\tan^{-1}(D_{axial} / D_{ring})) \quad (2.5)$$

where D_{axial} = axial extent.
D_{ring} = ring diameter.

In 3D mode, the geometric efficiency varies axially with a triangular profile, with the maximum at the axial centre. Therefore, the average geometric efficiency for an extended radioactive source within the tomograph volume is $\overline{\varepsilon_{geo}} \approx \varepsilon_{geo,point}/2$.

The total tomograph sensitivity also depends on the square of the detector efficiency, because two detectors are required for a coincidence event. The packing fraction of the detectors also affects the sensitivity. Overall, the sensitivity for a point source at the centre of the FOV varies from 0.2 – 0.5% for tomographs operating in 2D mode up to 2 - 10% for those in 3D mode [28].

2.2.3 Count Rate Performance and Noise Equivalent Count Rate

Detector and electronics dead-times in the tomograph limit the performance, causing count rate dependent dead-time losses and a maximum achievable count rate. These affect the accuracy of the measured count rates, the total counts obtained for a given acquisition time and, therefore, the signal-to-noise ratio of the data. The main factor in the count rate performance is the scintillator decay time, but the processing times at other stages of the electronics also contribute. The decay times range from 40 ns for LSO to 300 ns for BGO, but longer integration times are used to maximize the signals and improve the energy resolution. The finite event processing time also results in pulse pile-up in the detector blocks which may affect block addressing and energy discrimination accuracy. The metrics used for these performance issues are the maximum trues or trues+scatter count rate or the count rate associated to 50% dead-time.

Another count rate dependent issue is random coincidences. As the singles count rates increase, so does the rate of true and random coincidences. However, the randoms increase as the square of the singles, while the trues increase proportional to the singles (**Section 3.2.1**). Since randoms degrade the image data, the overall quality of the data depends on count rates. A useful metric for determining the effect of count rate (and thus randoms rate) on overall data quality for a tomograph is the noise equivalent count rate (NECR) [29]:

$$R_{NEC} = \frac{R_t^2}{R_t + R_{sc} + k_{rand} R_r} \qquad (2.6)$$

where R_t = trues count rate.
R_{sc} = scatters count rate.
R_r= randoms count rate.
k_{rand} = a constant 1 or 2 depending on randoms correction method.

The dependence of NECR on the count rate (and source activity) allows the effects of the various contributions to the total coincidence rates to be assessed. The NECR has been likened to the square of the signal-to-noise ratio, $(S/N)^2$, because it is a comparison of the true signal strength over the background and noise. Since scatters and randoms given inaccurate positional and activity

information (**Section 1.4.6**), they penalize the function. Note that the randoms term contains a factor, k_{rand}, which depends on the method of randoms correction. Using measured delays increases the contribution from the noise due to the randoms, $k_{rand}=2$. Using randoms corrections with reduced variance decreases the contribution from the randoms $k_{rand}=1$ and increases the NECR, as discussed in **Chapter 3**.

The NECR curve is used to compare the effects of different acquisition, processing and correction parameters on the data count rate, as well as the general characteristics between different scanners. In 3D PET, the NECR curve has a peak value which is a useful figure of merit. The activity concentration that produces the maximum NECR may be used to determine the optimal injected dose to be used in a given type of study. **Figure 2-6** illustrates the relationship between various coincidence count rate contributions to the *NECR* for a typical scanner in 3D mode.

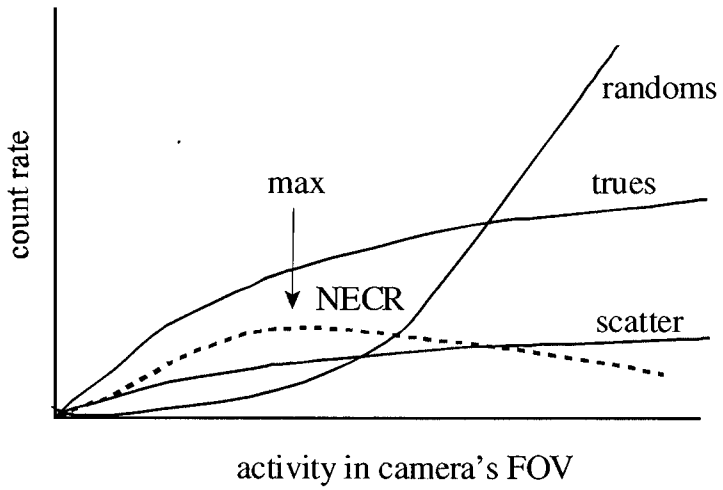

Figure 2-6 The relative coincidence count rates from trues, randoms, scatters and the resulting NECR are shown for different activities. This is for a typical scanner operating in 3D mode.

2.2.4 Other Performance Characteristics

The energy resolution of a PET scanner is determined mainly by the scintillator conversion efficiency and the light collection characteristics of the detector design. For 511 keV photons, the *% FWHM* values for simple (non-block) detectors are 18%, 7%, 9% and 11% for BGO, NaI,

GSO and LSO, respectively [16]. These values, however, are higher in block detectors and vary between individual crystals within a block. The energy resolution determines the optimal energy window settings during data acquisition and the resulting sensitivity and scatter fraction.

The scatter fraction, SF, is defined as the fraction of the non-random coincidences in which one photon underwent Compton scatter coincidences.

$$SF = \frac{R_{sc}}{R_{sc} + R_t} \tag{2.7}$$

where R_t = trues count rate.
R_{sc} = scatters count rate.

Although the scatter fraction depends mainly on the size and density of the object, the SF also varies with tomograph size, detector characteristics and acquisition mode and parameters. When measured using a standard phantom, SF becomes a performance measure by which the effects of tomograph design and/or acquisition parameters are compared. For the majority of scanners, the measured SF ranges from 15%-20% in 2D mode and 30-40% in 3D mode. However, when performing whole body human scans, the scatter fractions for 3D mode may be significantly higher (50-80%).

2.3 PET Data Acquisition and Reconstruction

2.3.1 PET Data Acquisition

A PET study consists of acquiring the data necessary to reconstruct the radioactivity distribution in the subject. This is primarily an emission scan, which counts the detected coincidences from the annihilation photons originating in the radioactivity within the subject. A single "static" frame is acquired to image a region of the subject when the radionuclide distribution does not change over the duration of the scan. "Whole body" static images scans are formed by acquiring static frames

at multiple bed positions. If the time course of the tracer distribution is to be measured, the data may be acquired at a predetermined number of contiguous time intervals (time frames) forming a "dynamic scan."

Two other scans are also performed: the blank and transmission scans. These are necessary for attenuation correction, as described in **Section 2.4.3**. A single blank scan is generally performed on a daily basis, and is also used for quality control. If detectors are poorly tuned or failing, they cause visually detectable artifacts in the blank scan. A transmission scan is required for each subject at each bed position. This may be done before or after the administration of the radioactive tracer. During the transmission scan, the subject must be maintained at the exact same position as they were in the emission scan; otherwise the attenuation correction would be inaccurate.

2.3.2 PET Data Structure

Since a valid event in PET involves the coincidence detection of two photons by a pair of detectors, events might be labelled simply by the identification of the two detectors involved. A more physical event address is provided by calculating the parameters of the line of response (LOR) between the centres of the two detectors. Therefore, within a slice plane, only two parameters are required: x_r, (radial displacement) which is the perpendicular distance from the LOR to a parallel chord through the radial centre of the aperture and θ, the azimuthal angle of the LOR with respect to an arbitrary 0° angle. The LOR parameters are illustrated in **Figure 2-7**.

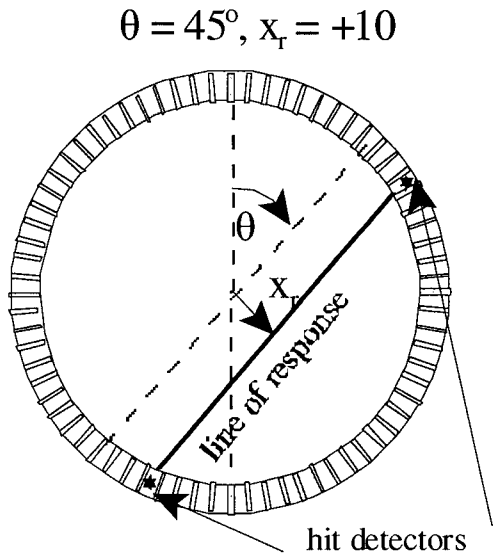

Figure 2-7 The geometric parameters describing a LOR within one slice plane. x_r is the radial displacement of the LOR from a parallel chord through the centre and θ is the azimuthal angle.

In 2D PET, only LORs from within transverse slice planes are acquired and these planes are identified by a third parameter: the slice number, or axial position of the slice, "z." In 3D PET, the events from oblique lines of response are also measured. Two parameters are required to label the oblique slice planes: the identities of the two detector rings involved, ("$z1$" and "$z2$"), the position of one ring and the ring difference to the second ring, ("$z1$" and "δ") or the position of one ring and the oblique angle of the slice plane ("$z1$" and "φ"). Thus, four parameters are required to define each 3D LOR uniquely. The total number of possible LORs increases significantly compared with 3D acquisition.

PET data have traditionally been stored in two dimensional histograms of counts per LOR (parameterized by x_r and θ) for each slice plane. Such histograms are called "sinograms," so named because each point of radioactivity in an object traces out a sinusoidal wave with changing angle in the sinogram. Each row of a sinogram contains the data from the parallel LORs at one azimuthal

angle from one slice plane. Thus, each row of the sinogram is a different projection. Each sinogram is indexed by the parameters that identify the slice plane. **Figure 2-8** shows the LORs involved in coincidence detections from a point source and their corresponding addresses in a sinogram.

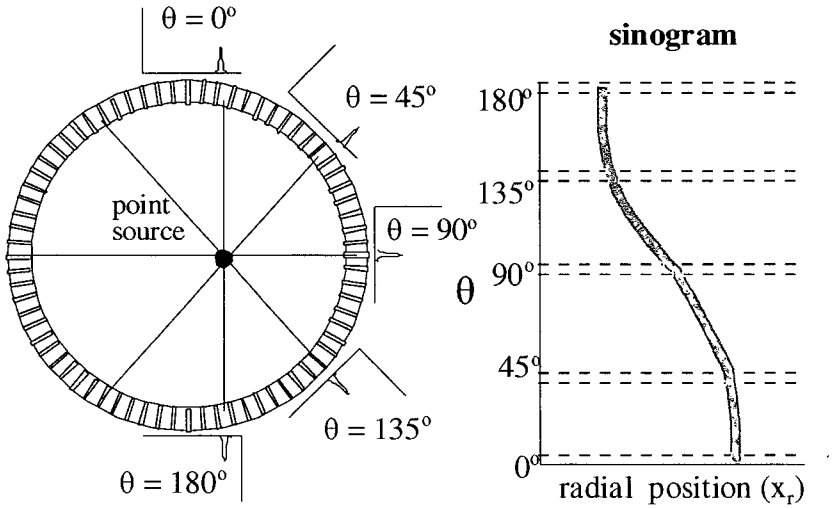

Figure 2-8 An example of a sinogram. PET acquisition is performed on an off-axis point source. All the LORs of valid coincidences form a sine wave in the histogram of counts vs. radial positions and azimuthal angle. The various parallel projections at different angles are shown outside the tomograph ring.

In 2D acquisition, each sinogram contains the data from one detector ring or pair of neighbouring rings that is used to reconstruct one transverse slice; thus, there is one sinogram per image plane. 3D mode data sets also include many oblique sinograms. Each oblique sinogram contributes to multiple transverse image planes during the reconstruction. The inclusion of the oblique sinograms greatly increases the total sinograms per study. For example, a 2D study the number of acquired sinograms is $2N_{rings}-1$, where N_{rings} is the number of detector rings. In 3D acquisition, the maximum number of sinograms is N_{rings}^2. Therefore, a tomograph with 32 detector rings yields 63 sinograms in 2D mode but up to 1024 sinograms in 3D mode. In practice, data reduction schemes are often used in 3D mode to reduce the number of acquired sinograms.

Data may also be stored in list mode, as described above. In list mode the data file size grows with the amount of acquired data since each event is stored separately and not immediately histogrammed. List mode is the most flexible way of storing the data since it may be later histogrammed into static or dynamic frames or may be reconstructed directly from list mode [30].

2.3.3 Data Reduction Schemes

To reduce the size of the data set, a number of data binning schemes have been introduced [31] [32]. These reduce the size of each sinogram and/or the number of sinograms. The technique of "angular mashing" sums together the counts in the LORs at adjacent angular bins (rows in the sinogram), thus reducing the size of the sinogram and increasing the counts per LOR. For example, if a mashing factor of 2 is used, every pair of rows (angular bins) in the sinogram is summed reducing the number of rows (and the size of the sinogram) by half. This reduces the angular resolution of the data by a factor of two. Often limited angular mashing may be performed without affecting the overall spatial resolution because most scanners tend to oversample in the angular dimension.

Oblique sinograms in 3D acquisition may also be summed to reduce the number of sinograms. The number of oblique angles summed is determined by a parameter called the "span." The span determines the averaging of the alternating oblique slices. A span of 1 means no averaging is done. If span = 3, the alternate slices are averaged by factors of 1 and 2 respectively (1+2 = 3). Increasing the span of a data set reduces its size, but also causes a reduction in the spatial resolution most prominent in the axially centred and radially off-centre regions of the FOV. Another data reduction scheme is to reduce the number of oblique bins used by limiting the maximum "ring difference" of the LORs being sampled. Larger ring differences sample larger oblique angles. In these schemes, 2D acquisition with direct and cross slice could be considered span = 3, max ring difference = 1. If 3D acquisition is performed on a tomograph with 32 physical detectors rings using span = 3 and maximum ring difference = 31, a total of 703 sinograms are acquired: 63 direct slice planes and 640 oblique planes.

2.3.4 PET Image Reconstruction

PET images are reconstructed from 2D or 3D data sets using a number of different methods [32][33][34]. These are broadly classed as analytic or iterative. The most commonly used analytic reconstruction method is 2D filtered backprojection (2D-FBP). FBP is an exact, analytic solution to the inverse radon transform. As its name suggests, FBP requires two steps: filtering and backprojection. First, the projection data are filtered with a ramp filter in the spatial frequency domain. This an integral part of the reconstruction because the ramp filter is actually the Jacobian of the transformation of rectangular to polar coordinates. This is required because the projections are acquired at varying azimuthal angles, but are used to reconstruct an image in a Cartesian coordinate system. Next, the counts from the filtered projections are backprojected onto an image space matrix and appropriately summed in image elements (voxels).

The projections are the line integrals through the object slice at a given azimuthal angle:

$$p(x_r,\theta) = \iint f(x,y)\delta(x\sin\theta - y\cos\theta - x_r)dxdy \qquad (2.8)$$

where $f(x,y)$ = 2D slice of the radioactivity distribution.
$p(x_r,\theta)$ = projection (radon transform)of 2D slice.

In PET, they are the set of parallel LORs at a given angle, or the rows of the sinogram.

The filtering of the projections is performed in spatial frequency domain. Thus, the projections are first fourier transformed.

$$P(\omega,\theta) = \int p(x_r,\theta)e^{-i\omega x_r}dx_r \qquad (2.9)$$

where $P(\omega,\theta)$ = fourier transform of the projection.

The transformed projections are then multiplied by the ramp filter, inverse transformed and backprojected to recover the 2D slice of the radionuclide distribution:

$$f(x,y) = \frac{1}{4\pi}\iint P(\omega,\theta)|\omega| e^{+i\omega(x\sin\theta - y\cos\theta)} d\omega d\theta$$
$$= \frac{1}{4\pi}\int p_{filt}(x_r,\theta) d\theta \qquad (2.10)$$

where $|\omega|$ is the ramp filter.

FBP is linear, very fast and robust. However, it assumes that the data consist of perfect projections, free of statistical noise or biases due to attenuation, scatter or randoms. As a result, FBP images are generally noisy and may contain quantitative inaccuracies and/or artifacts from the physical biasing factors. However, if sinograms are corrected for attenuation, randoms and scatter before or during reconstruction the biases are significantly reduced. The image noise may be reduced by applying a smooth, low-pass filter in the same step as the ramp to control the high frequency image components. However, this filtering may itself cause artifacts and negative counts, especially at large discontinuities in the image. While this may cause visible distortions in the image, the linearity of FBP preserves the quantitative accuracy.

Iterative reconstruction works by attempting to produce successively better estimates of the image using the measured projection data. This is achieved by maximizing or minimizing a cost function which describes the goodness of fit between the estimated image and the measured projections. Reconstruction begins with an initial simplistic estimate of the image. This is then forward projected and the resulting projections are compared with the measured projections to produce update factors. These factors are then backprojected and used to update the estimated image. The process of forward projection-comparison-backprojection is done once per iteration. The iterations end when a convergence condition, based on the value of the target function, has been met (if it exists).

The forward/backprojection process in iterative reconstruction has the potential benefit that the physics of the acquisition process may be incorporated into the mathematics of the projector/backprojector calculations. Thus, the effects of counting statistics, attenuation, scatter, and random events may also be included in the reconstruction process.

Statistical iterative methods include the modeling of the Poisson counting statistics. The first significant method of this class was maximum-likelihood expectation maximization (MLEM) [35]. MLEM uses a cost function, modeled on the Poisson distribution of measured values, as a measure of fitness. The projection-comparison-backprojection steps are given by a calculation of the form [36].

$$f_j^{k+1} = \frac{f_j^k}{\sum_{i=1}^{n} a_{ij}} \sum_{i=1}^{n} \frac{a_{ij} p_i}{\sum_{j'=1}^{m} a_{ij'} f_{j'}^k} \tag{2.11}$$

where f_j^k = voxel values estimates in the image at iteration k.
p_i = pixel values of projection sinogram corrected for randoms and scatter (i.e. $p_i - r_i - s_i$) where r_i and s_i are the contributions due to randoms and scatter, respectively.
a_{ij} = system matrix elements describing relationship between image voxels and projection pixels.
n = number of LORs.
m = number of image voxels.

While MLEM reduces statistical noise in the image and is shown to converge, it has a number of drawbacks. First, it requires a large number of iterations to converge (50-200) and is, therefore, very slow. As well, in practice it must be stopped before convergence because, after a number of iterations, it begins to reproduce the noise in the projections by introducing noise in the image.

A faster implementation of MLEM, ordered-subset expectation maximization (OSEM), was developed to speed up the iterative reconstruction process [37]. OSEM groups the projections into subsets which span the angular range of the projections. Each subset is reconstructed with the MLEM algorithm sequentially so that the image is updated once per subset until all the subsets have been used, ending a single iteration. Since the image is updated more frequently than MLEM, OSEM reconstruction is generally much faster.

While MLEM and OSEM require the projection values to be fully corrected for scatter and randoms before reconstruction, an MLEM variant, ordinary Poisson-expectation maximization (OP-EM) [33] [38] includes these in the image estimate:

$$f_j^{k+1} = \frac{f_j^k}{\sum_{i=1}^{n} a_{ij}} \sum_{i=1}^{n} \frac{a_{ij} p_i}{\sum_{j'=1}^{m} a_{ij'} f_{j'}^k + r_i + s_i} \qquad (2.12)$$

where p_i = pixel values of projection sinogram *not* corrected for randoms and scatter.
r_i = randoms events per pixel i
s_i = scatter events per pixel i.

This method has been shown to produce quantitatively more accurate images than MLEM and is considered the method of choice in high resolution PET imaging [39]. There is also an ordered-subset version of this method, OP-OSEM.

Another variation of the MLEM, Maximum a Posteriori (MAP), imposes conditions based on prior knowledge of the image (such as non-negativity and smoothness) in a manner similar to Bayesian logic [40]. MAP is flexible and gives good visual results in reducing noise and improving spatial resolution; however, it is quantitatively less accurate than OP-OSEM.

3D PET data may also be reconstructed by analytic or iterative methods carried over from the 2D versions. The 3D re-projection (3DRP) method [41] is the 3D equivalent of FBP and inherits the same problems as 2D-FBP. 3D versions of the statistical iterative techniques are also available. One option for a 3D data set is to rebin it into a set of 2D sinograms and then reconstruct them using a faster 2D algorithm. The most common rebinning method is fourier rebinning (FORE) [42]. FORE uses the distance-frequency principle to rebin the fourier transforms of the projection data and therefore may only be performed post-acquisition. However, FORE is accurate for off-axis activity and has become the standard method of 3D rebinning. An additional rebinning method is single slice rebinning (SSRB) [43] which simply assigns the LORs in an oblique plane to the direct slice plane equidistant between the involved two detector rings. This distorts the

accuracy of off-axis components of reconstructed radioactivity distributions, making SSRB only useful for compact radioactivity distributions near the tomograph axis. However, SSRB may be applied during acquisition.

2.4 Quantitative Corrections

2.4.1 Introduction

PET uses a number of quantitative corrections to remove spurious events from the measured data, and to correct for physical and detector limitations of the acquisition process. These corrections and calibrations are done for:

- random coincidences,
- photon attenuation,
- detector normalization,
- detector dead-time,
- photon scatter , and
- sensitivity calibration.

2.4.2 Randoms Correction

Randoms correction is the subtraction of random coincidences from the total measured coincidences in the sinograms. The subtracted randoms may be directly measured or calculated from other measured parameters. **Chapter 3** describes the details of randoms correction and the remainder of this thesis presents a new method of randoms correction.

2.4.3 Attenuation Correction

Photons emitted from within an object are subject to interactions along the path from the emission point to the detector. For 511 keV photons in human tissue, these interactions are predominantly Compton scatter. In PET, if either annihilation photon interacts such that it is not detected, coincidence detection cannot occur and the positron decay is not detected. The resulting reduction in the counts along an LOR is described as "attenuation." Attenuation not only leads to significant count losses, but the effects of attenuation vary with the location of the decay and the specific distribution of attenuating material. Thus, attenuation must be corrected before, or during, reconstruction, or it will lead to considerable biases in the reconstructed radioactivity distribution. However, if the scattered photons are detected elsewhere in the tomograph, an erroneous LOR results in a "scatter" event (**Section 1.4.6**). Scatter events must be removed from the data set before reconstruction (**Section 2.4.5**). Thus, Compton scatter results in both attenuation and scatter events.

The fraction of primary photons transmitted through an attenuating medium without interaction is given by the line integral:

$$f_{atten,1} = e^{-\int_{x_o}^{x_1} \mu(x)dx} \qquad (2.13)$$

where $\mu(x)$ = position dependent attenuation coefficient.
x_o = emission point.
x_1 = edge of attenuating medium.
dx = path along the LOR through the attenuating medium.

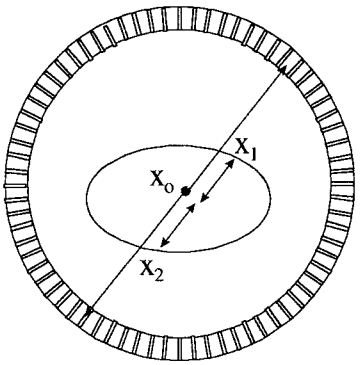

Figure 2-9 Attenuation in PET scanning. The intensity of annihilation photons is reduced in the object along the LOR from the emission point to the edge of the attenuating medium.

Likewise, the fraction of annihilation partner photons transmitted is given by:

$$f_{atten,2} = e^{-\int_{x_o}^{x_2} \mu(x)dx} \tag{2.14}$$

where x_2 = opposite edge of attenuating medium.

The probability of both photons being transmitted, P_{coinc}, is also the same as the probability of a coincidence (neglecting detecting efficiencies):

$$P_{coinc} = f_{atten,1} f_{atten,2} = e^{-\int_{x_o}^{x1} \mu(x)dx} e^{-\int_{x_2}^{x_o} \mu(x)dx} = e^{-\int_{x_2}^{x1} \mu(x)dx} \tag{2.15}$$

Thus, the probability of a coincidence only depends on the total attenuation along the length of the LOR and is independent of the point of emission along the LOR.

A number of methods have been used to correct for attenuation in PET [44], most of which involve a direct measurement of the attenuation using a transmission scan. In this scan, one or more moving radiation sources are positioned in the tomograph aperture outside the object. During the transmission scan, these sources move and the count rates are measured at all the lines of response. **Figure 2-10** shows the arrangement for transmission scanning.

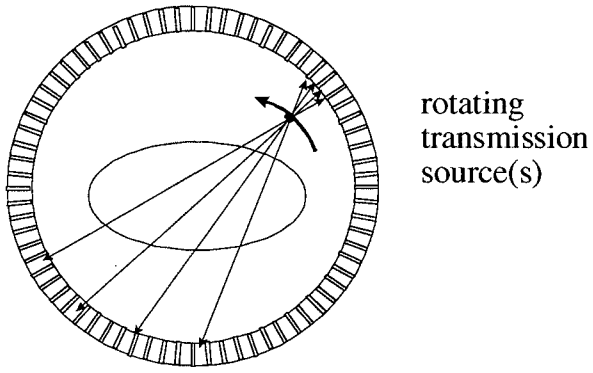

Figure 2-10 The arrangement for a transmission scanning system. The external sources are used to sample the counts rates for LORs through the object.

The counts for the transmission lines of response are measured and stored in transmission sinograms, $N_{trans}(x_r,\theta)$. The blank scan is also done using the transmission sources, but with the aperture empty yielding a set of blank sinograms, $N_{blank}(x_r,\theta)$. Sinograms of the attenuation correction factors (ACFs) are then calculated as.

$$ACF(x_r,\theta) = \frac{N_{blank}(x_r,\theta)}{N_{trans}(x_r,\theta)} \qquad (2.16)$$

where $N_{blank}(x_r,\theta)$ = measured counts in blank scan at a given sinogram element.
$N_{trans}(x_r,\theta)$ = measured counts in transmission scan at a given sinogram element.

The value of the ACF for each sinogram element is then the inverse of P_{coinc} (2.15) for the path through the attenuation media corresponding the LOR (x_r,θ), or:

$$ACF = e^{+\int_{x_2}^{x_1} \mu(x)dx} \qquad (2.17)$$

The emission sinograms are usually corrected for attenuation by multiplication with the corresponding correction sinograms prior to reconstruction.

The sources used for transmission scanning may be positron emitters or single photon emitters. Using positron emitters (e.g. ^{68}Ge) has many benefits. To begin with, the transmission scan is performed identically to the emission scan and the LOR is determined by the same coincidence processor. As well, because attenuation is energy dependent, the annihilation photons from the transmission source measure the exact same attenuation that affects the emission data. The main problem with using positron emitters is the low transmission coincidence count rates. Given that the probability of one photon being attenuated in the object is high, only a small fraction of the decays in the transmission sources produce coincidence counts. As well, the maximum usable activity used in the sources is limited by the dead-time in the detectors closest to the source, where the photons are not attenuated and the solid angle is high. Therefore, coincidence transmission scans are done at relatively low rates and require long acquisition times to obtain adequate statistics (~15 minutes per bed position). Shorter transmission scans result in poor statistics and a noisy attenuation correction. A second drawback to using positron emitters is that, since the energy of the photons from the emission source and the transmission source are the same, transmission scans acquired post-injection have interference from the emission photons.

The problems of low count rates and post-injection transmission scans are resolved by using single photon emitting sources [45][46], such as ^{137}Cs (662 keV), ^{57}Co (85.6% - 122 keV and 10.6% - 136 keV), or the X-ray beam from a CT scanner [47] (~80 keV). During the transmission scan, the source orbits the object and single photons transmitted through the object are detected on the opposite side of the source, but not in coincidence. This samples the attenuation along the LORs defined by the lines from the point source to the detectors. Counting single photons, without the coincidence requirement, allows for higher activities which increases the count rates, and shorter acquisition times may be used. The photons from the single photon emitting sources are generally at a different energy from the annihilation photons are counted in a different energy window. Thus, the transmission scan may be performed post-injection. However, since the energy of the transmission source is different from 511 keV, the ACFs require scaling to account for the energy dependence of the attenuation coefficients.

The ACFs derived from a transmission scan may require adjustment for inaccuracies in the energy scaling or noise from inadequate counting statistics. One correction method is attenuation image segmentation [48][49]. Segmentation uses the data from the transmission and blank scans to reconstruct images of the attenuation coefficients ("attenuation" or "μ-maps"). These images are then used to determine the boundaries of different material types within the attenuating medium. Once defined, these regions are identified with a specific material, such as air or soft-tissue, and the attenuation coefficient values in each identified region in the image are replaced with the single accepted attenuation coefficients for that material. Thus, the inaccurate values of the attenuation coefficient are corrected, along with the random fluctuations, yielding a noise-free attenuation map. The segmented corrected attenuation images are then forward projected to form noise-free transmission sinograms from which new ACFs are calculated. Segmentation reduces the time required for transmission scans and/or improves the accuracy of the ACFs derived from single photon transmission scans. However, the segmentation process is not without error. Any true small variations in the attenuation values are lost, reducing the accuracy of the ACFs.

2.4.4 Normalization

Variations in the coincidence counting efficiency of detector pairs give rise to non-uniform detection sensitivity. This may be corrected by using the data from a long duration, high statistics normalization scan, acquired using the rotating transmission source(s) or an extended uniform cylindrical phantom [50][51]. A normalization correction factor (*NCF*) is calculated from the scan data for each detector pair or sinogram coordinate:

$$NCF(x_r,\theta) = \frac{N_{norm}(x_r,\theta)}{\langle N_{norm} \rangle} \qquad (2.18)$$

where $NCF(x_r,\theta)$ = normalization correction factors for a given sinogram element.
$N_{norm}(x_r,\theta)$ = measured counts in normalization scan at a given sinogram element.
$\langle N_{norm} \rangle$ = average counts per LOR for all LORs in normalization scan.

The NCFs are applied to each sinogram element on an LOR basis prior to reconstruction.

Normalization in 3D PET is problematic for many reasons. First, long counting times are necessary to accumulate a statistically significant number of counts for each detector pair because the number of LORs in many modern tomographs is very large (10^8 to 10^9). Even with long, high count rate normalization scans, the counts per LOR may be statistically poor. As well, using large volume cylindrical sources require corrections for scatter and attenuation. Therefore, new normalization methods, such as component-based, or model-based normalization, exploit the symmetries in the detector block efficiencies and the LORs to reduce the variance in the normalization correction factors [52][53][54]. These may use individual detector efficiencies, rather than the LOR efficiencies, because there are fewer detectors than LORs.

2.4.5 Scatter Correction

Although the majority of the scattered coincidence events are eliminated by the energy window, a significant fraction may still contaminate the emission data, especially for 3D acquisition. The scattered events may be estimated and subtracted using a number of different schemes [55]. The simplest method estimates a smooth scatter distribution from the tails of the counts in either the sinograms or the reconstructed images. The scatter distribution is then assumed to be either a simple polynomial or a broad Gaussian with the parameters found from the fits to the tails. Once the scatter distributions are estimated, they are subtracted from the emission data. Another simple method assumes that the measured projection data may be modeled as the un-scattered distribution convoluted with a function which describes the effects of scatter [56][57][58]. The scatter function is derived from empirical studies using known cylindrical phantoms. The correction consists of deconvoluting the scatter function from the data.

The scatter correction method which is generally considered as the most accurate is the model-based scatter correction [59] or the "single scatter simulation." [60][61]. In this method, the scatter distributions are estimated by modeling the physics of scatter in the individual subject and the detection in the tomograph. The scatter contribution to each line of response is calculated from a set of randomly positioned scatter points in the preliminary reconstructed radioactivity and attenuation images and is calculated assuming single scatter only. The scatter distribution is scaled

to the tails of the trues distributions and then subtracted from the emission sinograms. This scatter correction may also be incorporated into iterative reconstruction schemes. The scatter correction improves the quantitative accuracy of reconstructed data.

2.4.6 Dead-Time Correction

The count losses from detector dead-time are corrected using correction factors based on the measured single event rates and detector count rate characteristics [62]. The simplest correction method simply scales the counts per LOR by a single global dead-time correction factor. More complex corrections are applied to individual detector blocks or buckets.

2.4.7 Absolute Quantitation Calibration

PET data, if properly corrected and calibrated, are capable of measuring the absolute values of radioactivity concentration. Studies using blood plasma activity as an input function require this calibration but not studies analyzed by ratios or relative values of activity measured in the images.

The activity quantitation calibration requires scanning a cylinder containing a uniform, known radioactivity concentration. A global quantitative calibration factor, CF, is then found by:

$$CF = \frac{\Lambda_o}{\langle N \rangle} \tag{2.19}$$

where Λ_o = measured radioactivity concentration in the cylinder (kBq/ml)
$\langle N_{voxel} \rangle$ = average voxel values reconstructed image (cts/voxel).

This calibration factor is then applied to each voxel in the reconstructed image. The accuracy of the calibrated images depends on the accuracy of all the quantitative corrections.

2.4.8 Image Quality

Even with accurate corrections and calibrations, the accuracy and precision of PET image data are limited by a number of factors. One of the most significant effects is partial volume averaging, which is the blurring of the radionuclide distribution in the image so that structures overlap and

their relative values are convoluted. This occurs when the object or structure being imaged is smaller than the 2-3 times its *FWHM* resolution in the transverse and axial directions [63] [64] [65]. As well, the boundaries of the structures are affected. Partial volume averaging causes a reduction or even loss of the signal from the object. It also results in reduced image contrast and introduces errors in quantitative values which depend on the relative magnitude of the structure and the background activity.

Image quality also depends on image noise. This is largely determined by the statistical fluctuations in the measured counts per line of response. The magnitude of these fluctuations is governed by Poisson statistics, so the standard deviation is proportional to the square root of the counts:

$$\sigma(N) = \sqrt{N} \tag{2.20}$$

where N is the number of counts in a line of response.

However, while the noise in the sinograms is Poisson, the noise in the images is not [66]. The reconstruction process changes the structure of the noise and causes correlations of the voxel values. Reconstruction also increases the noise and causes noise related artifacts.

A few figures of merit are available to assess the image quality produced by PET imaging, some defined in the NEMA standards [25]. These include the signal-to-noise ratio, contrast and contrast recovery. These values may be found from studies using contrast phantoms which consist of spheres of one radioactivity concentration imbedded in a background with the different concentration. The contrast of the image of a sphere with higher radioactivity concentration that the background ("hot sphere") is defined as:

$$Contrast_{hot} = \left(\frac{C_H}{C_B} - 1 \right) \tag{2.21}$$

where C_H = mean counts in a region of interest (ROIs) on the hot sphere.
C_B = mean counts in a region of interest on the background.

The contrast recovery coefficient, CRC, is the ability of the imaging system to recover the actual contrast between the radioactivity concentrations of the spheres and the background, with a maximum of unity. This is defined for a hot lesion as:

$$CRC_{hot} = \left(\frac{C_H / C_B - 1}{a_H / a_B - 1} \right) \qquad (2.22)$$

where a_H = activity concentration in the hot region measured independently (e.g. in a dose calibrator.)
a_B = activity concentration in the background region measured independently.

Another measure of image quality is the contrast-to-noise ratio (CNR), related to the signal-to-noise ratio (SNR). This is often defined as:

$$CNR = \left(\frac{contrast_{hot}}{noise_{bgd}} \right) \qquad (2.23)$$

where $noise_{bgd}$ = the relative standard deviation of the counts in the background region.

The noise in the background is generally assessed by finding the standard deviation of the number of counts between small, identical sized regions of interest placed on the background region. The noise measurement is complicated by the effects of reconstruction and the attenuation and scatter corrections.

Chapter 3

The Theory of Random Coincidences and Corrections

3.1 Single and Coincidence Counting

3.1.1 Chapter Overview

This chapter describes the basic theory and properties of random coincidences, as well as the randoms correction methods used in PET, to establish the requirements of a new randoms correction. The chapter begins with an examination of the relationship between singles and true coincidences and the factors influencing the single distribution. Next, the causes and characteristics of random coincidences are described. Then, the delayed coincidence method of randoms correction is explained and its shortcomings are discussed. Then, suggested variance reduction modifications to the delayed coincidence method and singles-based randoms correction schemes are described. The chapter ends with a discussion of the relative advantages and disadvantages of the new randoms correction methods. **Chapter Four** presents a new model-based method of randoms correction, which is the main subject of this thesis.

3.1.2 Single Photon Detection Events

As described in **Section 1.4**, positron decay and annihilation results in the emission of two collinear 511 keV photons. Each photon detected in the tomograph with energy above the threshold, results in a single event. If both annihilation photons are thus detected, a true coincidence event is also registered. If a solitary photon is detected, only a single event is registered. Most tomographs do not store individual crystal singles count information. However, the singles rates in detector blocks (or groups of blocks) are measured during emission scans.

In general, tomographs have a significantly higher sensitivity for counting single photons than coincidences. This results in considerably higher singles rates than true coincidence rates; usually by one or two orders of magnitude. Since the random coincidences are caused by singles events, the relationship between singles and the true coincidence rates also determines the relationship between randoms and trues in a tomograph. The main reasons for a difference between the singles and coincidence rates are:

- tomograph solid angle and geometric efficiency,

- detector efficiencies, and
- photon scatter (and/or absorption) in object

3.1.3 Tomograph Geometry

The geometric efficiency for 3D coincidence counting is a maximum at the centre of the tomograph and falls linearly to zero at the axial edges (**Section 2.2.2**). The geometric efficiency for single photon counting is the same as coincidence counting at the centre; however, it does not drop off rapidly for sources displaced in the axial direction. Activity outside the axial field of view causes singles events in the tomograph, but no coincidence events. **Figure 3-1 to Figure 3-3** show how the probabilities of single and coincidence events change with axial position.

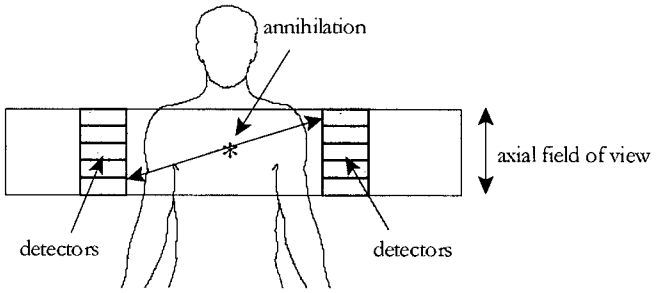

Figure 3-1 Annihilations near the centre of the tomograph have identical geometric efficiency for singles and coincidences.

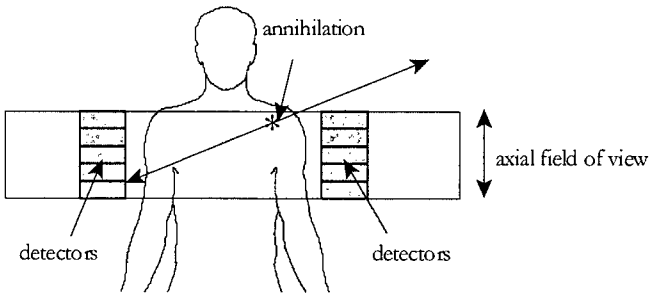

Figure 3-2 Annihilations near the axial ends of the tomograph have similar geometric efficiency for counting singles photons as annihilations near the tomograph centre. However the coincidence counting efficiency is much lower.

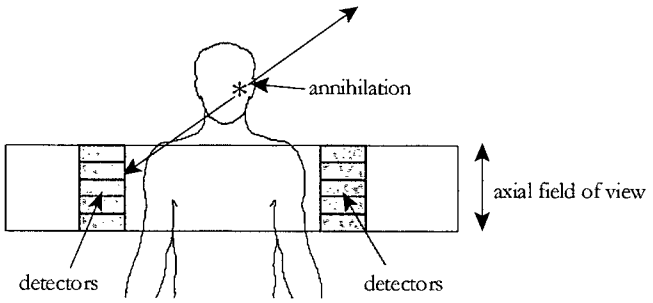

Figure 3-3 Singles events originating from radioactivity outside the axial field of view. These result in single events, but not true coincidences

The relationship between the theoretical singles and coincidence geometric efficiencies for a point source in a tomograph (8 cm axial FOV, 15 cm ring diameter) as a function of axial position are shown in **Figure 3-4.** The singles efficiency does not change dramatically with axial position.

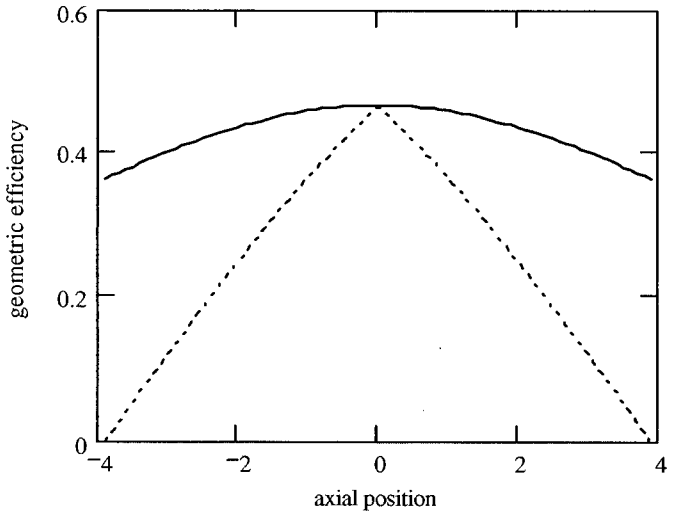

Figure 3-4 The theoretical singles (solid red line) and coincidence (dotted blue line) geometric efficiencies for a point source as a function of axial position.

3.1.4 Detector Efficiencies

The second factor in the difference in between singles and coincidence sensitivity is the detector efficiencies. The singles sensitivity depends on the detector efficiency, but the coincidence sensitivity depends on the square of the detector efficiency, since two photons are independently detected. This again reduces the coincidence sensitivity relative to the singles sensitivity, and the difference is greatest with lower detector efficiencies. As well, dead-time affects singles and coincidence events differently.

The relationship between theoretical singles and coincidence sensitivities for a point source in a tomograph (8 cm axial FOV, 15 cm ring diameter, detector efficiency = 25%) as a function of axial position is shown in **Figure 3-5**. The singles sensitivity is shown to be significantly higher than the coincidence sensitivity.

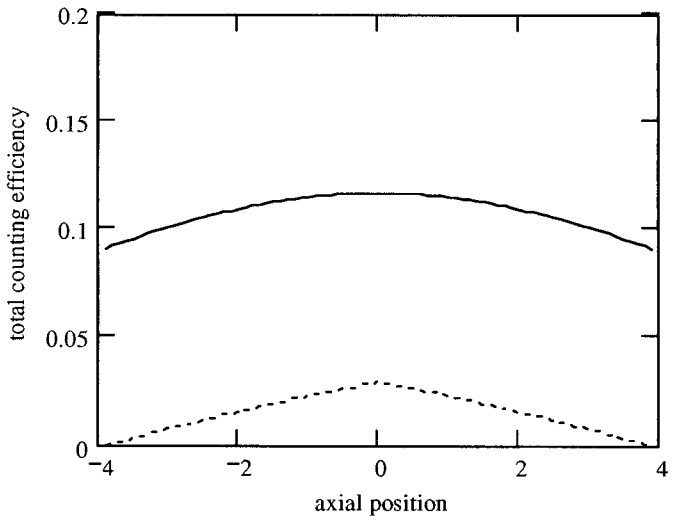

Figure 3-5 The theoretical singles (solid red line) and coincidence (dotted blue line) total sensitivities for a point source as a function of axial position. The total sensitivity depends on both the geometric efficiency and the detector efficiencies.

3.1.5 Photon Interactions in the Object

Photon interactions in the object also affect the single and coincidence counting differently. At 511 keV, the main photon interaction processes are Compton scattering and photoelectric absorption. In water-equivalent material, such as soft tissue, Compton scattering dominates and photoelectric absorption is negligible (only 0.02% of interactions). The probability of "Compton-absorption" in the object (one or more Compton scatters followed by absorption) is slightly higher but still not significant.

The major cause of count losses due to interactions are scattered photons either missing the tomograph or being detected with energies lower than the energy threshold. These processes affect both singles and coincidences. However, if one of the annihilation photons is lost, a single event may still be detected, while no coincidence would be counted, as shown in **Figure 3-6**. Scatter also affects the distribution of detected single photons, as described in **Section 4.6.**

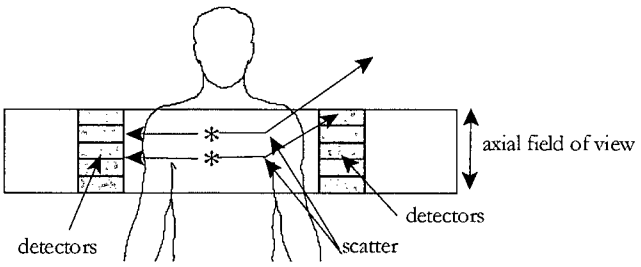

Figure 3-6 Singles events originating from physical interactions. Annihilations occur within the detector volume which should cause both photons to be incident on the tomograph. However Compton scatter causes the loss of one photon. However, a single event may still be detected.

3.1.6 The Singles Distribution

The detected individual annihilation photons create a distribution of singles rates in all the detectors of the tomograph. The singles distribution for a given scan depends on the radioactivity distribution, the attenuating object and the tomograph response. In 3D acquisition, the singles

distribution includes contributions from scattered photons and photons from activity outside the field of view.

In general, the distribution of single photons in the tomograph is slowly changing because the singles geometric efficiency changes smoothly. For a long cylindrical uniform source centred on the tomograph axis, the singles distribution is uniform. Non-uniform distributions of radioactivity and/or attenuating material cause low frequency variations in the singles distributions. The distribution of singles rates is also affected by variations in individual crystal efficiencies.

3.2 Random Coincidences

Random coincidences occur when two single events from different annihilations are detected within the coincidence timing window of the tomograph and are counted as a coincidence event [72] (**Section 1.4.6**). This gives a spurious count in the line of response between the two involved detectors. If three or more singles are in coincidence, a "multiple" coincidence occurs. In some systems multiples are ignored; in other systems one count is assigned to one possible LOR by an arbitrary process. Multiples have a much lower frequency than randoms.

3.2.1 Randoms Rates

Singles events are distributed randomly in time but described by an average count rate. If the time required to process a singles event is ΔT, the fraction of the time that a detector is counting singles is given by:

$$f_{s1} = R_{s1}\Delta T \qquad (3.1)$$

where f_{s1} = fraction of the time detector 1 is processing singles (unitless).
R_{s1} = singles rate at detector 1 (counts per second).
ΔT = singles event processing time (processing time per count).

If a second detector is also counting singles, the average rate at which events are counted in both detectors, and, therefore, the rate of random coincidences, R_r, is given by:

$$R_r = f_{s1} R_{s2} = R_{s1} R_{s2} \Delta T \qquad (3.2)$$

From the perspective of analog timing electronics, a coincidence involves the overlap of the two pulses. This occurs if the pulses are within ± 1 pulse width, τ, of each other. Therefore, the effective coincidence timing window is the sum of the two pulse widths, 2τ. In modern tomographs with digital processors, the coincidence is tested by comparing the time tags of buffered singles events with the value of the coincidence timing window, T_{CTW}. Therefore, the equation for the randoms rate may be written as:

$$R_r = R_{s1} R_{s2} 2\tau = R_{s1} R_{s2} T_{CTW} \qquad (3.3)$$

where 2τ = 2 x coincidence resolving time or pulse width. This notation is often retained the literature
T_{CTW} = time width of the coincidence timing window.

T_{CTW} is set by the user and its optimal value depends on the coincidence timing resolution of the tomograph, which is related to the scintillator decay constant and the tomograph detector design. For LSO systems T_{CTW} = 5-6 ns is used but older systems with other scintillators have timing windows up to 15 ns.

3.2.2 Randoms Distribution and Randoms Fraction

Since the randoms rates between detectors depends on the singles rates, the spatial distribution of randoms within the tomograph LORs depends on the singles distribution. In general, the randoms distribution is smoothly changing. A uniform singles distribution results in a uniform randoms distribution within a slice plane. However, detector efficiency variations cause sharp discontinuities, in the form of diagonal lines, in the randoms sinograms. Axially, in 3D acquisition, the total randoms rates within a slice plane decrease towards the axial ends of the tomograph.

While the relative distribution of randoms is independent of the activity in the subject, the magnitude of the randoms relative to the trues is not. The contribution of the random coincidences compared with the true events is quantified by randoms fraction (RF):

$$RF = \frac{R_r}{R_t + R_r} \tag{3.4}$$

where R_r = rate of random coincidences.
R_t = rate of true coincidences.

Both the singles and trues rates scale linearly with the total activity in the object (neglecting dead-time losses). The randoms rates depend on the square of the singles rates **(3.3)**, and therefore, on the square of the activity. Thus, the randoms fraction increases with activity of the object. Similarly, the RF drops over the duration of the scan as the activity decreases. Equation **(3.3)** also implies that the randoms rates and the randoms fraction also depend on the coincidence timing window.

3.2.3 Effects of Randoms

Random coincidences have three main effects on PET studies. Qualitatively, they form a smooth background in the image, which reduces the contrast. Quantitatively, they add counts to the LORs, increasing the measured values in a non-uniform manner, thus creating inaccurate values and biases. As well, randoms are an additional independent component of the measured data set, and, as such, the noise in the randoms contributes to the noise of the data. In all cases randoms degrade the quality in the image data. The effect of randoms on PET image data is quantified in the noise equivalent count rate (NECR) **(2.6)** (**Section 2.2.3**).

Therefore, in PET imaging, random coincidences should be minimized where possible through the design of the tomograph or imaging protocol. Likewise, the randoms should be subtracted from the image data. Since the randoms distribution is not uniform, it may not be simply subtracted or re-scaled and, instead, requires a more accurate correction.

3.3 Delayed Coincidence Measurements of Randoms

The random coincidence rates in a detector pair may be estimated by two different direct measurements: the rate of delayed coincidences or the singles rates in the individual detectors. These measurements require dedicated electronics and, in some cases, data storage requirements beyond those for basic coincidence imaging. However, most tomographs have the capability for at least simple delayed coincidence measurements.

3.3.1 The Delayed Coincidence Measurement

The single events that produce true coincidences are correlated in time because the detected photons are produced by the same positron annihilation. There is may be a slight time delay given the potential differences in travel time, photon detection time and event processing time, but this difference is smaller than the coincidence window width. Therefore, the true coincidences are measured in a real-time or "prompt" coincidence window. However, random coincidences also contribute to the counts measured using this window. The

The single events that produce randoms are not time correlated, so the randoms rate in a coincidence window does not depend on the relative time at which the photons are detected. The random rate measured in a time delayed coincidence window would be the same as that measured in the prompt coincidence window. If the time delay is long enough (e.g. 64 to 128 ns), no true coincidences would be measured. Therefore, the count rate measured in a delayed coincidence window may be used to estimate the contribution of randoms to the coincidences in the prompt window. This measurement provides a direct method of randoms subtraction.

3.3.2 Prompts and Delays

The coincidences measured in the prompt window are denoted as "prompts" while those measured in the delayed window are called "delays." These two measurement channels have different content. Prompts include both the true coincidence counts and the random coincidence counts that occurred within the prompt coincidence window. Thus:

$$N_P = N_T + N_R \tag{3.5}$$

where N_P = number of prompt coincidence counts.
N_T = number of true coincidence counts.
N_R = number of random coincidence counts in the prompt window.

While the term "trues" sometimes refers to unscattered photons, here it refers to true coincidences as opposed to random coincidences. Thus, "T" includes both unscattered and scattered coincidences, since scattering does not affect the time correlation of the two photons.

The measured delayed coincidences contain only random coincidences. Thus,

$$N_D = N_{R'} \tag{3.6}$$

where N_D = number of delayed coincidence counts
$N_{R'}$ = number of random coincidence counts in delayed window.

Thus, the randoms fraction, RF, **(3.4)** could be estimated as:

$$RF = \frac{N_D}{N_P} \tag{3.7}$$

The prompts are corrected for randoms by simply subtracting the measured delays from the measured prompts for each detector pair or line of response:

$$N_{T'} = N_P - N_{R'} \tag{3.8}$$

where $N_{T'}$ = number of corrected true coincidence counts.

In older systems, the delays were measured in a separate coincidence circuit and subtracted from the acquired prompts counts during acquisition. In some newer tomographs, the digital coincidence processor compares the detection times of buffered single events, so prompt and

delayed coincidences are determined in the same processing step. Again, the delays may be subtracted from the acquired prompts counts during acquisition. Some tomographs store the prompts and delays in separate histograms or in list-mode events flagged as prompts or delays.

The delayed coincidence measurement gives a simple, yet elegant, method of randoms correction. Since the delayed events have the same processing (e.g. energy window, coincidence timing, dead-time), the method is highly accurate. However, in general, randoms subtraction increases the noise in the true data estimate. As well, when the randoms fraction is high, the subtraction from the prompts may leave the trues poorly determined. This may be especially problematic when measuring short time frames and the randoms rates are high.

3.3.3 Noise from Delayed Randoms Correction

Although the randoms distribution and mean rates measured in the delayed window are identical to those contributing to the coincidences in the prompt window, the noise content is different. The variance of the prompts includes contributions from the trues and one estimate of the randoms:

$$\sigma_P^2 = \sigma_T^2 + \sigma_R^2 \tag{3.9}$$

where σ^2_P = variance of the prompt coincidences.
σ^2_T = variance of the true coincidences.
σ^2_R = variance of the random coincidences in prompt window.

The variance in the delays is from a second, different estimate of the randoms:

$$\sigma_D^2 = \sigma_{R'}^2 \tag{3.10}$$

where σ^2_D = variance in delayed coincidences.
$\sigma^2_{R'}$ = variance in random coincidences in delayed window.

The subtraction of the delays from the prompts increases the variance of the resulting trues because R and R' are different estimates of the randoms rate. Thus, the variances of the randoms in the prompts and in the delays do not cancel, but sum, resulting in:

$$\sigma_{T'}^2 = \sigma_P^2 + \sigma_D^2 = \sigma_T^2 + \sigma_R^2 + \sigma_{R'}^2 = \sigma_T^2 + 2\sigma_R^2 \qquad (3.11)$$

If the randoms fraction is small, the contribution of the subtracted delays to the image noise is generally insignificant. However, in short scans done with high activity, the randoms fraction may be very high (~50%). In such cases, the variance in the delays may contribute significantly to the noise in the corrected trues. As well, in high resolution tomograph designs with a very large number of LORs (e.g. Siemens HRRT, 4.5 billion LORs), the coincidence counts acquired per LOR will be low, resulting in large variance in both the prompts and the delays. Therefore, correcting the raw measured prompts with the raw measured delays may greatly increase the noise in the image data.

In contrast, if the subtracted randoms estimate was noise-free, (i.e. $\sigma^2_{R'}=0$), the overall variance would be reduced to the variance in the prompts:

$$\sigma_{T'}^2 = \sigma_T^2 + \sigma_R^2 = \sigma_P^2 \qquad (3.12)$$

Therefore, the randoms correction method affects the signal-to-noise ratio of the PET data. This is quantified in the NECR (**Section 2.2.3**). Recall that the NECR **(2.6)** is defined as:

$$R_{NEC} = \frac{R_t^2}{R_t + R_{sc} + k_{rand} R_{sc}} \qquad (3.13)$$

The constant k_{rand} is assigned a value of 2 when simple delays subtraction is used because the variance of the randoms is added twice **(3.11)**. A value of 1 is used when the randoms correction method is essentially noiseless. Randoms correction with reduced variance sets $1 < k_{rand} < 2$. Studies optimizing the NECR have identified the noise from measured delayed coincidence randoms correction as limiting factor in 3D PET high count rate performance [67]. Therefore, reducing the variance introduced by the randoms correction may provide significant improvements in the quality of PET image data.

3.3.4 Randoms Correction with Reduced Variance

Randoms corrections with noise reduction have followed three basic directions. The first is to fit the background outside the body to a smooth function and subtract it post-acquisition [69]. This background is caused by the combined scatters and randoms and is expected to be slowly varying compared to the trues distribution. This estimate is essentially noiseless and requires no additional measurements. However, it is prone to significant biases, especially for asymmetric randoms distributions or high randoms fractions. It also does not account for high frequency structure in the randoms distribution, such as that caused by detector efficiency variations. Similarly, a related method uses the deconvolution of smooth scatter and randoms response functions from the data [70]. These functions are determined by either phantom or simulation studies. Again, although no noise is added, large biases may be introduced.

The second direction for low noise randoms correction is to reduce the variance in the measured delayed coincidences by combining the delays from LORs involving the same detector. Variance reduction techniques are described in **Section 3.4**. The third direction is to estimate the randoms from the measured detector singles rates. Since the single rates are two or more orders of magnitude higher than the randoms rate, the estimated randoms from singles have lower variance. Singles-based randoms correction methods are described in **Section 3.5**. Variance reduction and singles-based randoms correction are then compared in **Section 3.6**.

3.4 Variance Reduction of Measured Delayed Coincidence Estimates

3.4.1 Introduction

A number of methods of reducing the variance of the randoms measured in the delayed coincidence window have been investigated. The simplest method is to acquire the randoms in separate sinograms and then smooth them prior to subtraction [71]. While this technique would reduce the variance, it would also attenuate the high frequency components of the randoms data,

mainly caused by the efficiency variations in the crystals, and thereby introduce biases [72]. More sophisticated smoothing approaches are required to prevent artifacts in the reconstructed images.

The problem of randoms variance reduction is almost identical to that of variance reduction in efficiency normalization. Many techniques developed for randoms correction are readily applicable normalization and visa versa. Variance reduction usually involves the measured counts in sets of LORs involving the same detectors to increase the total counts involved. Exploiting the symmetries of the involved LORs, the randoms rates of particular LORs may then be extracted.

3.4.2 The Basic Method of Casey and Hoffman

The seminal variance reduction technique is that first proposed by Casey and Hoffman in 1986 [73]. This scheme sums the randoms rates between one detector and a group ("bank") of opposing detectors. The randoms rate, $R_{r,i,sum(j)}$, between detector i on one side of the tomograph and a bank of N detectors j, on the other, may be decomposed into the contributing singles rates:

$$R_{r,i,sum(j)} = R_{s,i} \sum_{j=1}^{n_{bank}} R_{s,j} 2\tau \tag{3.14}$$

where $R_{s,i}$ = singles rate in detector i.
n_{bank} = number of detectors in one "bank."
2τ = coincidence timing window.

Likewise, the randoms rate for the other bank of detectors may be decomposed into:

$$R_{r,j,sum(i)} = R_{s,j} \sum_{i=1}^{n_{bank}} R_{s,i} 2\tau \tag{3.15}$$

The total randoms between both banks would be:

$$R_{r,sum(i),sum(j)} = \sum_{i=1}^{n_{bank}} R_{s,i} \sum_{j=1}^{n_{bank}} R_{s,j} 2\tau \tag{3.16}$$

From the product of **(3.14)** and **(3.15)** normalized by **(3.16)** the original randoms rate between two individual detectors is recovered:

$$R_{r,i,j} = R_{s,i}R_{s,j}2\tau = \frac{R_{r,sum(i),j}R_{r,i,sum(j)}}{R_{r,sum(i),sum(j)}} \tag{3.17}$$

In other words, the randoms rate between two individual detectors may be found from the normalized sum of groups of detectors including the pair of interest. Since the rates are summed the total counts increase; thus, the variance in the estimated randoms rate is reduced. The improvement in the variance depends on the number of detectors in the group (bank), n_{bank}. The ratio of the variance when using a single LOR $\sigma^2(1)$ to that when of using a group of n_{bank} LORs $\sigma^2(n_{bank})$ is:

$$\frac{\sigma^2(1)}{\sigma^2(n_{bank})} = \frac{n_{bank}^2}{2n_{bank}+1} \tag{3.18}$$

For example, if a group of 64 detectors is used in this scheme, the variance is reduced by a factor of 32. Therefore, improvements in reducing randoms variances come from choosing larger, but appropriate, groups of detectors to use in the sum.

3.4.3 Variance Reduction Including Full 3D Data

The basic method of Casey and Hoffman used only banks of detectors from the same slice, that is, contributing to the same sinogram. This technique was also limited to using the randoms rate per LOR rather than the singles rate per detector. Improved versions of this technique involve more detectors in a single-plane and/or detector pairs from oblique LORs in 3D acquisition. These methods were originally developed for normalization variance reduction [53]. Individual techniques differ by whether they include single-plane or 3D coincidences, are exact or approximate, and if the correction is based done for individual detectors or LORs.

The effectiveness of three of these techniques on randoms variance has been assessed for systematic accuracy and variance reduction efficacy in phantom and clinical studies [74]. All three methods showed reduction in variance. The one method that made a-prior assumptions about the singles distribution showed a low frequency bias, but the other two did not. Phantom measurements found that variance reduction increased the signal-to-noise from ~5% to ~15% for the specific tomograph used in the study operating in 3D acquisition.

Another randoms variance reduction scheme uses a Bayesian estimation method to compute the statistical mean values for each pixel of the randoms sinogram [75]. This was used to incorporate randoms smoothing into the Maximum a' Posteriori (MAP) reconstruction method. The smoothed randoms sinogram was estimated from the measured randoms sinograms and the intrinsic detector efficiencies extracted from blank transmission scan data. However, it was later found that the singles detector efficiencies extracted from trues coincidence data had significant difference from the singles efficiencies involved in random coincidences and the method was changed [76]. Instead, a maximum-likelihood (ML) estimate of the mean singles rate at each detector is calculated, from which a mean randoms sinogram is found. This method is admitted to be similar to that of Casey and Hoffman, except that a true ML estimate is used. The variance reduction resulted in lower visible noise in the sinograms. As well, when high and low count randoms data were both corrected by this method, there was only a small percentage squared difference between them. Biases introduced from this method were not assessed.

3.5 Singles-based Corrections

3.5.1 Introduction

The contribution of randoms coincidences to the measured prompt coincidences in a line of response may also be estimated indirectly through the measured detector singles rates. The randoms rate for the line of response joining any two detectors is given by **(3.3)**.

A number of singles-based randoms correction methods have been developed for different systems, each designed to work within the technical limitations of the device. For example, a number of singles-based randoms corrections were proposed for dual-head coincidence imaging systems which could not measure delayed coincidences [77] [78]. Only the most important singles-based methods for dedicated PET are reviewed below.

3.5.2 Singles-based Randoms Correction for Dedicated PET Tomographs

The most direct method of singles-based randoms correction for dedicated PET tomographs is to measure the singles rate per detector during acquisition. One early investigation of this technique used a PENN-PET 240H tomograph with large area NaI(Tl) detectors [79]. In this method, the singles distribution is first measured across the detectors in a separate scan because detector singles rates are not normally stored by this tomograph. Then, the randoms sinograms were calculated using **(3.3).** These were then scaled using an empirically determined relationship between randoms rate and singles rate and subtracted prior to reconstruction. For phantom and human studies, the resulting calculated randoms rates reproduced the values measured by delayed coincidence to within 17%. Unsurprisingly, phantom and human studies corrected with this method showed improved contrast compared to those corrected with a smooth background subtraction.

Singles-based randoms correction was also developed for the G.E. Advance™ dedicated PET camera [80]. For each detector, the count information is stored for every single event that meets the energy threshold requirement. Therefore, the singles distribution is directly measured and the resulting randoms rates may be calculated from **(3.3).** The accuracy of this method was tested by comparing the total measured delayed randoms counts in six slices of a patient study to those calculated from the singles. In these slices, the randoms counts rates agreed to within $\leq 0.25\%$ for both 2D and 3D patient data sets. The randoms counts per sinogram pixels were also compared. The pixel values measured by delayed coincidence were found to be Poisson distributed about the corresponding pixel values from the calculated sinograms, suggested that the differences were due mainly to noise rather than biases. The authors conclude that the method is highly accurate

compared to the delayed coincidence method. No estimate of the noise reduction efficacy was made.

In most tomographs the singles counts per crystal are not measured or stored during acquisition. However, the singles rate per detector block or bucket (group of four detector blocks) is measured and usually stored in the data file header. One method of singles-based randoms correction uses the measured singles rate per bucket [81]. It begins with the assumption that the ratio of the randoms rate in a detector pair to the product of the singles rates in the buckets containing the detectors is a constant. First, a high statistics reference scan is performed using a uniform elliptical phantom to produce a low variance randoms sinogram. Then, a singles sinogram is calculated for each crystal pair using the average bucket singles rates. This requires smoothing at the abrupt edges caused by the borders of the buckets. The measured and calculated sinograms are then divided to produce a correction sinogram. This correction sinogram takes into account the relative crystal efficiencies.

During subsequent scans only the bucket singles rates are required. The randoms sinogram used for correction is created by first calculating a preliminary randoms sinogram using only the bucket singles rates. This sinogram is multiplied by the predetermined correction sinogram. Therefore, clinical studies only required bucket singles rates for randoms correction, not delayed coincidences or individual detector singles. However, this method is prone to biases arising from the averaging of the singles rates over groups of detectors, rather than using individual crystal singles rates. As well, biases may be introduced by the calibration sinogram.

This method reproduces the total measured randoms rates to within 5% for a variety of imaging situations. Sample calculated randoms distributions profiles show visual agreement with measured randoms, but contain less noise. The sinograms also show lower standard deviation than those from delayed coincidence measurements. Finally, this method was shown to increase the NEC rates by up to 25% for clinical studies, compared with delayed coincidence measurements.

In a similar method [82], a reference scan is not used. Instead, the measured intrinsic detector efficiencies from component-based normalization data [54] are used to account for the differences in crystal singles efficiencies. However, this introduces a bias if there is any difference between singles and coincidence events in pulse-pileup, dead-time or energy discrimination. This method also suffers from the same biases as the previous method, caused by the averaging the singles over groups of detectors. However, this bias is modeled in a global scaling factor that varies with detector singles rates (to account for dead-time differences and the effects of patient size). The randoms are calculated from the singles using a variant of **(3.3)**:

$$R_{r,i,j} = \varepsilon_i R_{s,i} \varepsilon_j R_{s,j} \alpha(R_{s,i}, R_{s,j}) T_{CTW} \qquad (3.19)$$

where ε_i = singles efficiency for detector i.
$a(R_{s,i},R_{sj})$ = global scaling factor.

This method showed improvements in the signal-to-noise ratio (SNR) for contrast phantoms, similar to those obtained by variance reduction. However, biases resulted in large variations in the correction factor; $a(R_{s,i},R_{sj})$ was found to vary from 0.80 to 1.13 for objects varying from the size of a head to that of an abdomen.

3.6 Discussion of Low Variance Randoms Correction Methods

3.6.1 Issues with Smoothed-Delays Randoms Correction

While variance reduction is effective, it requires the measurement, storage and manipulation of the delayed coincidence data. The measurement of delayed coincidences increases the demands on the tomographs coincidence processor which results in higher dead-time. This limits the count rate capabilities of the system. As well, the delays require separate storage before subtraction which increases the data storage demands, whether the data are directly binned in histograms or stored in

list mode. Variance reduction also requires that the delays measurement be pre-processed before subtraction which increases the computing time necessary to produce the final image.

The gains from randoms variance reduction depend on the number of detector pairs included in the summation. Some methods have inherent biases if they make assumptions about the uniformity of the singles distribution, or if they require singles detector efficiencies. These biases may ultimately affect the accuracy of the randoms correction. Finally, the achievable variance reduction is still limited by the number of measured delays. In the cases of short scans or large number of LORs, these may still be small.

3.6.2 Issues with Singles-based Randoms Correction

The singles-based randoms correction method requires the measurement and storage of the singles counts for every crystal, rather than measured delayed coincidences. This frees up the coincidence processor and reduces the storage demands by a factor of two. Unfortunately, most tomographs do not presently have the capabilities to measure and store individual crystal singles counts. Some singles-based methods require only the measured singles rates for blocks or buckets, which are often already available, so that the data measurement and storage demands are not significantly increased. However, using the larger groups of detector introduces biases due to variations in the singles distributions over the crystals in a block and due to differences in the relative crystal efficiencies.

Other subtle issues may affect the accuracy of a singles-based estimate of randoms. First, the singles must be measured with the same signal processing parameters (preamplifier gain, energy window, and digitization) as the coincidence events; otherwise, the singles would yield an estimate of the randoms under different conditions. The singles must also experience the same dead-time losses or be accurately corrected for dead time. Since dead-time is mainly attributable to scintillator decay, the dead-time experienced by single and coincidence events is comparable, provided the coincidence processor does not significantly increase the dead-time. As well, in tomographs with

intrinsic radioactivity in the detectors, such as LSO, the constant singles background must be taken into account in the randoms correction.

3.6.3 Assessment of Variance Reduced Randoms Correction Methods.

An assessment of the effects of the different variance reduction randoms correction methods on data and image quality has been performed by Brasse, et al [82]. This work compared the impact of smoothed-delays and singles-based randoms correction. They concluded that both methods increased the NECR, leading to improvements in the image SNR of about 15% for both filtered backprojection and iterative reconstruction. Although this improvement is unnoticeable in the images, it is caused by increasing the NECR by 32%. This study concluded that if the original image SNR is acceptable, the reduced variance in the random correction would allow a 25% reduction in the patient scan times. The study also found that the singles-based method performed marginally worse than the smoothed-delays method because of biases from using singles rates from large numbers of detectors.

In summary, randoms variance reduction is of value in reducing the noise in the image data. While single-based randoms correction reduces the workload of the coincidence processor and the data storage demands, the method is subject to biases if single counts are not recorded for each crystal. As well, if the singles and coincidence counts are not processed identically, other biases may occur.

Therefore, a new singles-based randoms correction has been developed. In this new method, the single events in each crystal are found from a model-based calculation, so that no biases are introduced by averaging over many detectors. Also, no measured singles distributions are required because the singles are calculated only from the preliminary reconstructed activity and attenuation images, making this method applicable to any coincidence imaging device. The singles distribution is smooth, so that the randoms distribution used for the correction is essentially noiseless (i.e. $k_{rand} \approx 1$ in the NECR equation). This novel model-based randoms correction is the subject of **Chapter Four** and the remainder of this thesis.

Chapter 4

A Model-Based Approach to Randoms Correction

4.1 Introduction

4.1.1 Chapter Overview

This chapter details the theory of the model-based randoms calculation, beginning with an overview of method. Then, the details of the model-based singles distribution computation are given, including the calculations of the solid angle, photon survival and the detector efficiencies. The effects of photon scatter in the object on the calculations are then described. The chapter ends with an explanation of the how the randoms distribution is calculated from the singles and the scaling required before subtraction. **Chapter Five** describes the specific implementation of this method for the MicroPET R4 tomograph.

4.1.2 Overview of the Method

The model-based random correction is a post-acquisition method of estimating the randoms distributions from calculated singles distributions. The calculation uses only the preliminary reconstructed images of the radioactivity distribution and the attenuation coefficients and the measured global singles rate. Neither delayed coincidence data, nor individual crystal singles data are required. The calculated randoms distributions are smooth and therefore do not increase the noise in a randoms subtracted data set.

The heart of this method is the model-based calculation of the singles distribution. This method differs from traditional Monte Carlo calculations in that the histories of individual photons are not followed in detail. The probabilities of detecting singles and trues are calculated from modeling the single photon detection probability rather than by following a large number of photon histories. This increases the computational efficiency and reduces the calculation times. Thus, the method is comparable to model-based scatter correction [59][61] and normalization [52] schemes. It is also similar to other model-based simulations [83], except that the randoms correction calculation is driven by the data.

The following is a broad outline of the randoms calculation, with the details explained in the rest of the chapter. A set of activity sample points is generated within the radioactivity and attenuation

images. The contribution of each point to the singles rates at each detector in the tomograph is then calculated, taking into account the activity at the point, the probability of photon attenuation in the object, the detector solid angle and intrinsic efficiency, and the acquisition energy window. The effects of photon scatter are included in the attenuation and detector efficiency calculations. The total singles distribution is the sum of the contributions from all the activity sample points.

The calculated singles distribution is scaled to the measured average global singles rate. Then, the randoms rate per LOR is calculated from the singles distribution for every LOR acquired by the tomograph. The calculated randoms distribution is spatial variant. Finally, the total number of randoms events for the given acquisition time is calculated and the randoms are subtracted from the prompts data. The randoms corrected data may then be reconstructed normally.

The method may be applied to static or dynamic data sets. For dynamic data, a radioactivity image must be reconstructed, and a different randoms correction calculated, for each time frame.

4.2 Singles Distribution Calculation

4.2.1 The Preliminary Radioactivity and Attenuation Coefficient Images

The first step in the model-based randoms calculation is the preliminary reconstruction of the radioactivity distribution and attenuation coefficient images from the measured emission and transmission data. Since no delays are measured or subtracted, the emission data consist of prompts. The prompts sinograms are corrected for attenuation, normalized, and then reconstructed using standard reconstruction techniques. An accurate attenuation image is required for both the attenuation correction and for calculating photon survival in the singles calculation.

4.2.2 Generation of Activity Sample Points

The positions of the activity sample points are found by randomly generating x, y, and z locations within the volume of the activity distribution. The positions are absolute and are not discretized to the voxel centres. The total number of points generated is determined by the pre-defined *sampling*

density (sample points per ml). Increased sampling density improves the accuracy of the singles distribution calculation, but at the expense of increased computation time. The optimal sampling density is the smallest value that produces negligible differences between identical calculations of the singles distributions.

To improve the computational efficiency, a threshold is used to remove the sample points with low relative activity values from the sample set used in the calculation. The activity values of the sample points are still used in the calculation of the singles distribution; the threshold sampling simply determines the lowest activity used in the calculation. The threshold value is set as a percent of the maximum reconstructed activity value. The threshold also has the benefit of removing points in the background (randoms or scatter) from the calculation if the threshold is high enough. The optimal radioactivity threshold setting may be determined empirically by adjusting it so that there are no generated sample points outside the boundaries of the object. **Figure 4-1** shows a set of activity sample points from a small bottle with uniform radioactivity.

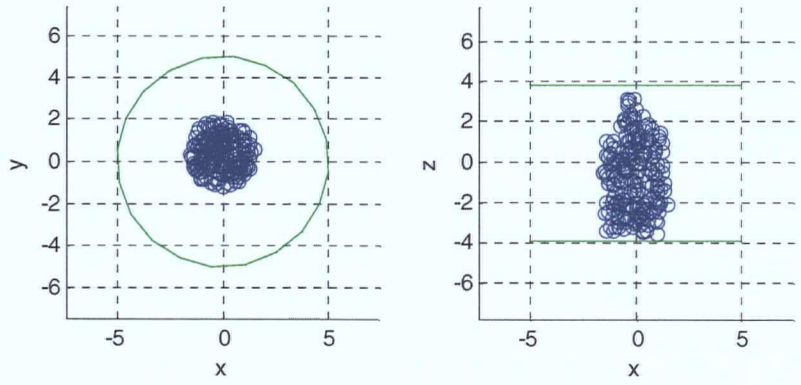

Figure 4-1 A set of randomly positioned radioactivity points (blue circles) from a uniform cylindrical bottle with a neck. The green circles and lines show the FOV of the tomograph.

The total number of sample points used in the singles calculation depends, not only on the sampling density and the threshold, but also on the activity distribution. A greater dynamic range

of activity concentration values requires a lower threshold for accurate results. This translates into more points for a given sampling density. In general, the singles calculation requires a few thousand points for accurate results when a complex activity distribution is used. The results of testing the values of the threshold and sampling point density are described in **Section 6.3.4**.

The random nature of the activity image sampling, along with the statistical noise in the image, causes differences between each realization of the calculated singles distribution even when the calculation parameters are identical. These variations do not appear as random fluctuations in the individual pixel values. Instead, they cause small differences in the overall smooth shape of the calculated singles distributions between otherwise identical calculations. Thus, noise in the radioactivity image manifests itself in small biases in the singles distribution. As well, different sets of activity sampling points lead to small differences in the calculated singles distributions between realizations. The magnitude of the random biases from both processes depends on the sampling parameters and is inversely related to the number of sample points used in the calculation.

4.2.3 Single Photon Detection Probability

Once generated, the set of activity sample points is used as the radioactivity distribution from which the singles distribution is calculated. The probability of detecting single photons originating at each sample point is calculated for every detector in the tomograph using an analytic calculation based on a detection model that includes the:

- solid angle and other geometric effects,
- photon attenuation based on the reconstructed attenuation map, and
- detector efficiencies.

Thus, the probability of annihilation photons from activity sample point, i, being counted by a detector, A, is:

$$P_{det,i,A} = \frac{1}{4\pi}\Omega_{i,A}P_{surv,i,A}\varepsilon_{i,A} \qquad (4.1)$$

where $\Omega_{i,A}$ = solid angle of detector A from sample point i.
$P_{surv,i,A}$ = photon survival probability in object from i to A.
$\varepsilon_{i,A}$ = efficiency of detector A for photons originating at i.

The calculation of the singles distribution uses **(4.1)** for the primary annihilation photons. However, the trues distribution may be simultaneous calculated if the detection probability of the annihilation partner photons is also found. This additional computation was included to provide an additional test of the accuracy of the photon detection model, but does not directly impact the randoms calculation.

4.3 Geometric Calculations

4.3.1 Introduction

A Cartesian coordinate system is used for the solid angle calculations. In the right handed Cartesian coordinate system, the transverse slices are in the x-y plane and z is the axial direction, with the positive direction being from back to front. The detectors in the tomograph form a cylindrical detection surface, as shown in **Figure 4-2**.

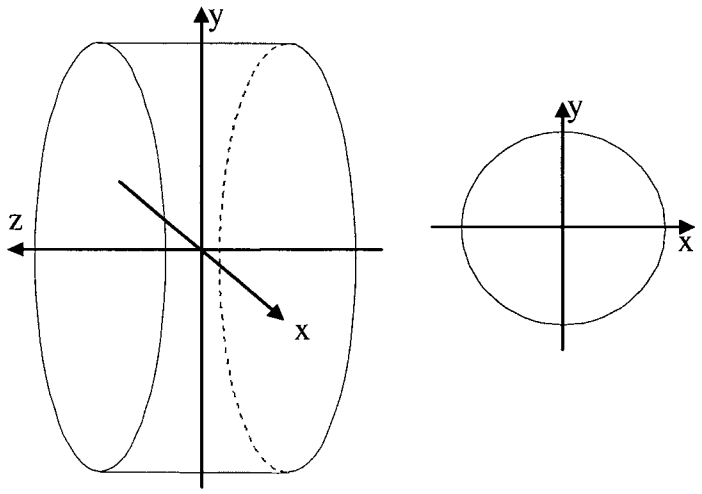

Figure 4-2 The coordinate system for a cylindrical dedicated tomograph. The z-axis goes from back to front.

The scintillator material forms an annular volume with the inner radius = the radius of detector ring, r_{ring} and the outer radius = $r_{ring} + x_{det}$, where x_{det} = detector thickness. Each detector crystal corresponds to a square or rectangular area on the inner cylindrical surface of the tomograph. Most tomographs also have an electronically defined FOV within the detector ring that defines the radial limit of accepted LORs and, therefore, the radial extent of the sinograms. The axial FOV is defined by the z extent of the tomograph. The relationship between these physical dimensions is shown in **Figure 4-3**.

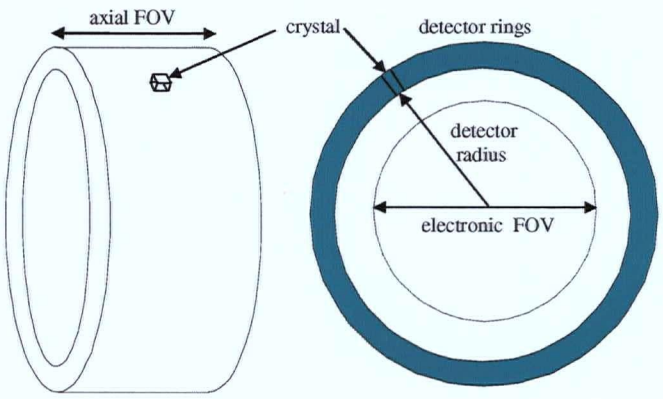

Figure 4-3 The tomograph physical parameters relevant to the solid angle calculation. Note that the crystal dimensions are not to scale.

4.3.2 Solid Angle of the Primary Photon

The probability of counting a photon in a given detector, A, depends first on the solid angle presented by the crystal to the activity sample point. The solid angle is given by:

$$\Omega_{i,A} = \iint_S \frac{\hat{\boldsymbol{n}} \cdot d\boldsymbol{\sigma}}{r^2} \approx \frac{\sigma_A \cos \gamma_{i,A}}{r_{i,A}^2} \tag{4.2}$$

where σ_A = area of the detector A at normal incidence.
$\gamma_{i,A}$ = photon incident angle from sample point i to detector A.
$r_{i,A}$ = distance from sample point i to detector A.

The elements of the solid angle calculation are shown in **Figure 4-4.**

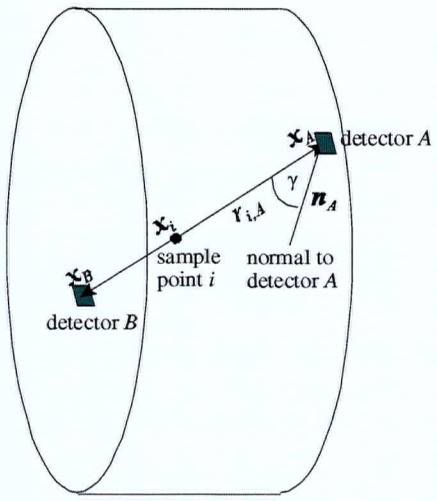

Figure 4-4 The elements of the solid angle calculation from activity sample point *i* to detector *A*.

For computational economy, the solid angle calculation treats the detector crystals as simple area elements rather than volumes. The solid angle is not calculated at the front face of the crystal, but at a depth equal to the mean depth of photon interactions in the crystal (e.g. 4.5 mm for 1.0 cm thick LSO). The distance from the activity sample point to the detector, $r_{i,A}$ is then found by:

$$r_{i,A}^2 = \left(\vec{x}_i - \vec{x}_A\right)^2 \qquad (4.3)$$

where $\vec{x}_i$ = coordinates of the activity sample point i

$\vec{x}_A$ = coordinates of detector A.

The vector from i to A is $\vec{r}_{i,A} = \vec{x}_i - \vec{x}_A = (x_i - x_A, y_i - y_A, z_i - z_A)$. The vectors describing the normals to the detectors are simply the detector positions in the x-y plane and zero in the axial direction, i.e. $\vec{n}_A = (x_A, y_A, 0)$. The incident angle, $\gamma_{i,A}$, is the angle between $\vec{r}_{i,A}$ and $\vec{n}_A$, and is found from:

$$\cos\gamma_{i,A} = \frac{\vec{r}_{i,A} \cdot \vec{n}_A}{|r_{i,A}||n_A|} = \frac{\vec{r}_{i,A} \cdot \vec{n}_A}{|r_{i,A}| r_{ring}} \tag{4.4}$$

where r_{ring} is the radius of the detector ring.

The incident angle is used in both calculating the solid angle and in determining the effective thickness of the detectors **(4.11)**.

4.3.3 Solid Angle of the Partner Photon

When calculating the probability of a coincidence, the probability of detecting the annihilation partner photon must be calculated. However, it is not necessary to determine which crystal the partner photon hits because of its collinearity with the primary photon; thus, the detector solid angle is not calculated explicitly. It is only necessary to determine if the partner photon is incident on the tomograph detector ring. This is found by calculating the axial position of the partner, z_p, on the path $r_{i,B}$ when its radial position is r_{ring}, i.e. at $x_p^2 + y_p^2 = r_{ring}^2$. Partner photons which miss the tomograph are not detected and, therefore, cannot result in a coincidence, only a singles event. Thus, $P_{det,i,B}$ is calculated as:

$$\begin{aligned} P_{det,i,B} &= P_{surv,i,B}\varepsilon_{i,B} \quad for\ |z_p| \le z_{tomo} \\ P_{det,i,B} &= 0 \qquad\qquad\ for\ |z_p| > z_{tomo} \end{aligned} \tag{4.5}$$

where i,B = path of the annihilation partner photon.
$\varepsilon_{i,B}$ = detector efficiency for annihilation partner photon = $\varepsilon_{i,A}$.
z_p = axial position for along $r_{i,B}$ when $x_p^2 + y_p^2 = R_{ring}^2$.
z_{tomo} = axial extent of the tomograph ring.

4.3.4 True Coincidence LOR Calculation and Corrections

The probability of a true coincidence in 3D acquisition is found for the line of response (LOR) defined by $\vec{r}_{i,A}$ using the coordinates x, θ, z_A and z_B. Perfect collinearity is assumed for all events. The relationship between the sinogram axes and the tomograph geometry are shown by **Figure**

4-5. The radial bins of the sinograms are the parallel LORs for a given azimuthal angle. The transverse image planes are the slices in the axial direction.

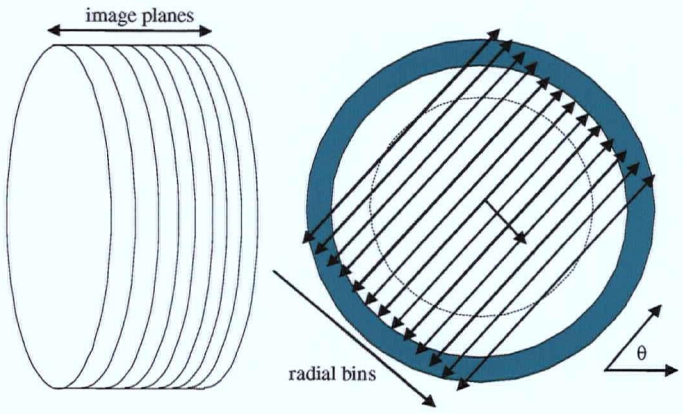

Figure 4-5 The axes of the sinograms are related to the tomograph parameters for transverse slices.

Before binning, the calculated trues distributions are corrected for the changing sampling distances in the radial direction. This "arc effect" reduces radial bin sizes as the displacement from the tomograph axis increases and, therefore, influences the relative counts per bin. An arc correction is usually applied to sinograms prior to reconstruction to prevent image distortion and artifacts from the non-uniform sampling. Arc effects do not occur for single photon detection and, thus, do not influence the randoms sinograms.

4.4 Photon Survival Calculation

4.4.1 Photon Attenuation

The probability of a photon emitted at sample point i being detected at detector A is reduced by attenuation in the object along $\vec{r}_{i,A}$. The intensity reduction is object and photon path dependent; thus, the calculation requires sampling the reconstructed attenuation image.

The probability of photon survival is given by the line integral:

$$P_{surv,i,A} = e^{-\int_{x_i}^{x_A} \mu(x,y,z)ds} \tag{4.6}$$

where $\mu(x,y,z)$ = position dependent attenuation coefficient.
$\vec{x}_i$ = coordinates of activity sample point i.
$\vec{x}_A$ = coordinates of detector A.
ds = interval along $\vec{r}_{i,A}$.

In the photon survival calculation, the 3D attenuation image is sampled at discrete points, $\vec{s}_j$, at intervals of ds along $\vec{r}_{i,A}$. The points are generated using the line parameters of $\vec{r}_{i,A}$ from $\vec{x}_i$ to the edge of the electronic FOV:

$$\vec{s}_{j+1} = \vec{s}_j + ds \times \frac{\vec{r}_{i,A}}{|r_{i,A}|} = \vec{s}_j + ds \times (\cos\theta\sin\phi, \cos\theta\sin\phi, \cos\theta\sin\phi) \tag{4.7}$$

where $\vec{s}_j$ = attenuation sampling points.
ds = sampling interval distance.
θ = azimuthal angle of $\vec{r}_{i,A}$.
φ = oblique angle of $\vec{r}_{i,A}$.

The attenuation coefficient for each sample point, μ_j, is found by indexing the voxel in the attenuation coefficient image corresponding to the coordinates of the attenuation sampling point, $\vec{s}_j$, and looking up the attenuation coefficient value for that voxel; $\mu_j = \mu(\vec{s}_j)$. The photon survival probability for each interval ds is $P_j = e^{-\mu_j ds}$. Then, the total survival probability along $\vec{r}_{i,A}$ is:

$$P_{surv} = \prod_j P_j = \prod_j e^{-\mu_j ds} \qquad (4.8)$$

where j = attenuation sampling point.
P_j = photon survival at j.
μ_j = attenuation coefficient at j.

The probability of a coincidence depends on the survival of both annihilation photons. To calculate the survival of the partner photon, the attenuation object is sampled in the opposite direction (i.e. $-\vec{r}_{i,A}$). The total survival is calculated by **(4.8)**, with an opposite, but collinear, set of attenuation sample points. **Figure 4-6** shows the attenuation object sample points for the both photons along $\vec{r}_{i,A}$ and $-\vec{r}_{i,A}$, respectively.

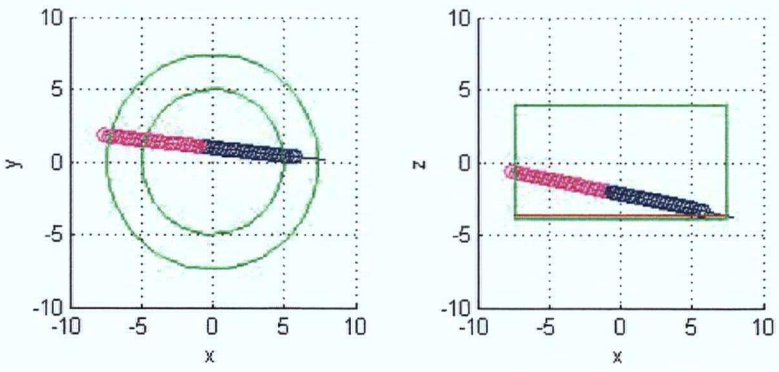

Figure 4-6 Attenuation sample points for along the path from an activity sample point to a detector. Both the primary (blue) and partner (pink) sample points are shown. The green lines show the FOV of the tomographs.

The photon survival probability from an activity sample point is calculated for every detector in the tomograph. This requires a large amount of sampling of the attenuation object, and is the majority of computational burden in the randoms calculation.

The photon survival calculation assumes narrow-beam attenuation: that all the photons interacting on the path $\vec{r}_{i,A}$ are completely lost. However, 511 keV photons interact in tissue almost exclusively by Compton scatter; thus, the narrow-beam calculation underestimates the total photon survival because a fraction of the scattered photons are still counted. **Section 4.6** describes the modifications to the photon survival calculations necessary to account for photon scatter in the object.

4.5 Detector Efficiency Calculations

4.5.1 Detector Efficiency

The last component of the singles photon detection probability calculation is the efficiency of the tomograph detectors. The total detection efficiency, ε_{det}, is the product of the detector intrinsic efficiency, ε_{int} and the fraction of the events with deposited energies within the acquisition energy window, f_{win}:

$$\varepsilon_{det} = \varepsilon_{int} f_{win} \tag{4.9}$$

The detector intrinsic efficiency is defined as:

$$\varepsilon_{int} = 1 - e^{-\mu_{det} x_{det,eff}} \tag{4.10}$$

where μ_{det} = attenuation coefficient of the detector material.
$x_{det,eff}$ = effective detector thickness.

For normally incident photons $x_{det,eff}$ is simply the detector thickness. However, the effective detector thickness increases with the incident angle, γ:

$$x'_{det} = x_{det} / \cos \gamma_{i,A} \tag{4.11}$$

where x_{det} = detector thickness.
$\gamma_{i,A}$ = photon incident angle.

The effective pathlength of photons in the intrinsic efficiency calculation is also affected by the saw-cuts in cut-block detectors. The saw-cuts not only decrease the packing fraction, they reduce the total thickness of scintillator encountered by the photons passing through the detector by the ratio:

$$f_{pack} = \frac{crystal\ size}{crystal\ spacing} \tag{4.12}$$

Therefore, the effective detector thickness used in the efficiency calculation is:

$$x_{det,eff} = f_{pack} x'_{det} \tag{4.13}$$

4.5.2 Energy Window Fraction

The energy window fraction, f_{win}, is the fraction of the photons interacting in the scintillator crystal that deposit energies greater than the lower energy threshold. Photons that deposit energies less than the lower threshold are not counted, resulting in reduced detection efficiency. The value of the threshold is user controlled (typically 250 keV or 350 keV), and the optimal values depend largely on the energy resolution of the detectors.

511 keV photons that interact in the detectors by photoelectric absorption deposit their full energy and are counted in the energy window. However, even in scintillators with high density and high atomic number, the probability of photoelectric absorption of 511 keV photons by a single interaction is small (e.g. 32.5% in LSO). Most of the photons Compton scatter in the scintillator. Those that undergo Compton scatter, but are then absorbed in the detector ("Compton-absorption"), deposit their full energy. However, 511 keV photons that Compton scatter once in the crystal, without a secondary interaction, deposit only a fraction of their total energy; between 0 and 340 keV for 511 keV photons. Neglecting the effects of detector energy blurring, all these events would be rejected by a 350 keV threshold window and a large fraction would be rejected by

a 250 keV window. The contribution of Compton-absorption is not calculated for a each photon path and detector, but it should increase with longer effective detector thickness $x_{det,eff}$

Therefore, since f_{win} is dependent of the effective detector thickness, the detector efficiency calculation might be improved by not assuming that ε_{int} and f_{win} are separable, as was done in **(4.9)** and **(4.10)**. The effect of the energy window on detector efficiency is then incorporated by modifying the exponent in the intrinsic efficiency equation:

$$\varepsilon_{det} = 1 - e^{-\kappa_{det}\mu_{det}x_{det,eff}} \qquad (4.14)$$

where κ_{det} = detection efficiency correction factor to account for the effect of energy thresholds.

The value of κ_{det} may be estimated for a given tomograph detector design (**Section 5.4.3**), but empirical adjustment may be necessary to reproduce measured data (**Section 6.3.2**). As well, since κ_{det} is dependent on the energy threshold, different values of κ_{det} are required for different energy window settings.

The values of f_{win} and κ_{det} would also are be largely dependent on photon scatter in the object, which reduces the photon energies. However, in this calculation, the detection of the object-scattered photons is calculated separately from the un-scattered photons, as described in **Section 4.6**.

4.5.3 Relative Crystal Efficiencies

The efficiencies of individual crystals vary systematically depending on their position in the detector block. For example, photons that scatter in the crystals near the block edge have a lower probability of being absorbed in the same block than photons scattered in the centre crystals. Therefore, the edge crystals have a systematic reduction in efficiency. True coincidences are corrected for these efficiency variations on a LOR basis using the normalization scan data (**Section 2.4.4**). However, the efficiency variations produce a "crystal block structure" pattern on

the singles distributions. This creates a diagonal pattern on the randoms sinogram due to the reduced efficiencies of the edges crystal, as shown in **Figure 4-7**.

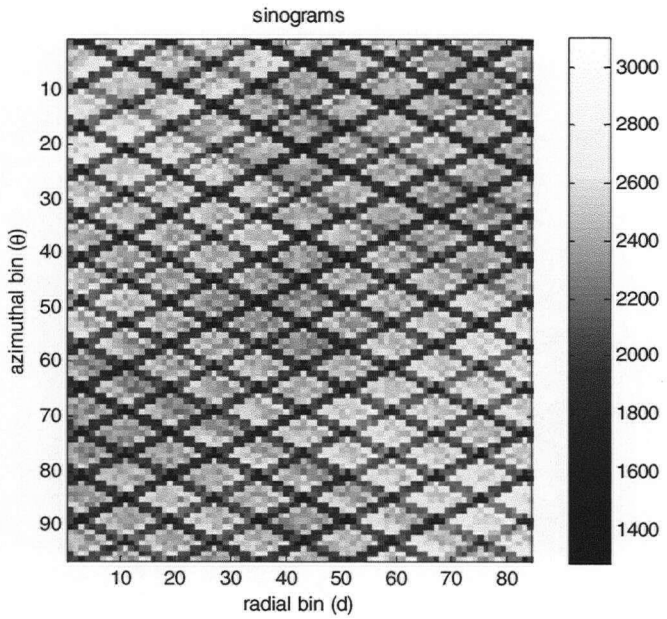

Figure 4-7 The diagonal pattern seen in a measured randoms sinogram. This pattern is caused by the "block structure," the systematic efficiency variations within a detector block.

The systematic, block-structure dependent, singles efficiency variations are incorporated in the calculation of the singles distribution. The singles efficiencies are modeled assuming that the efficiencies of the crystals at the same relative position within the block are identical. The relative block singles efficiencies are determined using Monte Carlo simulations with adjustments made to improve the agreement of the high frequency details between measured and calculated randoms distributions (**Section 5.4.5**). This block structure is then superimposed on the calculated singles distribution before the randoms distributions are calculated. One model of the block structure is used to correct all the detector blocks.

There are also random variations in the individual crystal singles efficiencies. These arise from the PMT tuning, scintillator and PMT non-uniformities and other subtle effects. Random efficiency variations are not incorporated into the singles calculation because they are not directly measured. While singles detector efficiencies are extracted in some normalization schemes [53][54], they are measured using true coincidences. Thus, they reflect the singles efficiencies for a smaller range of incident angles than the single photons involved in the random coincidences, and are not appropriate for correcting the calculated singles distribution [76].

4.6 The Effects of Photon Scatter in the Object

4.6.1 Broad-beam Correction

The photon survival calculation **(4.8)** is only accurate in a narrow-beam situation where attenuation is equivalent to count losses. It assumes that all photons interacting on the path $\vec{r}_{i,A}$ are not detected. However, since nearly all the interactions of 511 keV photons are by Compton scatter, very few photons are absorbed in the object. In a PET scanner, count losses only occur if the scattered photons physically miss the tomograph or if the scattered photons are rejected by the energy thresholds. Thus, **(4.8)** overestimates the count losses because a fraction of the scattered photons are counted.

To account for the lower count losses, the narrow-beam attenuation coefficients from the μ-map used in **(4.8)** are modified by a broad-beam correction factor, ($\kappa_{broad} < 1$); thus, the photon survival calculation becomes:

$$P_{surv} = \prod_j e^{-\kappa_{broad}\mu_j ds} \qquad (4.15)$$

This correction increases the calculated photon survival and, therefore, increases the effective singles counts at each detector. This is similar to the build-up factor used for corrections involving

broad-beam geometries [84] and is in agreement with the lowered attenuation coefficients seen in 3D PET [85].

κ_{broad} is a correction to the photon survival calculation along each path and is derived from the probability of the scattered photons being detected. It is assumed that the reduction in the counts in a detector caused by photons scattering out of the original path is roughly balanced by those that scatter into the detector from other paths (**Section 4.6.3**). Since every photon path from the activity sample point to each detector is sampled, the net effect of this modification is to correct for the broad-beam nature of the photon detection.

This broad-beam correction is based on the probability of the photons that single-scatter in the object being counted somewhere in the tomograph. This depends on the energy distribution of single-scattered photons, the energy-dependent efficiency of the detectors and the value of the energy threshold. Thus, the value of κ_{broad} for a given photon path may be estimated from a calculation of the fraction of the object-scattered photons that are counted in the tomograph (**Section 4.6.2**). Since κ_{broad} for a given path depends on the tomograph design and acquisition parameters, it becomes part of the model for a specific tomograph and acquisition protocol (**Section 5.4.4**). Finally, in this approach, the value is adjusted based on empirical studies (**Section 6.3.3**) and the dependence of the accuracy of the calculation on the value of κ_{broad} is investigated.

In general, build-up factors vary with the product of the narrow beam attenuation values and the thickness, μx. They also vary with the photon energy and attenuating material. In the present calculation, κ_{broad} is a single correction value for the average broad-beam build-up that is used for all paths as a first approximation. In practise, scaling the calculated singles distribution to the measured global singles rates makes the calculation less sensitive to the value of κ_{broad} for different sized objects As well, the final singles counts in each detector are calculated using contributions from many activity sample points with many different paths; thus, errors associated with using an average value of κ_{broad} for all paths tend to cancel out. In situations where this approximation could potentially lead to inaccurate results (for example, when applied to larger objects such as whole

body human studies) a path dependent value of κ_{broad} could easily be implemented in the calculation (**Section 7.2.4**).

Although the broad-beam correction accounts for the reduced count losses due to scatter, it does not address the issue of displaced counts. The photons scattered from a path $\vec{r}_{i,A}$ would not be counted in detector A, but in a different detector, potentially affecting the singles distribution. The effects of the angular distribution of scattered photons are discussed in **Section 4.6.3**.

4.6.2 Estimate of Fraction of the Object-Scattered Photons that are Counted

The fraction of the object-scattered single photons that are absorbed in the detector and counted, $f_{scat,abs}$, depends on a number of factors [86], including the:

- energy distribution of the scattered photons, $f_{KN}(E_{sc})$,
- energy dependence of the detector intrinsic efficiency, $\varepsilon_{int}(E_{sc})$,
- energy dependence of the photon absorption probability in the detector, $f_{abs}(E_{sc})$,
- energy blurring caused by the detector, $f_G(E_{sc})$, and
- energy windows setting used during acquisition,. $f_{win}(E_{sc})$.

Each of these factors are examined in turn and built into the estimate.

The energy distribution of single scattered photons, $f_{KN}(E_{sc})$, is given by the Klein-Nishina equation cast in terms of the energies of the scattered photons, E_{sc}:

$$f_{KN} = \frac{d\sigma}{dE_{sc}} \propto \frac{1}{E_o^{\,2}}\left[\frac{E_o}{E_{sc}} + \frac{E_{sc}}{E_o} + \left(\frac{m_e c^2}{E_{sc}} - \frac{m_e c^2}{E_o}\right)^2 - 2m_e c^2\left(\frac{1}{E_{sc}} - \frac{1}{E_o}\right)\right] \quad (4.16)$$

where m_e = electron rest mass energy.
E_o = unscattered photon energy.
E_{sc} = scattered photon energy.

This distribution is shown in **Figure 4-8** for energies from the backscatter peak (170 keV) to the full energy (511 keV) for annihilation photons.

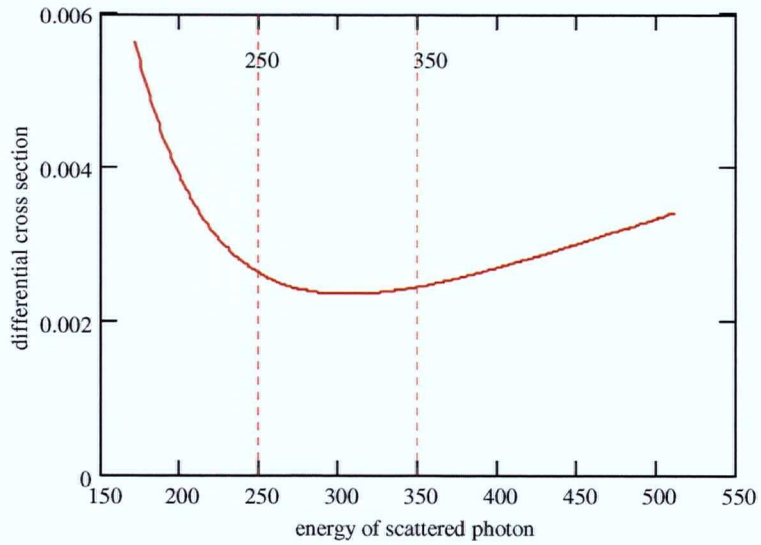

Figure 4-8 The differential cross section vs. scattered energy for object-scattered 511 keV photons; from the backscatter energy (170 keV) to full energy (511 keV). The vertical red lines show two common lower level thresholds use in PET.

The efficiency of detecting these photons depends on E_{sc} because the attenuation coefficient of the scintillator is energy dependent. As well, since the scattered photons have a range of incident angles, the effective detector thickness for individual photon paths, $x_{det,eff}$, in **(4.10)** must be replaced by an average effective value $\langle x_{det} \rangle$. The intrinsic efficiency is then a function of the scattered photon energy, E_{sc}.

$$\varepsilon_{int}(E_{sc}) = 1 - e^{-\mu_{det}(E_{sc})\langle x_{det} \rangle} \qquad (4.17)$$

The product of **(4.16)** and **(4.17)** gives the energy distribution of the object-scattered photons that interact in the crystal.

This absorption fraction, $f_{abs}(E_{sc})$, is the fraction of the interacting photons that deposit all of their energy in the detector, which depends on the photofraction of the detector. Although, in general, this is not a simple function of E_{sc}, in the first approximation $f_{abs}(E_{sc})$ is simply the probability of photoelectric absorption. Thus, the total energy distribution of scattered photons that are *fully absorbed* in the detector is:

$$f_{KN}(E_{sc})\varepsilon_{int}(E_{sc})f_{abs}(E_{sc}) \tag{4.18}$$

However, this distribution is blurred by the energy resolution of the detector. This may be modeled by convolving **(4.18)** with a Gaussian function, $f_G(E)$ that models the shape of the photopeak:

$$f_G(E,E_o)=\frac{e^{\frac{-(E-E_o)^2}{2\sigma(E_o)^2}}}{\sqrt{2\pi}\sigma(E_o)} \tag{4.19}$$

where E_o = reference energy
$\sigma(E_o) = FWHM(E_o)/2.35$ and $FWHM$ is the width of the photopeak.

This function is made more accurate by using an energy dependent width, given that $FWHM \propto 1/\sqrt{E}$. In general, energy blurring in the detector flattens the distribution and may changes the fraction of accepted photons depending on the energy threshold.

In summary, the total energy distribution of the object-scattered photons that are fully absorbed in the detector, $P_{scat,abs}(E_{sc})$, is:

$$P_{scat,abs}(E_{sc})=\left[f_{KN}(E_{sc})\varepsilon_{int}(E_{sc})f_{abs}(E_{sc})\right]\otimes f_G(E_{sc},E_{sc,o}) \tag{4.20}$$

Finally, the fraction of the photons that are absorbed in the detector and counted in an energy window, $f_{scat,abs}$, may then be estimated by integrating **(4.20)** over the bounds of the energy window and normalizing to the total integrated scattering cross section:

$$f_{scat,abs} = \frac{\int_{E_{lower}}^{E_{upper}} P_{scat,abs}(E_{sc})dE_{sc}}{\int_{E_{sc}=170keV}^{E_{sc}=511keV} f_{KN}(E_{sc})dE_{sc}} \tag{4.21}$$

where E_{upper} (E_{lower}) = upper (lower) energy threshold.

The impact of the detected object-scattered photons may be seen by simplifying the photon survival calculation to a uniform attenuation situation:

$$P_{surv} \approx e^{-\mu_{obj}x_{obj}} \tag{4.22}$$

where μ_{obj} = attenuation coefficient of the object material.
x_{obj} = pathlength through the object.

Neglecting the object-scattered photons, the total photon detection probability **(4.1)** is:

$$P_{det} \propto P_{surv}\varepsilon_{det} = e^{-\mu_{obj}x_{obj}}(1-e^{-\kappa_{det}\mu_{det}x_{det,eff}}) \tag{4.23}$$

Adding the effects of the detected scattered photons (4.23) becomes:

$$P_{surv}\varepsilon_{det} = e^{-\mu_{obj}x_{obj}}(1-e^{-\kappa_{det}\mu_{det}x_{det,eff}}) + (1-e^{-\mu_{obj}x_{obj}})f_{scat} \tag{4.24}$$

If the broad-beam correction factor is used to account for the scatter, then **(4.24)** becomes:

$$P_{surv}\varepsilon_{det} = e^{-\kappa_{broad}\mu_{obj}x_{obj}}(1-e^{-\kappa_{det}\mu_{det}x_{det,eff}}) \tag{4.25}$$

The value of κ_{broad} is then estimated by equating (4.24) and (4.25), and solving for κ_{broad} for a given value of $\mu_{obj} x_{obj}$. This calculation has been done for the MicroPET R4 **(Section 5.4.4)**.

However, this calculation provides a lower limit estimate because it only accounts for the singly scattering photons that are fully absorbed in the detector by a single interaction. It does not include other relevant processes, such as multiple Compton scatter or Compton-absorption in the detector, that increase the number of counted photons. Therefore, the estimated value of κ_{broad} is further adjusted to fit the empirical data. The dependence of the randoms calculation accuracy on the value of κ_{broad} was also investigated experimentally (**Section 6.3.3**).

A single value of κ_{broad} was used in the randoms calculation and is expected to give good results for small objects (such as those tested in this work). In principle, the optimal value of κ_{broad} changes with object size. However, scaling the calculated singles to the measured singles rates reduces the dependence of the results on the exact value of κ_{broad}. The above derivation may also be used to determine the path-dependent values of κ_{broad}, which may lead to improvements if the randoms correction is applied to larger objects (**Section 7.2.4**).

4.6.3 The Spatial Distribution of the Object-Scattered Photons

In the previous section, the fraction of the object-scattered photons that are detected was described and a broad-beam correction was applied to the photon survival calculation. However, the spatial distribution of the detected scattered photons was not discussed. Since the scattering process alters the paths of the photons, the distribution of detected single photons could be affected. Following the paths of every scattered photon in a given study would require a detailed Monte-Carlo simulation. In the model-based calculation, the effects of the photon displacement may be determined based on some general observations [87].

The photons scattered from the beam along $\vec{r}_{i,A}$ are effectively distributed in a cone around $\vec{r}_{i,A}$ originating at the scattering location, $\boldsymbol{x}_{sc}$, as shown in **Figure 4-9**. Thus, the overall effect of

scatter is that photons scattered along $\vec{r}_{i,A}$ are counted by detectors in an area centred on detector A.

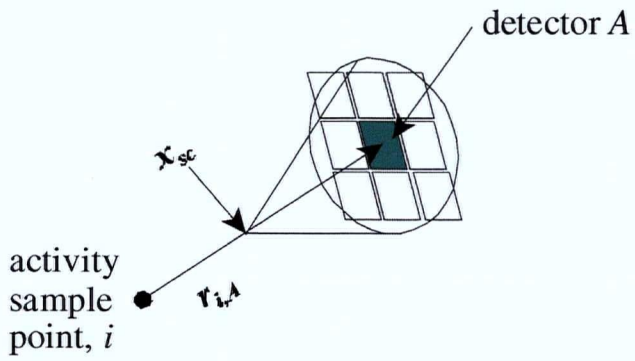

Figure 4-9 Scattered photons are scattered into a cone around the ray between the emission point and the detector. Some of the scattered photons hit other detectors.

The energy thresholds not only cause count losses due the rejection of object-scattered photons, they also effectively determine the maximum and average scattering angles of photons that are counted. The relationship between scattering angle, θ_{sc}, and scattered photon energy E_{sc} is given by:

$$\theta_{sc} = \arccos\left(1 - \frac{511}{E_{sc}} + \frac{511}{E_o}\right) \qquad (4.26)$$

where E_o = original photon energy.
E_{sc} = scattered photon energy.

From **(4.26)** an energy threshold of 250 keV corresponds to a maximum scattering angle, $\theta_{sc,max}$ = 93° and a threshold of 350 keV corresponds to $\theta_{sc,max}$ = 58°, ignoring energy blurring. Thus, the scattering cones of the energy-accepted photons have these half-angles.

The angular distribution of Compton scattered photons is given by the common form of the Klein-Nishina equation:

$$\frac{d\sigma}{d\Omega} = \frac{r_e^2}{2} \frac{1+\cos^2\theta_{sc}}{[1+\alpha(1-\cos\theta_{sc})]^2} \left[1 + \frac{\alpha^2(1-\cos\theta_{sc})^2}{(1+\cos^2\theta_{sc})[1+\alpha(1-\cos\theta_{sc})]} \right] \quad (4.27)$$

where r_e = the classical electron radius.
$a = E/ m_e c^2$ (ratio of photon energy to electron rest mass energy.)
θ_{sc} = scattering angle.
$d\Omega = 2\pi \sin\theta_{sc} d\theta_{sc}$.

Figure 4-10 shows the normalized differential and integral scattering cross sections for 511 keV photons. The cross-section is strongly biased to small scattering angles; thus, the photons have a higher probability of being detected closer to detector *A*. Therefore, although the maximum scattering angles are 58° and 93°, respectively for thresholds of 350 keV and 250 keV, the average scattering angles are lower. In the case of a 350 keV energy threshold, 50% of these detected photons were scattered into a cone with a half angle of 34° (45° for 250 keV.) However, in absolute terms, the number of scattered photons that hit an individual detector is smaller at larger scattering angles, because the distribution is spread over a larger area, reducing the beam density.

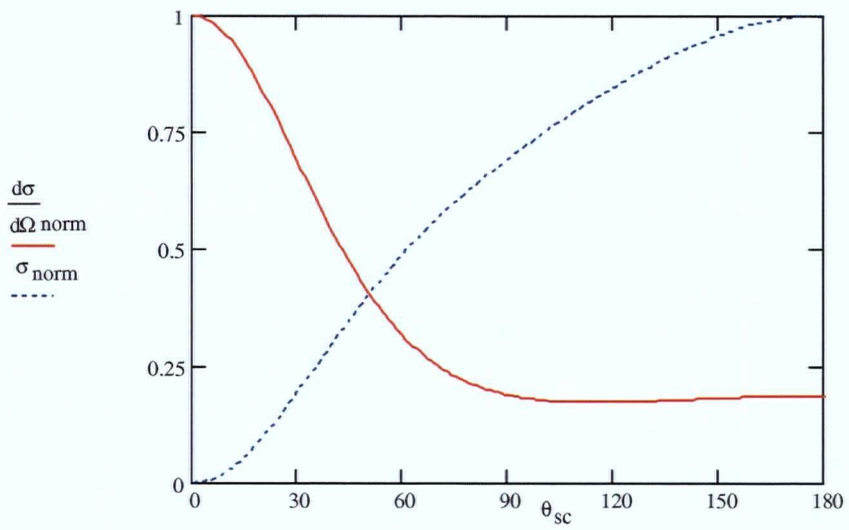

Figure 4-10 The normalized differential (solid) and integral (dashed) cross sections for the Compton scattering of 511 keV photons at angles from 0 to 180°.

While it may be possible to calculate the distribution of scattered photons, including the necessary additional corrections for the differences in solid angle, survival and detection efficiency for the scattered photons excessively increases the complexity and computational burden of the calculation. However, this calculation is not necessary because the effects of scatter on the singles distribution generally cancel. Any photons that scatter out of the beam along the path $\vec{r}_{i,A}$, and therefore do not hit detector A, hit one of the surrounding detectors. Likewise, some of the photons that scatter from neighbouring beams hit detector A, as shown in **Figure 4-11**. The total photons incident on the tomograph detectors is largely preserved. Therefore, no further modification to the singles distribution is used beyond the broad-beam correction.

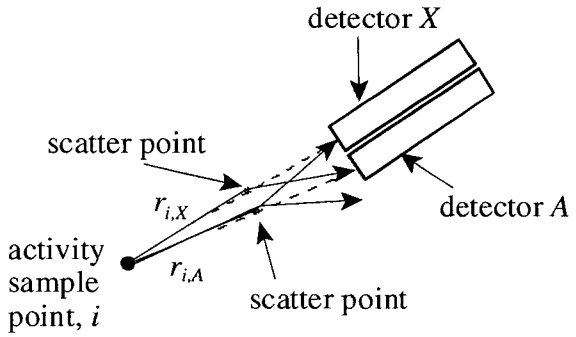

Figure 4-11 Some of the photons scattered along $\vec{r}_{i,A}$ hit detector X and some scattered along $\vec{r}_{i,X}$ hit detector A. This calculation assumes that the losses and gains of counts due to scatter in neighbour photon beams are roughly balanced.

4.7 Calculating, Scaling and Subtracting the Randoms Distributions

4.7.1 Calculating Relative Count Contributions

Once the photon detection probabilities per detector **(4.1)** are calculated for an activity sample point, the singles and trues count rates contributions are simply the product of the detection probability and the activity of the sample point. Therefore, the contribution of the radioactivity at i to the singles rate at detector A is:

$$R_{s,i,A} = P_{det,i,A}\Lambda_i \qquad (4.28)$$

where $P_{det,i,A}$ = probability of single event on detector A due to radioactivity at i **(4.1).**
Λ_i = radioactivity at sample point i.

The total singles rate at detector A, $R_{s,A}$, due to all the activity sample points is then:

$$R_{s,A} = \sum_{i=1}^{n} 2R_{s,i,A} \qquad (4.29)$$

where n = number of activity sample points.
2 = the emission of two photons per annihilation.

Likewise, the calculated contribution to the trues rates along the LOR defined by the line $\vec{r}_{i,A}$ is:

$$R_{t,i,LOR(iA)} = P_{det,i,A}P_{det,i,B}\Lambda_i \qquad (4.30)$$

where $LOR(iA)$ = the LOR defined by the line $\vec{r}_{i,A}$.

The total trues rate for $LOR(iA)$ is the sum of the contributions from all the sample points.

4.7.2 Scaling the Rates

The calculated singles and trues rate distributions described thus far are only relative values. Therefore, the calculated detector singles rates require scaling to absolute values before the randoms distributions are calculated. The simplest and most robust scaling method is to simply scale the total calculated singles to the global, average singles rate measured by the tomograph. In this case, the scaling factor for singles and trues is:

$$f_s = \frac{R_{s,meas}}{R_{s,calc}} \qquad (4.31)$$

where $R_{s,meas}$ = measured average global singles rate.
$R_{s,calc}$ = sum of the calculated singles rates of all detectors = $\sum_{A=1}^{N_{det}} R_{s,A}$.

This one scaling factor is applied to all the calculated singles rates in each detector to give the scaled singles rates $R'_{s,A}$:

$$R'_{s,A} = f_s R_{s,A} \tag{4.32}$$

This method of scaling requires that the measured global singles rate be corrected for detector dead-time. There are potential problems if dead-time associated with singles rates and coincidence rates differ due to differences in their processing. Errors in the singles rate dead-time correction lead to scaling inaccuracies, especially at higher count rates, and impose a limit on the maximum count rate for which the randoms correction would be effective. However, for both singles and coincidences, the scintillator decay time dominates. Therefore, the dead-time correction factor calculated by the tomograph software may be used to correct the singles rates, albeit in a modified form. The effect of high dead-time on the accuracy of the model-based randoms correction is tomograph dependent, and must be determined experimentally.

4.7.3 Correction for LSO Radioactive Background on Singles Calculation

The use of scintillators which cause a radioactive background counts (e.g. LSO) requires **(4.31)** and **(4.32)** to be modified. The singles calculation assumes that all the singles events are due to the radioactivity distribution. However, the measured rates have two components: one due to radioactivity in the subject (which is time dependent) and the other due to the background radioactivity in the scintillator material (which is time independent.) Since the singles distribution calculation assumes that the counts are due only to the activity in the subject, the scaling factor should be:

$$f_{s,bgd} = \frac{R_{s,meas} - R_{s,bgd}}{R_{s,calc}} \tag{4.33}$$

where $R_{s,bgd}$ = measured total singles rate due to background radioactivity.

Then, the singles rates in each detector, A, are scaled by:

$$R'_{s,calc,A} = f_{s,bgd} R_{s,calc,A} + R_{s,bgd,A} \tag{4.34}$$

where $R_{s,calc,A}$ = calculated singles rate in detector A.
$R_{s,bgd,A}$ = measured background singles rate per detector.

Since the trues rate from the background radioactivity is generally negligible in realistic scanning situations, the trues rates are simply scaled by.

$$R'_{t,LOR(iA)} = f_{s,bgd} R_{t,lor(iA)} \tag{4.35}$$

4.7.4 Calculating Randoms from Singles

Once the singles rates distribution is scaled, the average randoms rate, R_r, for each pair of detectors is computed directly from the calculated average detector singles rates using **(3.3)**. The parameters of the line of response are also calculated for each detector pair based on the relative detector positions in the tomograph. The calculated randoms rate is then stored in the randoms sinogram at the calculated LOR coordinates. This is done for all possible detector pairs and binned in a 3D data set with the same data reduction parameters (span and mashing) as the acquired data set.

The calculated randoms sinograms now contain average randoms rates. However, randoms subtraction uses sinograms of the total randoms *counts* for a given acquisition time. Converting average randoms rates to total randoms counts requires a decay correction that takes into account the quadratic dependence of the randoms rates on activity, as well as the acquisition time.

Assuming that the spatial distribution of radioactivity does not change significantly with time during the duration of the frame, the total radioactivity, singles rate and trues rates all decrease exponentially with time due to the decay the radionuclide:

$$R(t) = R_o e^{-\lambda t} \tag{4.36}$$

where λ = decay constant of radionuclide.
R_o = initial trues or singles count rate.

The randoms are related to the square of the singles rates and, therefore, decrease as:

$$R_r(t) = R_{r,o} e^{-2\lambda t} \tag{4.37}$$

where $R_{r,o}$ = initial randoms event rate.

When calculating the average randoms rates from the average singles rates, a decay correction factor, $f_{r,decay}$, is required to correct for the differences in how the randoms and singles rates change with the decay of the radioactivity. This is found by integrating **(4.36)** and **(4.37)** over the acquisition times, yielding the singles and randoms decay factors. Then, $f_{r,decay}$ is the ratio of the randoms decay factor to the square of the singles decay factor:

$$f_{r,decay} = \frac{\lambda T_{acq}}{2} \frac{\left(1 - e^{-2\lambda T_{acq}}\right)}{\left(1 - e^{-\lambda T_{acq}}\right)^2} \tag{4.38}$$

where T_{acq} = scan acquisition duration.

This correction is small for scans with acquisition times that are short compared to the half-life of the radionuclide. For example, for a 30 minute scan with ^{18}F, the correction is 0.3% and for a 60 minute scan it is 1.2%. For a three hour scan the correction is much larger, 10.5% and, for a 12 hours scan, it is 230% [80].

This decay correction must be modified to take into account scintillator background radioactivity. In the presence of such a background, the singles rate does not follow **(4.36)** but changes with time as:

$$R(t) = (R_o - R_b)e^{-\lambda t} + R_b \qquad (4.39)$$

where R_b = background singles count rate.

Therefore, $f_{r,decay}$ is calculated using **(4.39)** rather than **(4.38)** because the part of the randoms due to the background should not be decay corrected.

Finally, the total randoms counts for each detector pair, $C_{r,total}$, is calculated by:

$$C_{r,total} = f_{r,decay} R_r T_{acq} \qquad (4.40)$$

Thus, the randoms calculation produces a scaled and spatially variant randoms distribution. The randoms counts distributions are then subtracted directly from the measured prompts sinograms. The resulting trues sinograms are attenuation corrected, normalized and reconstructed.

Chapter 5

An Algorithm for Model-Based Randoms Correction for the MicroPET R4 Tomograph

5.1 Development of the Randoms Correction Algorithm

5.1.1 Chapter Overview

This chapter details of the specific algorithm and implementation of the randoms correction calculation. The chapter begins with a description of the randoms calculation algorithm. Then, the details of the design and performance of the MicroPET R4™ tomograph, used to test the randoms correction, are described. The chapter ends with a detailed discussion of how the MicroPET R4 is modeled in the single photon detection calculation.

5.1.2 Introduction

A computer program was written to perform the randoms correction using the model-based method described in **Chapter Four**. This method is, in theory, applicable to any PET tomograph provided that the design and performance characteristics of the specific tomograph are accurately specified in the calculations.

Originally, the randoms correction was intended to be used for dual head coincidence imaging (DHCI) systems [14], specifically the Philips/ADAC Vertex Molecular Coincidence Detector with Attenuation Correction™ (MCD/AC). The Vertex MCD/AC is dual head SPECT camera with the NaI(Tl) crystal thickness increased from 3/8" to 5/8", coincidence electronics, axial septa and a singles-based transmission scanning system. However, this camera did not measure delayed coincidences and used only a simple background subtraction to correct for randoms and scatter.

Our research group performed a number of studies aimed at defining and improving the performance of this class of devices [88][89][90]. Work also began on the development of calculated scatter and randoms corrections for the MCD/AC camera [91][92]. However, DHCI systems became obsolete, given their inferior performance compared to dedicated PET, and have been superseded in common usage by the widely available dedicated PET and PET/CT systems.

It was, therefore decided to develop the model-based randoms correction method for use on a Siemens MicroPET® R4. This dedicated PET tomograph is designed to image small animals with

high resolution and high sensitivity in an axial field of view that is large relative to the size of the subjects. The MicroPET was ideal for validating the random correction because it stores prompts and delays separately, so that measured randoms distributions are easily extracted. As well, since small objects are imaged, the effects of single photon scatter are less significant. **Section 5.3** describes the design and performance of the MicroPET R4 in detail, and **Section 5.4** describes the modeling of this tomograph in the singles calculation.

5.1.3 Program Development

The randoms correction program, "*rand_corr*", was required to perform the calculations in a clinically reasonable time (~ minutes) using a single CPU PC with 1 GB of memory. Although developed in a Windows XP environment, it was also desirable that the code be portable to other platforms. As well, the code needed to be flexible enough to allow different tomograph designs to be modeled with only minor changes.

It was, therefore, decided to write the model-based randoms correction program in MATLAB™ (© 1984-2007, The Mathworks™, Inc.). MATLAB is a high level programming language optimized to perform calculations on large arrays of multidimensional data. Although MATLAB is a script language, code optimization allows execution to be very fast, approaching the speed of compiled C code. As well, a MATLAB compiler is available which translates the MATLAB script files into C code for compiling into an executable file. MATLAB is also available for different computer platforms with only minor compatibility issues, so that the code is portable. MATLAB includes powerful editing, debugging and optimization tools. It has tools to analyze data, to build graphical user interfaces (GUIs) and produce presentation quality graphics of two and three dimensional data sets.

MATLAB was used to create *rand_corr*, as well as a number of other programs used in the development, testing and analysis of the randoms correction method. The analysis and visualization tools potentially have wider applications beyond this work and may be useful in other related research. First, a graphical user interface was developed to run the *rand_corr* program. It

simplifies the control of all the calculation parameters. Access to debugging and visualization tools is also simplified. The *rand_corr* gui is shown in **Figure 5-1.**

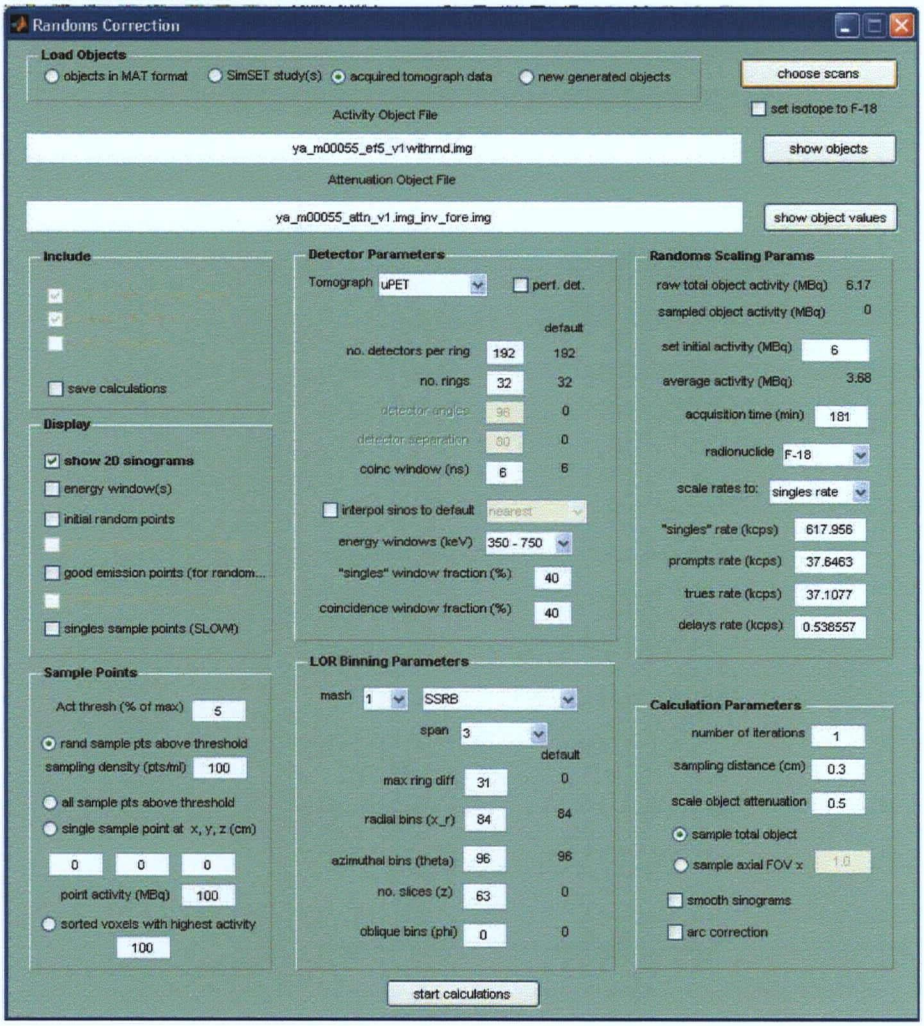

Figure 5-1 Graphical user interface (GUI) for *rand_corr*. This interface allows control of all the calculation parameters and the selection of the data sets used for the randoms correction.

A set of programs for data handling, processing, visualization and analysis in a graphical environment were created under the name *CODEX* (*COincidence Data EXaminer*). These were developed because no other appropriate data analysis package was available. *CODEX* includes

graphic tools to display, analyze and compare 2D data sets (sinograms, projections or singles distributions), as shown in **Figure 5-2**.

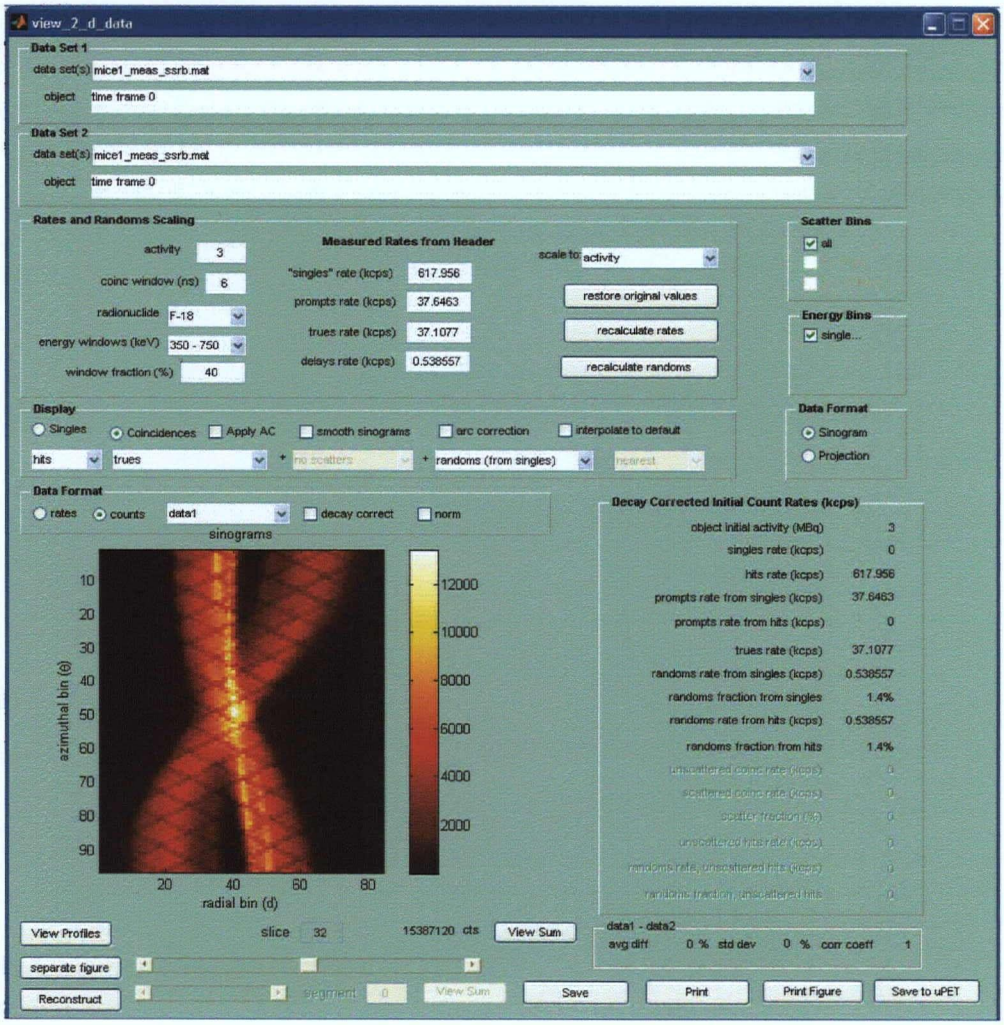

Figure 5-2 The graphical 2D data analysis tool used in *CODEX*. A 2D sinogram is displayed.

As well, a 1-D profile data analysis/display tool was developed to simultaneously display radial, azimuthal and axial profiles of multiple data sets as raw counts or as ratios, percent differences or other figures of merit between the different data sets. This program is shown in **Figure 5-3.**

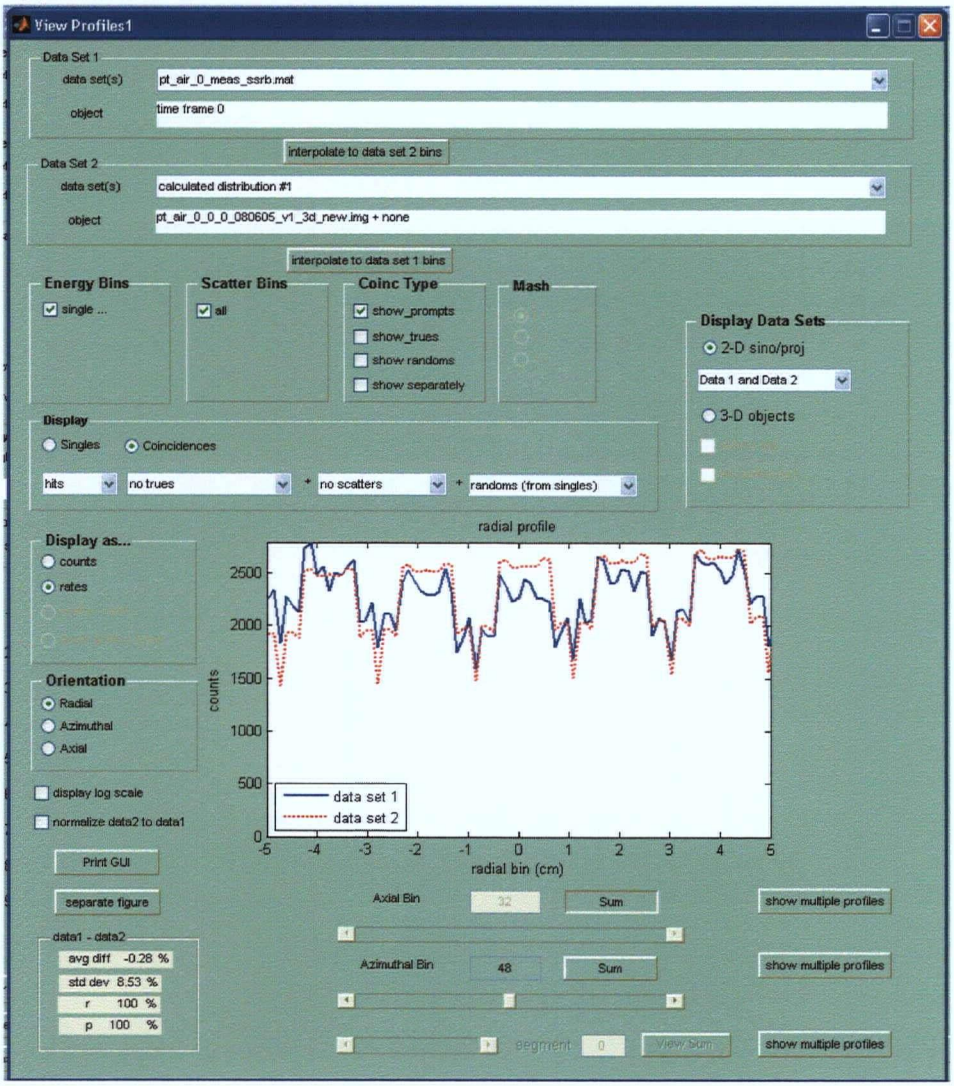

Figure 5-3 The 1-D profile analyze/display tool used in *CODEX*. This is used to analyze and compare the 1-D profiles from different data sets.

5.2 Structure of the Randoms Correction Code

5.2.1 Overview

The basic mathematics of the randoms correction calculation is described in detail in **Chapter 4**. The implementation of the calculation is described in detail in this section. The overall structure of the *rand_corr* code is shown in **Figure 5-4**.

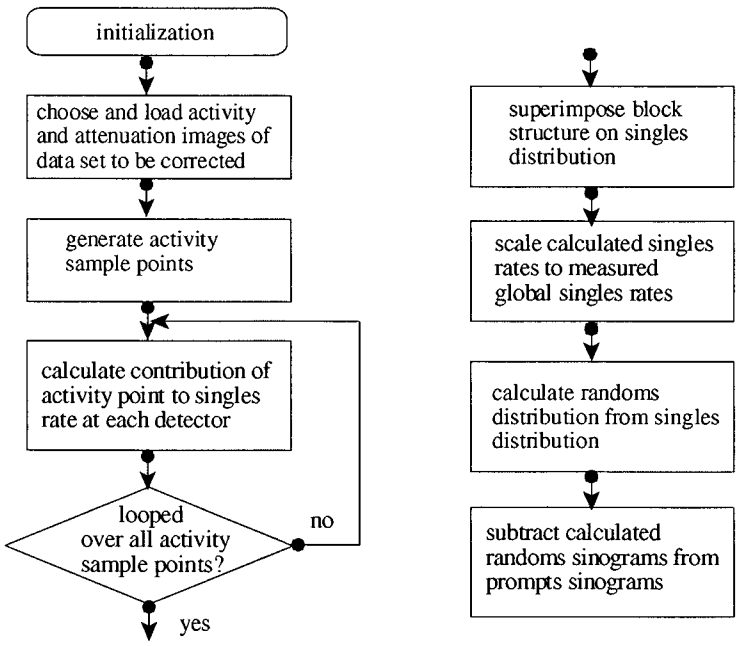

Figure 5-4 The structure of the random correction algorithm.

5.2.2 Initialization of Calculation Parameters and Loading Image Data

The *rand_corr* program uses a number of parameters that govern the randoms calculation, tomograph detector model, and various other aspects of the overall calculation. The "Detector Parameters" describe the tomograph model and include the *number of detectors per ring*, *number of rings*, *coincidence timing window*, *energy window* and the *detection efficiency correction factor*. The "Randoms Scaling Parameters" are used in calculating the absolute randoms counts and include the *acquisition time*,

radionuclide, measured singles rates and *background singles rate.* The "LOR Binning Parameters" determine the binning of the trues and randoms sinograms produced by the calculation. These include the *mash, span, maximum ring difference, number of radial and azimuthal bins, number of slices* and the *2D rebinning* methods. The sinogram binning should match the sinogram binning of the acquired data sets to be corrected. The "Radioactivity Object Sampling Parameters" are used in the generation of the activity sample points, and include the *sampling method, percent threshold,* and *sampling density* or *number of sample points.* The "Display Parameters" set flags to graphically display information used during the calculation for debugging or presentation purposes. The information that may be shown includes the plotting of the *generated activity sample points,* and the *attenuation sample points* used in the photon survival calculations.

When the data set to be randoms corrected is selected, the header files of the preliminary reconstructed images are read and the header information and the image data are loaded into memory using a widely used MATLAB function, *read_asipro.m* [93]. The voxel values may be accessed by a 3D coordinate or a single index. Acquisition and/or tomograph information from the header files that is relevant to the randoms calculation (e.g. study acquisition parameters, calculated correction factors, measured count rates, reconstruction and processing parameters) are used to set the calculation parameters in *rand_corr.* However, the calculation parameters may be changed by the user before the calculation.

5.2.3 Generation of Activity Sample Points

The first step in the calculation is the random generation of the positions of the activity sample points. Three sets of random numbers, bounded by the tomograph FOV, give the x, y and z coordinates. If the activity distribution extends beyond the FOV (for example, a long digital phantom for testing or reconstructed images from multiple bed positions knitted together), the points are generated outside the FOV. The random point positions are stored in three vectors corresponding to the x, y and z coordinates.

The activity at each of these sample points is then determined by finding the value of the voxel in the activity distribution image that corresponds to the position of the point. The activity values are compared to the threshold and the sample points with values below the threshold are removed from the set used in the calculation of the singles rate distribution.

5.2.4 Calculation of the Contribution of Each Activity Sample Point

The contributions of each activity sample point to the detector singles rates **(4.28)** and trues rates **(4.30)** are then calculated while looping over all the sample points. The *rand_corr* code is vectorized to simultaneously calculate the singles and trues contributions for all the detectors in one ring. Therefore, the calculation loops over all detector rings. The flowchart for this routine is shown in **Figure 5-5.** Each element of the flowchart includes a reference to the appropriate equation from **Chapter 4**. As well, in this section, the primary photons are referred to as the "blue" photons, while their annihilation partners are the "pink" photons.

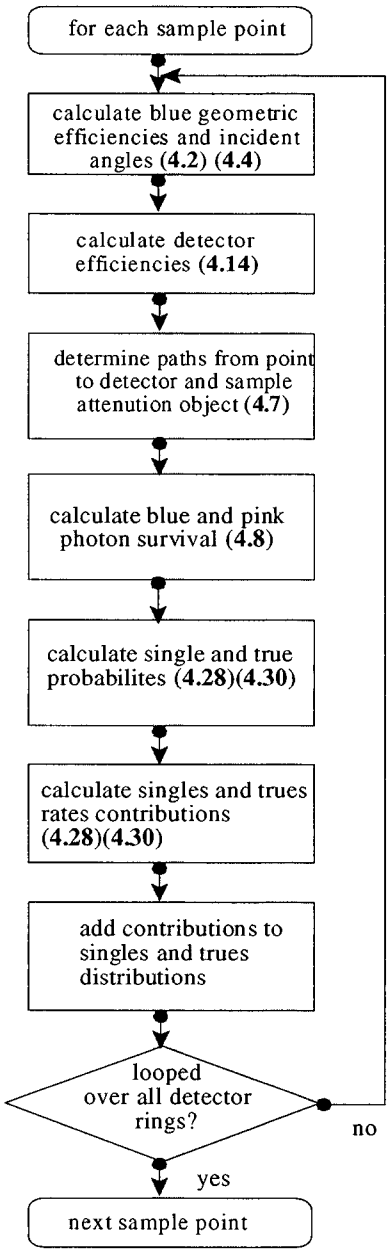

Figure 5-5 The structure of the routine in 'rand_corr' that calculates the contribution of an activity sample point to the singles and trues distributions. In each element is a reference to the corresponding equation. The "blue" photon refers to the primary photon under consideration, while the "pink" photon is the annihilation partner.

The first step is the simultaneous computation of the distance **(4.3)**, incident angle **(4.4)** and the line parameters **(4.7)** from the activity sample point to each detector in the ring. These values are stored as vectors and used for calculating the solid angles **(4.2)** and detector efficiencies **(4.14)** of the blue photons, which are also stored as vectors. Then, the line parameters are used to determine the axial location at which the pink photons intersect the tomograph detector ring in order to calculate the probability of detecting the pink photons **(4.5)**.

The line parameters are used to generate the attenuation sample points **(4.7)** from the activity sample point position through the attenuation object to each detector in the ring, as shown in **Figure 4-6**. This produces a set of two dimensional data structures with one dimension the detector in the ring, and the other the attenuation sample points. Attenuation sample points that extend beyond the bounds of the attenuation object are rejected, and the lines truncated. The attenuation sample point coordinates are then converted to object indices and used to look up the attenuation coefficients along the line and calculate the interval photon survival, $P_j = e^{-\mu_j ds}$. The product of the interval photon survival values along the lines yields the total photon survival to each detector **(4.8)**. Calculating the total photon survivals collapses the 2D data structure into a vector, with each element the total photon survival to a different detector. The pink photon survival is calculated identically.

The solid angle, photon survival and detection efficiency vectors are then used to calculate the contributions of the activity sample point to the singles rate **(4.28)** and trues rate **(4.30)** of each detector in the tomograph ring. The singles rates contributions for this detector ring are then added to the singles distributions. The trues rates contributions are added to the trues sinograms for the LORs that are calculated from the line parameters.

This calculation is done for each detector ring and then repeated for each activity sample point until the contributions from all activity sample points are added. The result is a two dimensional singles distribution (indexed by crystal position and detector ring, (**Figure 5-6**)) and a 3D trues data set.

5.2.5 Adding Block Structure Scaling, and Calculating Randoms

Once the total singles rates distribution has been calculated, the singles rates are multiplied by systematic relative detector efficiencies (**Section 4.5.3**) producing the "block structure" shown in **Figure 5-6**. The calculated trues are not corrected for the relative detector efficiencies because the identities of both crystals involved in a coincidence are not explicitly calculated.

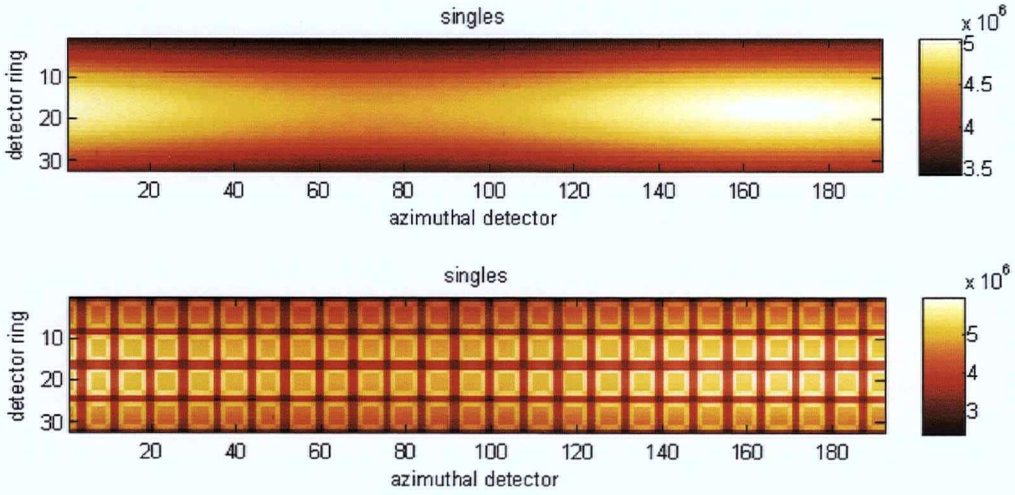

Figure 5-6 The calculated singles distribution to the 32 x 192 arrays of the detectors in the tomograph. The singles distributions before (above) and after (below) correction for relative individual detector efficiencies are shown.

The calculated singles distribution and trues sinograms are then scaled to the measured global average singles rate and corrected for the radioactive background in LSO. Thus, the singles and trues distributions contain absolute values of count rates based on the rates measured during scan **(Section 4.7.2).**

Next, the singles distribution is used to calculate the sets of randoms sinograms. The randoms rate per detector pair is calculated from the singles rates in each detector. The randoms calculation is performed for the one row of radial bins at a time, each corresponding to one azimuthal angle. The singles rates in a half-ring of detectors are stored in one vector and the rates in the opposite

half-ring are stored in another vector. The products of the opposing detector singles rates give the randoms rates for the LORs between the detector pairs. The LORs are then offset by a single detector, and the randoms rates for the new LORs are calculated. These LORs are assumed to be interleaved between the first set of LORs, increasing the radial sampling. This follows the binning scheme used by most modern tomographs. Thus, for a ring of n_{det} detectors, the randoms rates are calculated first for $\frac{n_{det}}{2}$ LORs using the opposing half-rings and then for the $\frac{n_{det}}{2}-1$ interleaved LORs. This yields a total of $(n_{det} - 1)$ LORs per azimuthal angle. The detector ring pairs and the LORs are shown in **Figure 5-7**.

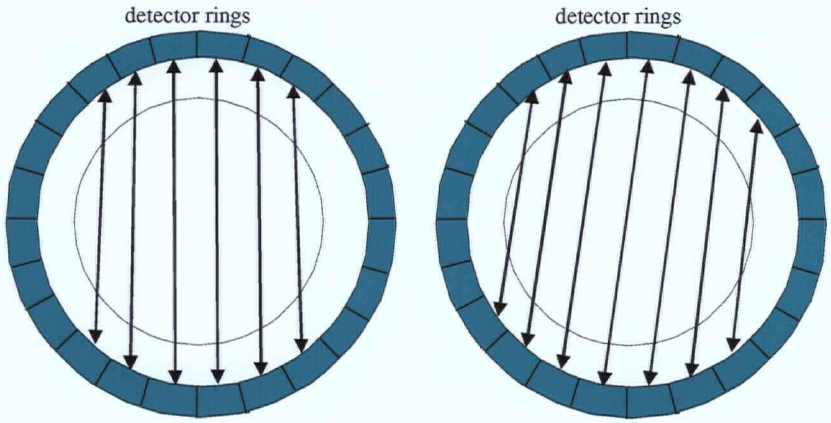

Figure 5-7 The calculation of the randoms for the even numbered LORs (left) and the odd numbered interleaved LORs (right). The dashed line shows the electronic FOV.

All the rows of the randoms sinograms are then calculated in like manner by rotating the azimuthal angle of the LORs and recalculating based on the singles rates of the detector pairs in the new half-rings. In this binning scheme, $\frac{n_{det}}{2}$ azimuthal angles are used. The calculation continues until the random are calculated for the LORs at all possible angles, yielding a $(n_{det} - 1) \times (n_{det}/2)$ randoms sinogram. Randoms sinograms are calculated for single detector rings or pairs of detector rings. Since a 3D data set is required, a randoms sinogram is calculated for each possible pair of

detector rings. This yields a $(n_{det} - 1) \times (n_{det}/2) \times n_{rings} \times n_{rings}$ data set, where n_{rings} is the number of detector rings in the tomograph Once all the randoms sinograms are calculated, the radial dimensions of the trues and randoms sinograms are truncated to match the size of the electronic FOV. The sinograms may then be rebinned and/or reformatted to match the structure of the data to be randoms corrected.

Finally, the values in the randoms sinograms are converted to total randoms counts for an acquisition time frame (**Section 4.7.4**). The calculated randoms counts may then be directly subtracted from the measured prompts sinograms to correct them for randoms.

5.2.6 Optimization of the Code

Two methods of code optimization significantly improve the execution speed in MATLAB. The first is the pre-allocation of memory for large data arrays. The randoms calculation involves the use of large data arrays. For example, the calculated 3D randoms sinograms for the MicroPET R4 are four dimensional and contain 18 million bins (191×96×32×32). Dynamically reallocating memory during the calculation would increase the computation time considerably. Pre-allocating memory to store large arrays before the calculation of the values of the array elements resolves this computational problem. The speed improvement is considerable.

The second important code optimization is performed by vectorizing the calculation code. As its full name, MATrix LABoratory, suggests, MATLAB is optimized to do simultaneous calculations on the elements of data structures such as vectors, matrices and multidimensional arrays. Using array calculations in the place of loops significantly reduces the calculation time. Vectorization is used extensively in the calculation of the singles distribution and in the calculation of the randoms sinograms.

5.3 The MicroPET R4 Scanner

5.3.1 MicroPET R4 Tomograph and Detector Design

The imaging of small animals for research has been advanced by the development of MicroPET tomographs [94]. The MicroPET R4 is a small aperture, large axial FOV dedicated tomograph used for imaging mice and rats, shown in **Figure 5-8**. It has a 120 mm central aperture defined by 25 mm thick lead end-shields. The detector ring is 148 mm in diameter, but the transverse FOV is electronically limited to a 100 mm diameter. The axial field of view is 78 mm. It is based on the original MicroPET design [95] and is similar to the MicroPET P4 small primate scanner [96].

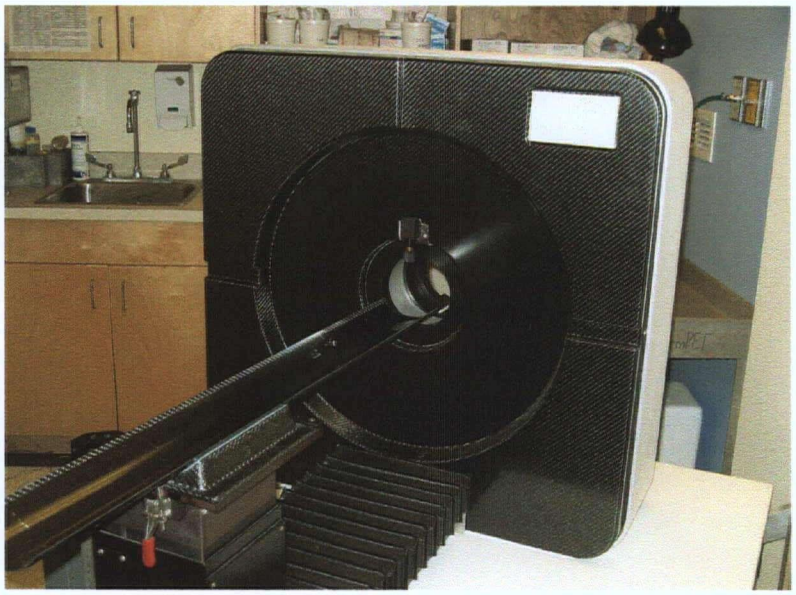

Figure 5-8 The MicroPET R4 small animal tomograph. The aperture is 120 mm and axial FOV is 78 mm, large enough to accommodate two mice or one large rat.

The MicroPET R4 detectors use a LSO(Ce) scintillator crystal block 19x19 mm^2 by 10 mm thick. The block is cut into an 8 x 8 array yielding 64 crystals, each 2.1 x 2.1 x 10 mm^3. Since the centre-to-centre crystal spacing is 2.4 mm, the overall volumetric packing fraction is 76.5%. The cuts are all 9 mm deep, leaving 1 mm to structurally support the block. There is no depth of interaction encoding. The scintillator light is carried by a 100 mm long multi-clad fibre optic bundle to a

position sensitive photomultiplier tube (PS-PMT). The fibre optic coupling permits the larger PS-PMT to be positioned away from the smaller detector block to allow closer packing of the detector blocks. The PS-PMT (Hamamatsu R5900-C8) has eight anodes tied together through a resistor chain to give four outputs. The signal outputs are fed into preamplifiers and integration circuitry on the four boards at the backside of the PMT. The basic detector block of the MicroPET R4 is shown in **Figure 5-9**.

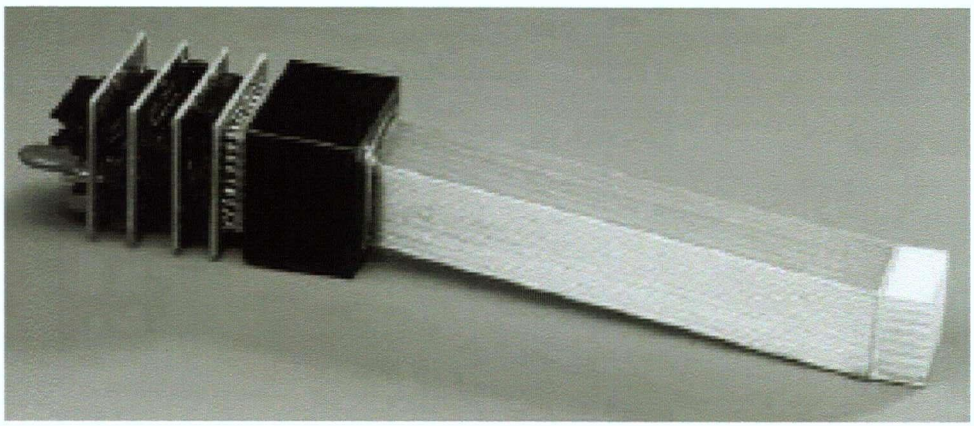

Figure 5-9 The detector block unit from the MicroPET R4 tomograph. An LSO cut-block scintillator is optically coupled to a position sensitive PMT through a multi-clad fibre-optic bundle. Four boards at the backside of the PMT provide front-end readout. From reference [99], Used with permission.

Four detector blocks are bundled into a module or cassette with a common high voltage supply but separate detector readout channels, so each module has 8 x 32 crystals. The MicroPET R4 has 24 modules arranged in a ring around the aperture, the long side of the module in the axial direction. The tomograph has 4 detector blocks (32 crystal rings) in the axial direction and 24 detector blocks (192 crystals) per ring for a total of 96 detector blocks and 6144 crystals.

5.3.2 MicroPET R4 Electronics

The analog signals from the modules are sent to 24 analog subsection boards, each with 4 independent signal channels. Each channel provides a variable gain receiver, crystal address identification and digitization, energy signal digitization and thresholding. Both crystal identification and energy thresholding use on-board, user-definable look-up table information. As well, each channel has a summed signal which is sent to a constant fraction discriminator to produce a time stamp for each event.

The digital signals from the analog subsection boards are sent to one of two detector head interface boards which adds a detector block identification tag. Then, the signals and count rate information are passed to a digital coincidence controller that buffers events and determines which events are in prompt and delayed coincidence according to the user defined T_{CTW}. Coincidences are also restricted to be within the electronic field of view. All the event information for valid coincidences, including detector pair, time tags and coincidence type (prompt or delayed), are finally put into a 64 bit word that is sent by a fibre optic cable to the acquisition computer and the event information is stored in list mode.

The MicroPET uses an Intel CPU based computer system running Windows XP™ (Microsoft™) for the acquisition/reconstruction computer platform with no additional hardware. A proprietary software suite consisting of "MicroPET Manager™" [97] and "Asipro™"[98] are used to acquire, histogram, reconstruct, process and analyze the data.

5.3.3 Transmission Scanning System

The MicroPET R4 transmission scanning system uses a point source which moves in a helical orbit as it is translated along the axial FOV. The acquisition may be done using a windowed coincidence mode with a ^{68}Ge point source. However, since the source orbits close to the detectors a singles source, such as ^{57}Co (E_γ=122 keV, 136 keV), is preferable to give higher count rates and reduced scanning times. For singles transmission scanning, the source motion is controlled by an encoded motor that constantly measures the source holder position. From the

source and detector positions, the lines of response of detected single photon events are calculated and used to generate transmission sinograms. This transmission scanning system is also used for the blank scans and may be used for normalization scans. Alternately, a uniform cylinder of radioactivity may be used for normalization.

5.3.4 MicroPET R4 Histogramming and Reconstruction

The MicroPET R4 tomograph has 32 rings of 192 crystals for a total of 6144 crystals. It acquires in 3D list mode, including oblique LORs, leading to large data sets. The list mode data are histogrammed into sinograms based on the selected span, mash and maximum ring difference parameters. A typical 3D acquisition (span = 3, maximum ring difference = 31) produces 63 direct and 640 oblique sinograms for a total of 703. These are grouped into "segments" related to the average ring difference. For span = 3 and maximum ring difference = 31, there are 21 segments, 1 for the direct planes and 20 (±10) for the oblique planes. The direct segment contains 63 slice planes and the oblique segments contain a decreasing number of sinograms (59 sinograms for the segments with an average ring difference of ±2, down to 5 sinograms for the segments with an average ring difference of ±29).

The standard sinogram size is 84 radial x 96 angular bins. The LORs measured by offsetting one detector are interleaved in the radial binning to increase the radial sampling distance to half the detector size and satisfy the Nyquist criterion (**Figure 5-7**). For 192 detectors per ring, this should produce 96+95 = 191 bins over the ring diameter of 148 mm. However, the sinogram is electronically truncated to a radial FOV of 100 mm to reduce the arc and parallax effects, decreasing the number of radial bins to 84. The radial bin size in this configuration is 1.2 mm at the radial centre and becomes smaller with increased displacement due to the arc effects. Arc effects are corrected prior to reconstruction.

Data binned with 84 x 96 sinograms, span = 3 and maximum ring difference = 31 (703 sinograms) have a total of 5,668,992 LORs per data set. The data are stored as 4 bytes per LOR for a total size of 22 MB. The prompts and delays may be binned separately, or the delays may be subtracted

during histogramming. The list mode data may also be binned into static, dynamic or gated (if available) data sets. The 3D data may be further rebinned into 2D sinograms before reconstruction using SSRB or FORE.

Tomographic reconstruction may then be performed using the standard methods such as 2D filtered backprojection (FBP) and 2D ordered subset expectation maximization (OSEM). If 3D sinograms are used, 3DRP and 3D OSEM/MAP reconstruction are available. Typically, the slice images are reconstructed at 128 × 128 voxels with 63 slices with a voxel size of 0.845 × 0.845 × 1.211 (=0.865) mm^3.

5.3.5 MicroPET R4 Performance

Measured performance values for the MicroPET R4 have been published [99][100]. The performance measurements of the similar MicroPET P4 (primate scanner) and other small animal PET scanners are also available [96][101].

For the MicroPET R4, the spatial resolution measured with a 1 mm ^{22}Na point source at the radial and axial centre was FWHM = 1.65 mm (radial), 1.66 mm (tangential) and 1.85 mm (axial). At a radial offset of 5 mm, the FWHM increases to 2.61 mm (radial) 2.27 mm (tangential) and 2.50 mm (axial). The point source equivalent sensitivity at the axial and radial centre of the tomograph was measured with a ^{68}Ge line source and attenuating aluminum sleeves [102]. After corrected for attenuation and source branching fraction, these were found to be 4.37% for a 250-750 keV window, 2.45% for a 350-650 keV window and 1.86% for a 410-613 keV window.

The energy resolution was measured for every crystal in the tomograph. The values varied between 17% and 36% with the averaged tomograph value of 23%. The scatter fractions were measured with 30 mm and 60 mm diameter scatter phantoms representing, respectively, a mouse and a rat. The scatter fractions were 30% and 42% with a 250-750 keV, and 18% and 28% with a 350-750 keV, for the mouse and rat phantoms, respectively. The count rate performance and NECR were also measured using different sized cylindrical phantoms and different energy windows. The maximum true + scatter count rates using a 350-750 keV window were 411 kcps (@1240

kBq/ml), 317 kcps (@552 kBq/ml) and 290 kcps (@161 kBq/ml), respectively, for the mouse, rat and 10 cm phantoms. The maximum NECR using a 350-750 keV window were 168 kcps (@824 kBq/ml, 91 MBq total) and 89 kcps (@298 kBq/ml, 81 MBq total) for the mouse and rat phantoms, respectively.

The background radioactivity from the LSO scintillator influences the low count rate performance of the MicroPET R4 [103]. The count rates with an empty aperture due to the ^{176}Lu have been measured with different energy windows [104]. For a 250-750 keV energy window, the singles rate = 70.9 kcps, trues rate = 1032 cps, delays rate = 6.7 cps and prompts rate = 1039 cps. For the 350 to 750 keV energy window, the singles rate = 52.2 kcps, trues rate = 80.1 cps, delays rate = 3.7 cps and prompts rate = 83.8 cps. High background singles rates could cause errors in the calculated randoms rates and distributions if they are not taken into account.

5.4 The MicroPET R4 Detector Model

5.4.1 Introduction

The model-based calculation of the singles count rates requires modeling the physics of the radiation interactions in the object and in the tomograph detectors. Therefore, the specific design and performance characteristics of the tomograph being modeled must be included in the calculation. In this Section, the details of the MicroPET R4 tomograph relevant to the detector model used in this calculation are discussed.

5.4.2 Detector Binning, Solid Angle Calculations and Attenuation Object Sampling

The accuracy, speed and memory requirements of the randoms calculation depend primarily on the number of crystals used in the tomograph detector model. Ideally, the number of crystals in the calculation should equal the number of crystals in the tomograph. In scanners with an extremely large number of crystals, the burden of calculating the singles rates to each crystal would cause unreasonably large calculation times. In such cases the detector binning should be down

sampled. However, since the MicroPET R4 tomograph has only 6144 crystals, the singles calculation may be performed for every real crystal within a reasonable time.

The solid angle of each crystal is calculated using the physical crystal area (2.1 × 2.1 mm) rather than the area of the crystal spacing (2.4 × 2.4 mm). The solid angle is calculated using the position of the mean depth of interaction, rather than the front face of the crystal. For 511 keV photons in a 10.0 mm thick LSO crystal this depth is 4.6 mm. Thus, while the tomograph ring has a physical radius of 74.0 mm, the effective radius for the solid angle calculation is 78.6 mm. The effect of non-normal incident angle on effective detector area is also included in the solid angle calculation.

The attenuation object is sampled along the line from the activity sample point to the detector in order to calculate the photon survival (**Section 4.4.1**). The computation time depends directly on the size of the sampling interval, *ds*. The MicroPET attenuation image is reconstructed with the voxel size = 0.845 x 0.845 x 1.211 (=0.865) mm^3; thus, *ds* should not be < 1mm. If the sampling interval is too large, the photon survival calculation does not properly account for changes in the attenuating medium. Therefore, a sampling interval of *ds* = 3 mm was chosen as a compromise between accuracy and speed.

5.4.3 Detector Efficiencies

The MicroPET R4 detectors consist of 1.0 cm thick LSO. The effect of the crystal gaps is modeled by reducing the effective crystal thickness by the ratio of the detector size to the detector spacing (2.1/2.4 = 88%). Thus, at normal incidence, the effective crystal thickness is $x_{det,eff}$ = 0.88 cm. For 511 keV photons, the total attenuation coefficient of LSO (μ_{LSO}) is 0.88 cm^{-1}. Therefore, using **(4.10)**, for normally incident photons, the MicroPET detectors have ε_{int} = 54%. The detector efficiency improves with increasing incident angle because of the increased effective detector thickness.

The detector efficiency for the photons that did not scatter in the object is given by **(4.14)**. The detection efficiency correction factor, ε_{det}, is used to account for the effect of the energy window

on efficiency. $\varkappa_{det}$ varies with the detector design and the energy window settings. In the following discussion, the value of $\varkappa_{det}$ is estimated for the MicroPET R4 model with a 350 keV energy threshold using the procedure outlined in **Section 4.5.2**.

The effect of the energy window on the total detection efficiency may also be modeled using the window fraction, f_{win}, which is simply the fraction of the interacting photons that are counted **(4.9)**. The value of f_{win} may be estimated for the case when no photons scatter in the object, since the effects of scatter are accounted for in the photon survival calculation (**Section 4.6**). 511 keV photons interact in LSO by photoelectric absorption (33%), Compton scatter (62%) and coherent scatter (5%)[105]. All photons that are photoelectrically absorbed deposit 511 keV in the detector. These events are above the energy threshold and counted. Photons that coherently scatter are assumed to deposit no energy in the detector and are not counted. According to the Compton equation **(1.2)**, 511 keV photons that Compton scatter in the detector deposit energy through the recoil electrons up to a maximum of 340 keV. Although, these should all be rejected by the 350 keV threshold, energy resolution blurring causes a small fraction of the single scattered photons to be counted, as shown in **Figure 5-10.**

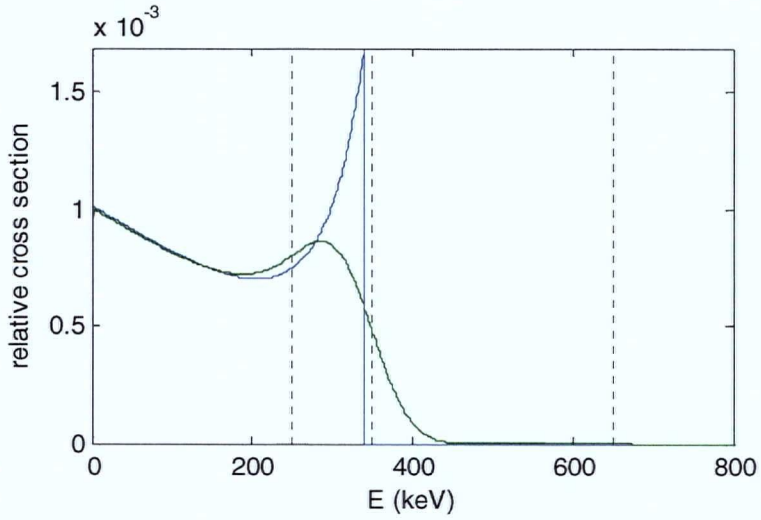

Figure 5-10 The distribution of the energy deposited by 511 keV photons Compton scattered in the detector (blue). This is convoluted with an energy blurring function (FWHM = 23% at 511 keV) (green). The black dashed lines show the 350-650 and 250-650 keV energy thresholds.

For the 23% energy resolution of the MicroPET R4, ~ 5% of these events are above the 350 keV threshold. The total contribution of the 511 photons that undergo single Compton scattering in the detector is then 3% (62% x 5%). Therefore, the total fraction of 511 keV photons that are detected when using a 350 keV threshold is 36% (33% from photoelectric absorption and 3% from single Compton scatter in the detector). This is a lower limit estimate of f_{win}. However, it does not take into include the photons that undergo Compton-absorption, or multiple scattering in the detector that would increase f_{win}.

Using this value, a lower limit estimate for $\varkappa_{det}$ may be found by equating **(4.9)** and **(4.14)**, the two different formulae for ε_{det}:

$$\varepsilon_{det} = f_{win}(1-e^{-\mu_{det}x_{det,eff}}) \approx (1-e^{-\kappa_{det}\mu_{det}x_{det,eff}}) \qquad (5.1)$$

Setting f_{win} = 0.36 and solving **(5.1)** for $\varkappa_{det}$ yields $\varkappa_{det}$ = 0.28. Again, this is lower limit estimate; the true value would be higher. The optimal value is $\varkappa_{det}$ is based on empirical data (**Section 6.3.2**).

5.4.4 Broad-Beam Correction Factor

Essentially all the interactions of 511 keV photons in tissue-equivalent materials are by Compton scatter. Since the MicroPET R4 is designed for imaging small rodents, it has a small transverse field of view (100 mm) and a small axial field of view (78 mm.) This limits the size of the subjects so that the maximum possible pathlength of photons in the subject is ~130 mm. More realistically, the diameter of a rat and a mouse are approximately 60 and 30 mm, respectively, so the average pathlength of photons in the animals would be ~30 and 15 mm. Using the attenuation coefficient for water, it may be estimated that < 15% of the single photons would scatter in a mouse and < 25% in a rat. Therefore, in these imaging situations, the attenuation and scatter of single photons is small and does not alter the data significantly. This also implies that multiple scatter is negligible.

The photon survival calculated uses a broad-beam correction factor, $\varkappa_{broad}$, to correct the narrow-beam attenuation coefficients for photon scatter in the object (**Section 4.6**). The value of $\varkappa_{broad}$ may be estimated from the fraction of the object-scattered single photons that are counted, $f_{scat,abs}$, using the procedure outlined in **Section 4.6.2**.

The value of $f_{scat,abs}$ is estimated for a MicroPET R4 tomograph with a 350 keV energy threshold using the energy distribution of the object-scattered photons that are fully absorbed in the detector, $P_{scat,abs}(E_{sc})$. This, following **(4.20)**, is given by:

$$P_{scat,abs}(E_{sc}) = \left[f_{KN}(E_{sc}) f_{abs}(E_{sc}) (1 - e^{-\mu(E_{sc}) < x_{det,eff} >}) \right] \otimes f_G(E_{sc}, E_{sc,o}) \quad (5.2)$$

where
$f_{KN}(E_{sc})$ = energy distribution of Compton scattered photons
$f_{abs}(E_{sc})$ = fraction of photoelectric interactions
$\mu(E_{sc})$ = total attenuation coefficient of the detector
$< x_{det,eff} >$ = average, effective detector thickness
$f_G(E_{sc}, E_{sc,o})$ = an energy dependent, Gaussian energy blurring function.

$f_{KN}(E_{sc})$ is given by the Klein-Nishina equation **(4.16)**. For the MicroPET R4, $f_{abs}(E_{sc})$ and $\mu(E_{sc})$ for LSO are used [105]. The effective detector thickness $\varkappa_{det,eff}$ for scattered photons depends on their incident angles. Since the paths of the scattered photons are not explicitly calculated, an average

effective crystal thickness $\langle x_{det,eff} \rangle$ is used. In the MicroPET detector model, the normally incident effective thickness was taken to be 8.8 mm (**Section 5.4.3**). Scattering from the radial and axial centre of the tomograph would result in incident angles up to 26°. Scattering from near the axial edge would result in incident angles up to 45°. This range of incident angles corresponds to a range of effective detector thicknesses from 8.8 - 12.4 mm. Therefore, the average incident angle is about 26° and $\langle x_{det,eff} \rangle \approx$ 10 mm. Finally, the energy blurring function in the calculation of $P_{scat,abs}(E_{sc})$ uses the MicroPET energy resolution of 23% at 511 keV.

Figure 5-11 shows all the stages of this calculation: the energy distribution of the Compton scattered photons, $f_{KN}(E_{sc})$, then corrected for intrinsic efficiency (using $\mu_{LSO}(E_{sc})$ and $\langle x_{det,eff} \rangle \approx$ 10 mm), then further modified by $f_{abs,LSO}(E_{sc})$ and finally the total distribution blurred by $f_G(E_{sc})$. All values of attenuation coefficients are taken from [105]. The four plots show the various factors in the final calculation of $P_{scat,abs}(E_{sc})$.

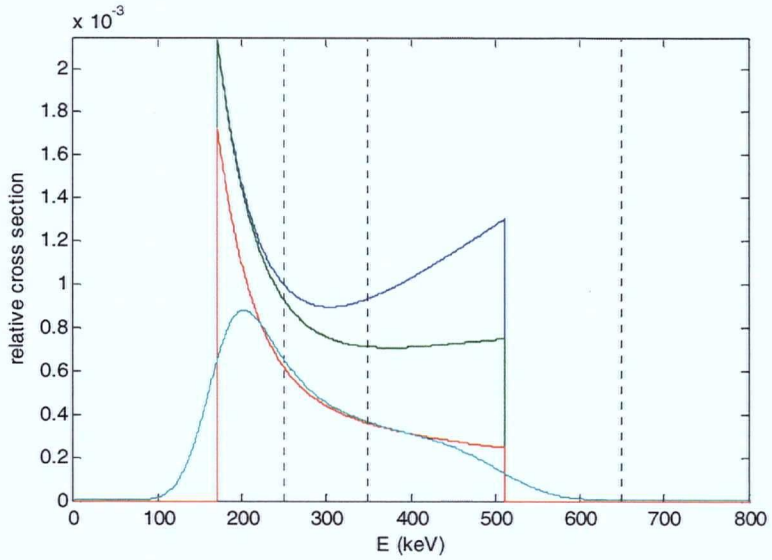

Figure 5-11 The energy distribution of photons Compton scattered in the object, f_{KN}, (blue). This is corrected by the intrinsic efficiency (green), the fraction of photoelectric absorption in the detector $f_{abs,LSO}(E_{sc})$ (red) and convoluted with an energy dependent energy blurring function (teal). These assume $\langle x_{det,eff} \rangle$ = 10 mm and energy resolution = 23% at 511 keV. The black dashed lines show the 250, 350, and 650 keV energy thresholds.

The fraction of the object-scattered photons that were photoelectrically absorbed in the detector, $f_{scat,abs}$, is found by integrating $P_{scat,abs}(E_{sc})$ within the energy window and normalizing to the total scattering cross section **(4.21)**. Using the $P_{scat,abs}(E_{sc})$ calculated above (based on the MicroPET R4 detector model) and a 350-650 keV window, gives $f_{scat,abs}$=12.5%.

$f_{scat,abs}$ does not include the fraction of the object-scattered photons that *Compton scatter* in the detector and fall within the 350-650 keV window, $f_{scat,cs}$. This also contributes the total fraction of object scattered photons that are counted. Calculating by a similar method gives $f_{scat,cs}$=0.5%. The fraction of object-scattered photons that undergo *Compton-absorption* in the detector cannot be calculated analytically and is not included in this analysis. Therefore, the lower limit of the fraction of the object-scattered photons that are counted is the sum of the two calculated contributions, $f_{scat,tot} = f_{scat,abs} + f_{scat,cs} \approx 13\%$.

The value of the broad-beam correction factor, $\varkappa_{broad}$, is now found based on $\varkappa_{det} \approx 0.28$ and $f_{scat,tot} \approx 0.13$. As described in **Section 4.6.2,** the value of $\varkappa_{broad}$ is found by equating **(4.24)** and **(4.25)**, then solving for $\varkappa_{broad}$. Combining these equations yields

$$P_{surv}\varepsilon_{\text{det}} = e^{-\varkappa_{broad}\mu_{obj}x_{obj}}(1-e^{-\varkappa_{det}\mu_{det}x_{det,eff}}) \approx e^{-\mu_{obj}x_{obj}}(1-e^{-\varkappa_{det}\mu_{det}x_{det,eff}}) + f_{scat,tot}(1-e^{-\mu_{obj}x_{obj}}) \quad (5.3)$$

The calculation is not very sensitive to the values used for μ_{obj} and x_{obj}. For x_{obj} = 5.0 cm of water (μ_{obj} =0.0958 cm^{-1}), $\varkappa_{broad} \approx 0.28$. Again, this preliminary value does not take into account Compton-absorption in the object or the detector. Therefore, the optimal value of $\varkappa_{broad}$ requires further refinement based on empirical tests (**Section 6.3.3**).

5.4.5 Crystal Block Structure

Variations in the relative crystal efficiencies cause sharp diagonal lines in the randoms sinograms (**Section 4.7.3**). A simple model of the crystal efficiency variations within the detector block of the MicroPET R4 was used to reproduce these in the randoms calculation. Preliminary values of the efficiencies in a detector block were found using a Monte Carlo simulation of the detector block. Then, the symmetries of the crystal location were used to the identify crystals that should have the

same efficiencies from purely systematic considerations. It was found that within a block of 64 crystals only ten unique efficiency values were required. The efficiencies found from the simulation were then averaged according to their block locations to determine the ten efficiency values. These values were normalized to bring the total block efficiency to unity. The efficiency values were further adjusted to improve the fit of the calculated randoms distribution to the high frequency details in the measured randoms distribution. The relative efficiencies within the model of the MicroPET R4 detector block are shown in **Figure 5-12**.

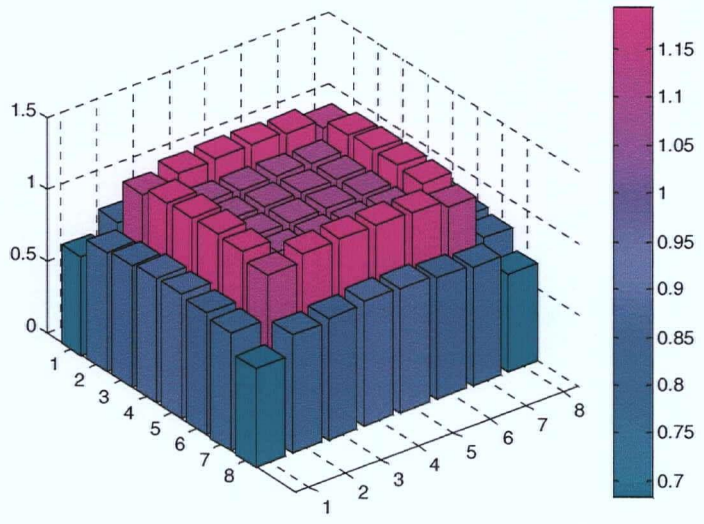

Figure 5-12 Relative detector efficiencies in detector block model.

This model only reproduces systematic block structure effects; random variations in crystal efficiency are not included. These would result in random variations in the relative amplitudes of the individual diagonal lines in the randoms sinograms. As well, the systematic variations change with PMT drift, so the block structure model may require adjustment over time. The relative efficiencies also depend on the energy window settings. The present model is only used with a 350-650 keV window.

5.4.6 Dead-Time Correction

The randoms calculation requires the measured randoms and singles rates to be dead-time corrected. The MicroPET software calculates a global correction factor, $f_{deadtime} > 1$, for the coincidences (trues and randoms), but not for the singles rates. Since the MicroPET calculation of the dead-time correction factor is proprietary, the exact relationship between singles and coincidence dead-time is unknown [106]. However, the measured singles and coincidences are processed identically in the MicroPET until the coincidence processor. As well, the scintillator decay time is largest contribution to detector dead-time. Therefore, a dead-time correction factor for the singles rates may be based on the values of $f_{deadtime}$.

The randoms are measured as delayed coincidences in the same digital coincidence processor as the trues, so $f_{deadtime}$ is equally valid for trues or randoms. Given that the randoms rates are proportional to the square of the singles, the dead-time correction for singles should be roughly the square root of the correction for coincidences. Therefore, a dead-time correction factor of $f_{deadtime}^{1/2}$ was used for the measured single rates. A further, an empirically determined, correction of $f_{deadtime}^{1/4}$ was applied to the calculated randoms sinograms to bring calculated and measured values of randoms rates at high count rates into better agreement.

5.4.7 Summary of Calculation Parameter Optimization

The following calculation parameters require further adjustment based on the experimental validation studies:

- detector efficiency correction factor, $\varkappa_{det}$,
- broad-beam correction factor $\varkappa_{broad}$, and
- radioactivity object sampling parameters, threshold and sampling density.

Experiments were performed to determine the optimal values of these parameters, and the sensitivity of the randoms calculation to those values (**Section 6.3**).

Chapter 6

Experimental Validation of the Randoms Calculation

6.1 Measurements

6.1.1 Chapter Overview

Chapter Six examines the validation experiments used to test the calculated randoms correction. The chapter begins with a description of the experimental details of the phantom and animal studies. Next, the Figures of Merits used to compare the measured and calculated randoms corrections are discussed. Then, the details of the calculation parameters used in the randoms correction are described. The bulk of the chapter gives the results of the experiments and compares them with the corresponding results from the randoms calculation. The overall significance of the results is discussed in **Chapter Seven.**

6.1.2 Introduction

The accuracy and efficacy of the model-based randoms correction method were assessed using phantom and animal experiments done on the MicroPET R4 PET tomograph. Since the MicroPET R4 allows the delayed coincidences to be stored separately, the randoms distributions may be directly measured. In early development, the calculated randoms distributions were compared with those generated by Monte Carlo simulations using SimSET [107]. However, because SimSET does not directly simulate random coincidences or include a block detector model for PET tomographs, the value of the simulations was limited. The GATE simulation program was later available, but was not then validated for the MicroPET R4 [108]. Therefore, it was decided to perform validations using only measured data.

The following studies were made on the MicroPET R4:

- A high activity, off-centre line source was imaged in air for 12 hours. This provided a data set with a large number of counts so that individual count profiles could be examined. The high initial count rates also allowed the effects of high dead-times to be assessed.

- Point sources in air-filled and water-filled cylinders were scanned at different positions in the FOV. These experiments assessed the accuracy of the randoms calculation for activity at different positions in the tomograph.

- Uniform cylinders were scanned to assess the accuracy of the calculation for larger objects and radioactivity distributions. As well, one cylinder was scanned at different axial positions so that the effects of radioactivity outside the axial field of view could be studied. Another scan was done on a cylinder with very high activity to measure image noise at high randoms fractions.

- Contrast phantoms consisting of a sphere within a cylinder, each with different radioactivity concentrations, were also scanned. These experiments assessed the accuracy of the randoms calculation for complex radioactivity distributions. As well, the effects of the measured and calculated randoms on the reconstructed contrast phantom images were studied.

- A mice study was used to assess accuracy of the randoms correction in a realistic scanning situation. As well, the effects of the measured and calculated randoms on the reconstructed mice images were evaluated.

All studies used ^{18}F ($\tau_{1/2}$=110 min), with the exception of the high activity cylinder which used ^{11}C ($\tau_{1/2}$=20 min). The emission scans were acquired on the MicroPET R4 using a 350-750 keV energy window and a coincidence window of T_{CTW} = 6.0 ns. Acquisition times were varied depending on the source radioactivity and the count requirements of the study. The blank and transmission scans used a ^{57}Co point source and acquisition times of ~12 minutes and were performed post-injection.

6.1.3 High Count Study Using a High Activity Line Source in Air

A high radioactivity (~40 MBq), ~ 1 mm diameter, off-axis line source in air (**Figure 6-1**) was scanned for 12 hours The source was 44 mm long, approximately half the length of a mouse body. The study was histogrammed into one 12 hour time frame to obtain a high count, low noise randoms distribution. The study was also histogrammed into 12 – one hour time frames to assess how the randoms rates and distributions vary with count rate.

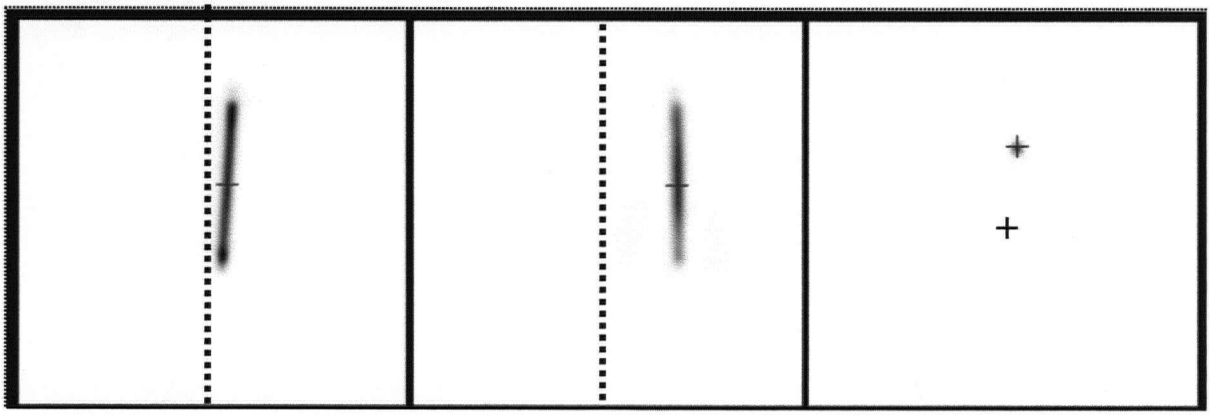

Figure 6-1 Reconstructed coronal (left), sagittal (centre) and transverse (right) slice images of the off-axis line source. The lines and cross hair mark the approximate position of the tomograph axis.

6.1.4 Point Sources in Air-filled and Water-filled Cylinders

Point sources were scanned at various positions in air-filled and water-filled cylinders in the tomograph imaging volume. These studies provided a test of the total photon detection model (solid angle, photon survival and detector efficiency) from different axial and radial positions within the FOV. Two scans were done for each position. The bottle was first filled with non-radioactive water and scanned. The scans with water were done first to maximize the activity when attenuation reduces the count rates. After scanning, the water was removed and the phantom was repositioned with the point source at the same location and scanned again. The measurements in air isolate the solid angle and detector efficiency parts of the calculation. The measurements in water include the additional effects of the photon survival (and scatter), so that the parts of the calculation may be studied separately. High activities were used to produce elevated randoms fractions and allow the acquisition of a large number of randoms counts. Scan durations of 30 to 60 minutes were used depending on the source activity. All experimental parameters are listed in **Table 6-1**.

Table 6-1 Experimental parameters of the studies with a high activity point source at various positions in air-filled and water-filled cylinders. There are no scans position labelled 3 and 4.

Study position number and cylinder filling	Initial Activity (MBq)	Scan Time (min)	Position (mm)		
			x ±0.4 mm	y ±0.4 mm	z ±0.6 mm
1 (water)	37.99	30	-4.7	+5.5	-4.9
1 (air)	25.53	30	-4.7	+4.7	-4.9
2 (water)	15.11	60	-6.3	20.7	0.0
2 (air)	5.54	60	-5.5	19.9	1.2
5 (water)	31.22	30	5.5	-4.7	21.8
5 (air)	16.71	60	5.5	-6.3	20.6
6 (water)	8.29	60	-18.2	0.4	20.6
6 (air)	3.58	60	-18.2	-0.4	20.6
7 (water)	19.99	30	0.4	0.4	35.1
7 (air)	13.51	30	-0.4	-0.4	33.9
8 (water)	8.31	58.7	-0.4	-14.8	33.9
8 (air)	4.48	60	-0.4	-15.6	33.9

The sources used liquid samples of ^{18}F with high initial activity concentrations. Point sources were made by injecting a small volume (~5 μl) of radioactivity into a small bore capillary tube using a narrow gauge syringe. Care was taken to not smear out the radioactivity along the tube walls. The tube was sealed and the activity measured in a dose calibrator. The tube was then implanted into a high density polystyrene mesh/foam and mechanically secured into the neck of a 500 ml Nalgene water bottle, as shown in **Figure 6-2.** The bottle was approximately the size of a large rat, with the outer diameter = 69 mm, length from bottom to neck = 142 mm, total length = 167 mm, the wall thickness = 2.0 mm. The point source positions in the bottle are shown in **Figure 6-3**. Only positions on one end were used because the tomograph response was assumed to be symmetric about the axial centre.

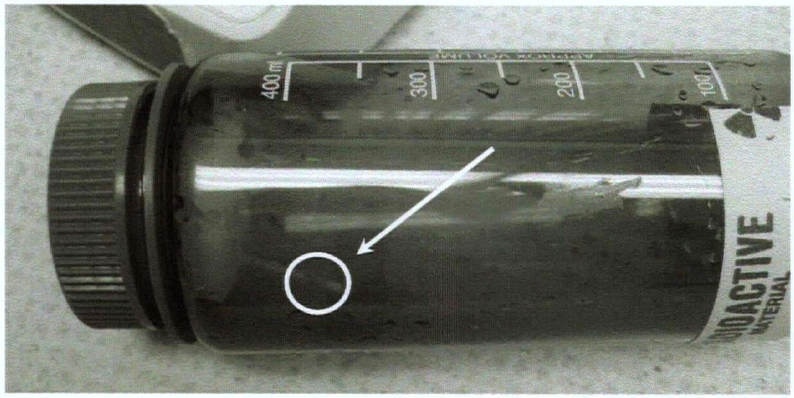

Figure 6-2 The large water bottle used in the point source measurements. The tube containing the point source is seen at the left, sticking out of the neck of the bottle.

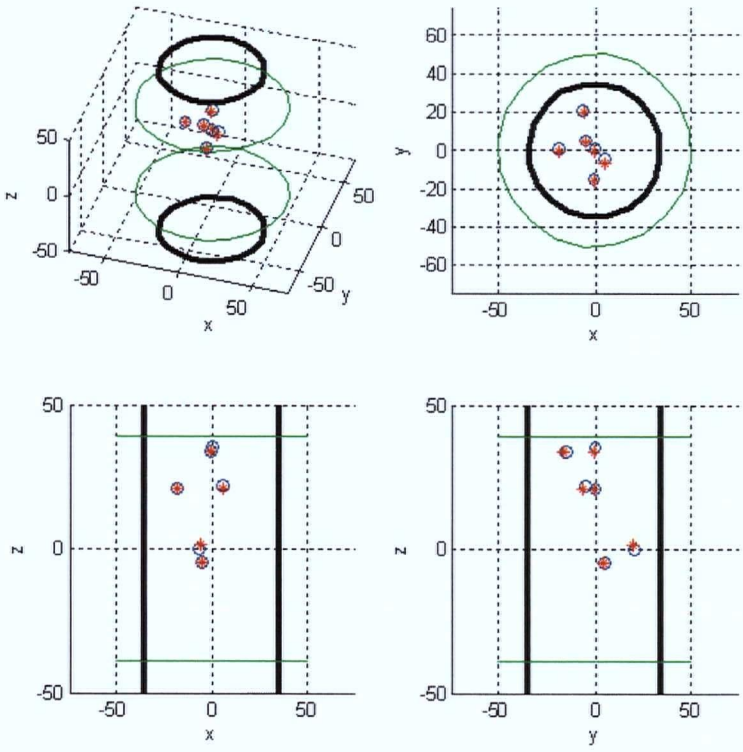

Figure 6-3 Positions of point sources in an air-filled cylinder (red asterisks) and the corresponding positions in a water-filled cylinder (blue circles). The green lines show the electronic aperture of the tomograph. The black lines show the location of the phantom cylinder walls.

High activity point sources in more complex attenuation distributions were also scanned. One scan used a point source in air positioned beside a plastic water-filled ampoule (**"**complex point 1"), as shown in **Figure 6-4**. Another scan was done of a point source inside a water-filled cylinder beside an air-filled sphere ("complex point 2"), as shown in the **Figure 6-5.** The experimental parameters are listed in **Table 6-2.**

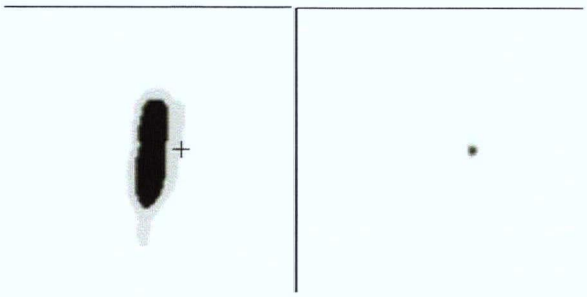

Figure 6-4. A coronal slice of the reconstructed attenuation (left) and radioactivity (right) images for the point source in air beside a water-filed ampoule ("complex point 1"). The cursor in the attenuation image marks the position of the point source.

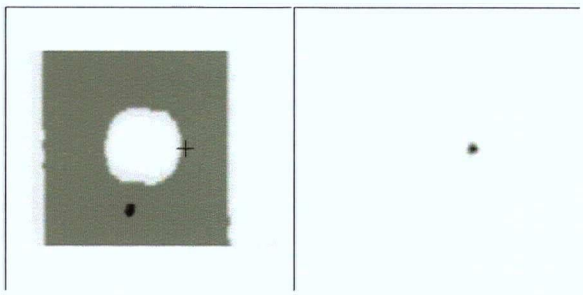

Figure 6-5 A sagittal slice of the reconstructed attenuation (left) and radioactivity (right) images for the point source in a water-filled cylinder beside an air-filed sphere ("complex point 2"). The cursor in the attenuation image marks the position of the point source.

Table 6-2 Studies with a high activity point sources in complex attenuation objects.

Study	Initial Activity (MBq)	Scan Time (min)	Point Source Position		
			x (mm)	y (mm)	z (mm)
complex point 1	4.48	60	12.2	2.9	0.0
complex point 2	8.31	58.7	1.3	-13.1	0.0

6.1.5 Uniform Cylindrical and Contrast Phantoms

Different sized cylindrical phantoms containing a uniform distribution of radioactivity in water were scanned. The first phantom was a small cylinder about the size of a mouse, which fit completely within the axial FOV. This phantom was scanned with different axial offsets, each with increasing radioactivity outside the axial FOV of the tomograph, as shown in **Figure 6-6**. For this study, transmission scans were done of only the first two scans. The other two scans used an attenuation map created from the reconstructed radioactivity image in which the voxel values in the cylinder were replaced with the attenuation coefficients of water.

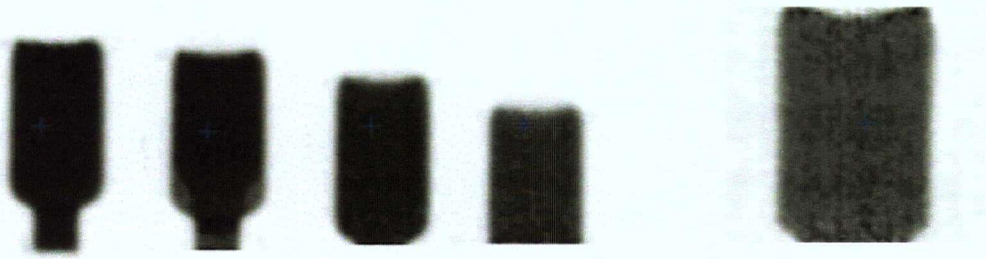

Figure 6-6 Reconstructed images of a small uniform cylinder scanned with increasing axial displacements (0.0, 1.0, 2.0 cm and 3.0 cm) (left). Larger displacements resulted in increased radioactivity outside the axial FOV. The reconstructed image of the larger uniform cylinder is shown on the right.

A second, larger cylinder (approximately the size of a rat) was also scanned. This had a larger diameter and the length extended outside the axial end of the tomograph. The phantom and study parameters are listed in **Table 6-3.**

Table 6-3 Details of the parameters in the uniform cylindrical phantom studies.

Study	Initial Activity (MBq)	Scan Time (min)	diameter (mm)	length (mm)
cylinder 1	20	60	50	~100
cylinder 2 position 1	59	60	30	70
cylinder 2 position 2	34	30	30	70
cylinder 2 position 3	27	30	30	70
cylinder 2 position 4	21	60	30	70

The larger cylinder was also previously scanned with a very high activity of ^{11}C. This study was analyzed for image noise.

Two different contrast phantoms were scanned under different conditions. Both phantoms used a large cylinder but with different sizes of spherical insert. The sphere and the cylinder were filled with different radioactivity concentrations. The radioactivity concentration ratio between the sphere and background varied. Contrast phantom 2 was scanned twice at one position with different total activities and scanning times. It was also scanned at a second axial position, which altered the amount of activity outside the axial FOV and the location of the sphere. The different phantom configurations are shown in **Figure 6-7**. The details of the studies are listed in **Table 6-4**.

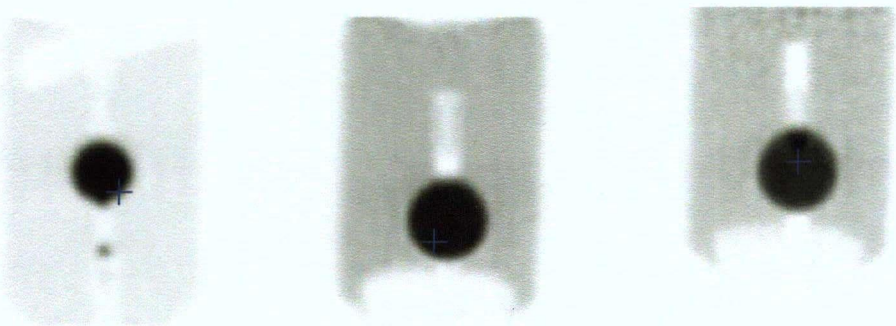

Figure 6-7 Reconstructed images of the three contrast phantom configurations: "contrast phantom 1" (left), "contrast phantom 2" (centre), and "contrast phantom 2a" (right.) Phantoms 2 and 2a are identical except that the entire phantom was moved between the two scans.

Table 6-4 Details of the parameters in the contrast phantom studies.

Study	Initial Activity (MBq)	Scan Time (min)	sphere diameter (mm)	Activity Ratio (T:B)
contrast phantom 1	27.0	58.7	50	7:1
contrast phantom 2 study 1	60.8	5	20	3:1
contrast phantom 2 study 2	58.5	120	20	3:1
contrast phantom 2a (posn 2)	21.4	60	20	3:1

6.1.6 Animal Study

As part of a regular research study, two mice were injected with a total of ~3 MBq of ^{18}F-EF5, an imaging agent which is taken up in hypoxic tumour tissue. A three hour scan was performed. The reconstructed images are shown in **Figure 6-8**.

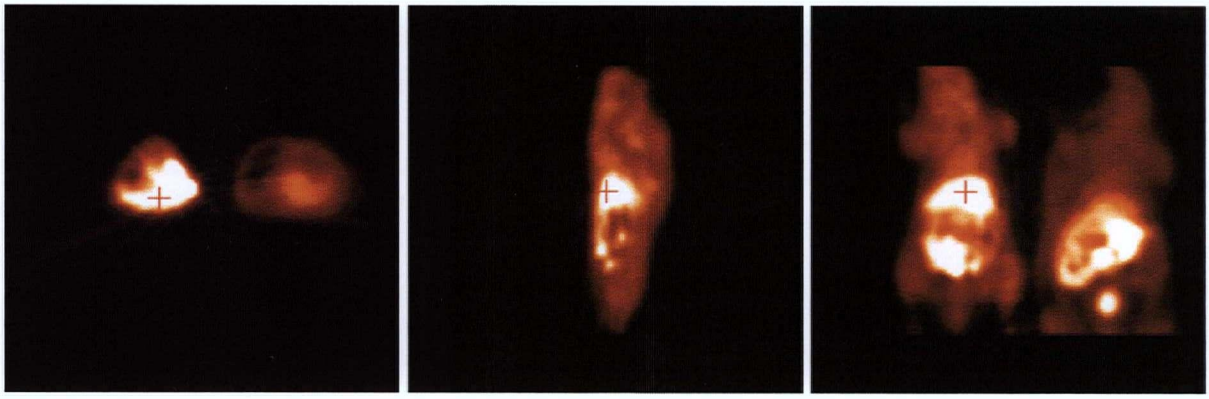

Figure 6-8 Reconstructed transverse, sagittal and coronal slices of the reconstructed scan of two mice injected with ^{18}F-EF5.

6.1.7 MicroPET Acquisition and Processing

All data were acquired using the standard protocol, unless otherwise noted. The acquired list mode data were histogrammed into two data sets for each study: one with the prompt and delayed coincidences stored in separate sinograms, and the other with the delays subtracted. 3D data sets were generated with a sinogram size of 84 radial bins by 96 angular bins using span = 3 and maximum ring difference = 31. This produced a total of 703 sinograms grouped into 21 segments. Data were also rebinned into sinograms using SSRB to increase the counts per slice for comparison with the calculated randoms sinograms. The preliminary radioactivity images used for the randoms calculation were reconstructed from the prompts sinograms using FORE followed by 2D-FBP with normalization, attenuation and dead-time corrections applied. The reconstructed images were 128 x 128 x 63 slices.

The attenuation coefficient images were reconstructed from the transmission scan data. The resulting μ-values for water were ~30% lower than the true value (0.0958 cm^{-1}). This was due to the scatter of the photons from the singles transmission source [109]. Segmentation was done using the standard MicroPET procedures to give correct values. First, the attenuation coefficient images were first smoothed using a Gaussian filter with a FWHM of 3 pixels in both the transverse

axial directions. Regions of interest were drawn around volumes of known attenuating media, usually a water volume or the patient bed, and the material composition was identified. The attenuation values were then scaled to the known values. Next, the attenuation image voxels were segmented according to their new rescaled values. A number of thresholds were placed on the histograms of the object μ-values to define the regions that have same composition and μ-values. The thresholds were adjusted until distinct structures (such as the animal bed or phantom boundaries) were seen on the preliminary segmented image. When the thresholds were finalized, the segmented image was created. This was reprojected to form new transmission sinograms and new ACFs were generated. The preliminary radioactivity image was then reconstructed using the new ACFs. **Figure 6-9** shows histograms of the same attenuation image voxel values before and after segmentation.

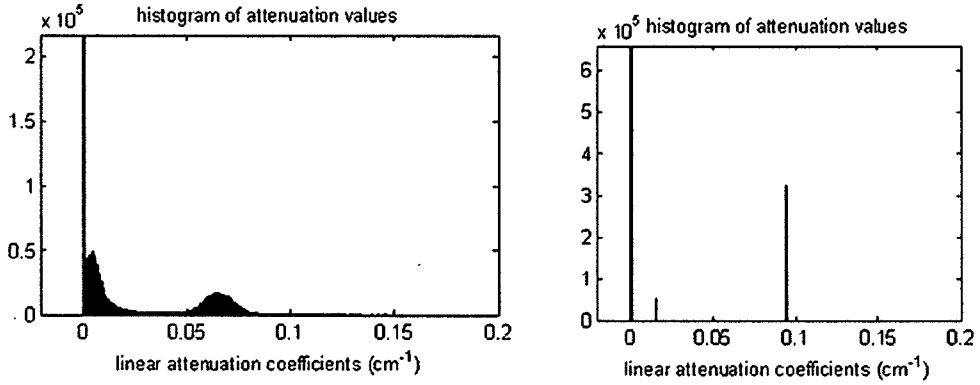

Figure 6-9 Histograms of attenuation coefficient values from the transmission scan of a water-filled cylinder using a ^{57}Co singles source. The uncorrected histogram (left) shows a water peak at an erroneous value of 0.065 cm^{-1}. The histogram of the segmented attenuation object (right) shows only discrete attenuation values, and the water peak is now at the correct value (0.0958 cm^{-1}.) The y-axis shows the frequency of attenuation values.

6.2 Data Analysis

6.2.1 Introduction

The measured and calculated randoms distributions may differ in three ways:

- inaccuracies in overall scaling,
- statistical noise, and
- biases in the spatial distribution due to inaccuracies in the calculation.

The validation of the model-based randoms correction requires that both the accuracy of the calculated spatial distribution of the randoms, as well as the global scaling, be assessed. The accuracy of the global scaling is found simply by comparing the measured and calculated global randoms rates. The accuracy of the calculated randoms distributions for each study was assessed by visual comparison of the sinograms and count profiles to measured distributions. The pixel values were compared using quantitative figures of merit (FoM). Finally, the effects of the each randoms correction method on the images (noise and bias) were assessed.

6.2.2 Comparison of Count Rates

The measured and calculated global randoms count rates were compared by the percent difference:

$$\%\ difference = \frac{M - C}{M} \times 100\% \qquad (6.1)$$

where M = measured average global count rates.
C = calculated average global count rates.

This gives no information about the accuracy of the spatial distribution, only on the accuracy of the global scaling of the randoms rates. The trues rates were also compared, but the accuracy of the trues calculation has little bearing on the accuracy of the randoms calculations.

6.2.3 Comparison of Randoms Distributions

An assessment of the accuracy of the calculated spatial distribution of randoms requires comparing the pixel values of the measured and calculated randoms distributions. However, the pixel values differ because of both biases and the statistical fluctuations in the measured randoms. Thus, the task is to estimate bias in the presence of noise. In this analysis, the term "bias" is used for the systematic errors in the calculated random distributions that may vary spatially.

Visual comparison of the sinograms was first done to detect any potential gross differences and artifacts in the shapes of distributions. In general, the calculated sinograms are very smooth, but in the majority of the studies, the measured delays sinograms are very noisy. This noise masks both high and low frequency details. Single slice rebinning was used to reduce the 3D data set to a 2D data set, and, thus, reduce the noise in the sinograms. As well, the central transverse slices were mainly examined because this slice is at the peak of the counting sensitivity and has the lowest statistical noise. Sinograms of the sum of the slices were also sometimes used to further reduce the noise. Sinograms of the percent differences **(6.1)** between the pixel values of the measured and calculated sinograms were also calculated. These were very useful in detecting the small differences between the sinograms.

For the highest count studies, the count profiles of individual pixel rows were examined along the different data axes: radial, azimuthal and axial. When the profiles of measured and calculated randoms distributions and plotted simultaneously, biases may be visually detected if the statistical fluctuations in the measured data are small. The 12 hour frame of the off-axis line source study contained an extremely large number of counts (460 million delays); thus, profiles within the 3D data set were also compared, without rebinning. For most studies with a lower number of counts, the data were summed over two out the three axes to form the profiles. For example, the summed radial profiles were formed by summing the data over the azimuthal and axial bins. This was necessary to reduce the noise, so that biases could be detected along the un-summed axis. While these summed profiles have reduced noise, biases in the summed axes may average out. Therefore, summed profiles for each axis must be examined. Finally, profiles of the percent difference

between the measured and calculated summed count profiles were formed to enhance and quantify biases. In the percent difference profiles, biases appear as departures from flatness.

Four quantitative calculated figures of merit (FoM) were also used to assess the bias and noise differences between the calculated and measured randoms distributions based on the differences in the pixel values. These were the normalized mean squared error, *NMSE*, the chi-squared value, "χ^2", the standard deviation of the percent differences, *s.d.(%diff)*, and the 2D correlation coefficient, r_{2D}. The *NMSE* and χ^2 were calculated when comparing sinograms or entire data sets. The *s.d.(%diff)* and 2D correlation coefficient were calculated only when comparing individual sinograms.

In this task, the mean squared error, *MSE*, is the square of the differences between the corresponding pixel values in the two data sets, divided by number of pixels. The *NMSE*, then, is the sum of the square of the normalized differences. For the measured "*M*" and calculated "*C*" data sets, with pixel values, M_i and C_i, and for N pixels, these quantities are defined as:

$$MSE = \frac{1}{N}\sum_{i=1}^{N}\left(M_i - C_i\right)^2 \qquad (6.2)$$

and

$$NMSE = \frac{1}{N}\sum_{i=1}^{N}\left(\frac{M_i - C_i}{M_i}\right)^2 \qquad (6.3)$$

For two identical data sets, *MSE* and *NMSE* = 0. It may be shown that the *MSE* is the sum of the statistical variance and the bias, so the values of *MSE* and *NMSE* have components from both bias and noise. In situations where the bias dominates, NMSE and MSE become a measure of the upper limit of the bias. The *MSE* and *NMSE* are especially useful when evaluating the differences made by different processing of the same data set. For example, optimal values of the calculation parameters were found, in part, by finding the values that minimized the MSE. For individual

studies, the *NMSE* gives an absolute value of the magnitude of the bias if the noise is small compared to the bias.

The chi squared, χ^2, between the pixel values in two data sets is calculated as:

$$\chi^2 = \sum_{i=1}^{N} \frac{(M_i - C_i)^2}{M_i} \qquad (6.4)$$

This may be also normalized to the Chi-squared per pixel, χ^2/N, where N is the number of pixels. The Chi-squared is a measure how closely the variations in pixel values follow Poisson statistics alone. Thus, it may be used to detect the presence of systematic biases. In this task, the χ^2/N is used to compare the smooth distribution (the calculated randoms) to a distribution that contains Poisson noise (the measured randoms). If the difference the between two data sets is purely Poisson, χ^2/N is very close to unity. However, $\chi^2/N > 1$ indicates that the differences in the data sets have a component due to bias. The relative magnitude of biases, however, cannot be quantified by χ^2/N because its value is sensitive to the absolute pixel values. Thus, χ^2/N increases with the absolute number of counts even when the relative bias is unchanged.

The standard deviation in the percent difference values between the measured and calculated distributions is calculated as:

$$sd(\%\,diff) = \frac{1}{N-1} \sum_i \sqrt{\left(\frac{M_i - C_i}{M_i} - \overline{\left(\frac{M_i - C_i}{M_i} \right)} \right)^2} \qquad (6.5)$$

This is a measure of the magnitude of the statistical variations between the pixel values in two data sets. For two identical sinograms *s.d.(%diff)* = 0. For two identical sinograms which differ only by their noise content, *s.d.(%diff)* > 0 and is indicative of the noise. When comparing the noisy measured randoms with the smooth calculated randoms, *s.d.(%diff)* is a measure of the noise in the measured randoms, but *s.d.(%diff)* is also sensitive to biases.

The 2D correlation coefficient, r_{2D}, is a measure of the similarity of two 2D data sets:

$$r_{2D} = \frac{\sum_i \left(M_i - \overline{M}\right)\left(C_i - \overline{C}\right)}{\sqrt{\left(\sum_i \left(M_i - \overline{M}\right)^2\right)\left(\sum_i \left(C_i - \overline{C}\right)^2\right)}} \tag{6.6}$$

For two identical images, $r_{2D} = 1$ and is independent of a scaling factor. r_{2D} is very sensitive to structural differences, but also to noise. For low noise images, it provides an additional measure of the agreement between two images. In low noise situations, low values of r_{2D} indicate significant bias.

These figures of merit must be used in combination to assess the accuracy of the calculated randoms distributions because the magnitude of the statistical noise limits the detectability of any bias. For those studies in which $\chi^2/N \approx 1$, the difference between the calculated and measured data is dominated by the Poisson noise. In this case, the bias is smaller than the statistical noise; making it undetectable. For those tests with $\chi^2/N > 1$, the statistical noise no longer dominates and the other FoMs become more sensitive to bias. In this case, the FoM values become the upper limit of the bias (in the limit of when the statistical noise is zero).

6.2.4 Comparison of Reconstructed Images

The overall effect of the different randoms correction methods on the reconstructed images was assessed by comparing image count profiles and measuring the image noise. The noise was found by measuring mean voxel values in a number of small ROIs position at equal radial distances from the centre of the phantom. The % *noise* is the ratio of the standard deviation of the mean ROI voxel values to the average of these values. This gives an estimate of the image noise, but is sensitive to averaging within the ROI, as well as variations in the image due to attenuation and scatter and their corrections. Such variations could potentially change the purely Poisson nature of the noise.

6.2.5 Testing the Quantitative FoMs

To test the sensitivities of the different quantitative FoMs, a high count measured randoms sinogram was compared with two calculated randoms sinograms: one including the effects of the block structure in the calculation, and the other without. The block structure causes the diagonal pattern in the randoms sinograms. **Figure 6-10** shows the measured sinogram and the two calculated sinograms. The FoMs were calculated comparing the measured central slice sinograms to each of the calculated sinograms. The resulting FoMs are listed in **Table 6-5**.

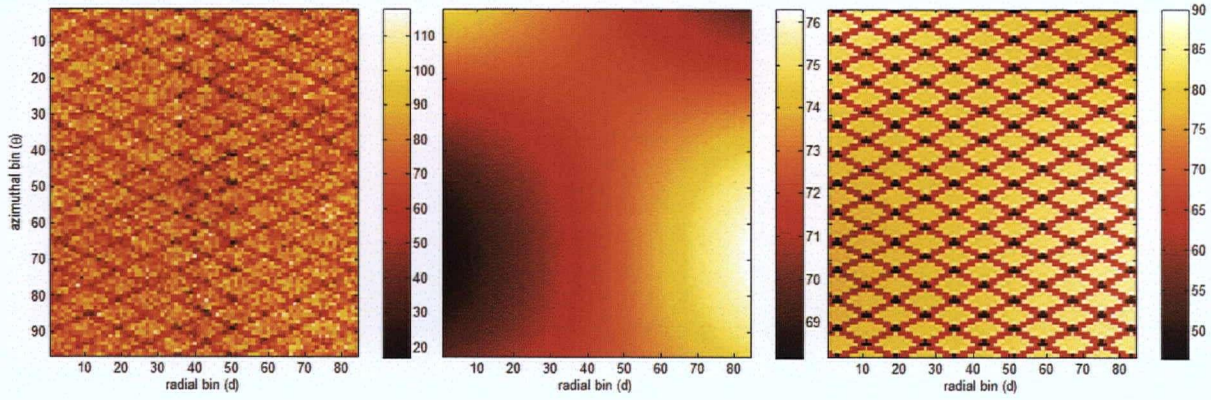

Figure 6-10 The comparison of a measured sinogram (left) to a calculated sinogram without block structure (centre) and a calculated sinogram with block structure (right.)

Table 6-5 The values of the FoMs between measured and calculated randoms distributions in detecting block structure in the central slice sinogram.

calculation parameter	*NMSE* (%)	*sd(% diff)* (%)	χ^2/N	r_{2D} (%)
w/o block	5.33	10.89	2.44	9.0
with block	2.34	8.34	1.29	70.6

The value of every FoM is improved with inclusion of the block structure. The *NMSE* decreased by almost 50%. The *s.d.(% diff)* decreased by ~20%. The $\chi^2/N > 1$ indicates the dominance of the bias. The decrease in the χ^2/N shows that including the block structure brings the difference

between the sinograms closer to being purely Poisson. The 2D correlation coefficient changes the most if the block structure is added; it increases from 9% to 71% for central slice. Thus, these FoMs are able to detect bias when the image noise is low, and the 2D correlation coefficient is most sensitive measure.

6.3 Calculations of the Randoms Distributions

6.3.1 Introduction

The randoms distribution calculation requires the values of the following calculation parameters to be optimized based on experimental results:

- detector efficiency correction factor $\varkappa_{det}$,
- photon survival broad-beam correction factor $\varkappa_{broad}$, and
- radioactivity object sampling parameters: threshold and sampling density.

The experimentally determined values were used in the remainder of the calculations. Also determined was the sensitivity of the results of the randoms calculation to the values of these parameters.

6.3.2 Detection Efficiency Correction Factor

The value of the detection efficiency correction factor was estimated to be, $\varkappa_{det} \approx 0.28$ from physical arguments based on the MicroPET R4 detector model (**Section 5.4.3**). However, because of the simplifications in this calculation, the optimal value is expected to be higher. Randoms distributions calculated with different values of $\varkappa_{det}$ were compared to the measured data from the high activity line source study (**Section 6.1.3**). The line source, being an extended object, averages out any small errors from the calculations of individual points with different solid angles. Since the line source is in air, the effects of attenuation and scatter in the subject are negligible; thus, the results do not depend on the value of the broad-beam correction factor. The comparison used a

one hour frame from the study which was acquired at lower count rates (frame 3 in **Table 6-8**) to minimize the impact of dead-time. The calculation was done with high sampling density (5000 pts/ml) and threshold (20%). The calculated distributions were compared with the measured data by the count rates and quantitative figures of merit. The results are listed in **Table 6-6**.

Table 6-6 Measured and calculated counts rates and FoMs comparing the randoms central slice sinograms from frame 3 of the line source in air for different values of κ_{det}.

κ_{det}	Randoms Rate (kcps)	Trues Rate (kcps)	MSE	χ^2/N
measured rates	8.00	186		
0.20	8.02	115	74.1	1.28
0.25	8.02	142	74.1	1.28
0.30	8.02	167	74.1	1.28
0.33	8.02	179	74.4	1.29
0.34	8.02	185	74.3	1.29
0.35	8.02	192	74.2	1.29
0.40	8.02	216	74.2	1.29

The results show that the value of κ_{det} has no effect on the accuracy of the randoms rate over a wide range of values. This is due the scaling of the randoms distribution to the measured singles rate. There is also a negligible difference between the FoMs over a wide range of κ_{det} values. In the absence of other criteria, the agreement with the measured trues rate was used to determine the value of κ_{det}; with κ_{det} = 0.34 giving the best agreement. While the value of the trues rate is not a primary figure of merit, smaller differences between calculated and measured trues rates indicate a better overall calculation.

6.3.3 Broad-beam Attenuation Correction Factor

In **Section 5.4.4**, κ_{broad} was initially estimated to be 0.28 for a 350-650 keV energy window, based on physical arguments and the assumption that also κ_{det} = 0.28. However, if the empirically determined value κ_{det} = 0.34 is used, the initial estimate of κ_{broad} becomes 0.38. Empirically-based adjustments were done by measuring the agreement between measured and calculated randoms rates and distributions for different values of κ_{broad}. For this, a study a phantom configuration with significant attenuating material was used (point source at position 6, in water, in **Table 6-1**). The measured and calculated count rates are compared in **Table 6-7,** along with FoMs comparing the measured and calculated randoms distributions.

Table 6-7 Measured and calculated counts rates and FoMs comparing the randoms distributions from an off-centre point source in a water-filled cylinder for different values of κ_{broad}.

κ_{broad}	Randoms Rate (kcps)	Trues Rate (kcps)	MSE	χ^2/N
measured rates, position 6 in H2O	2.00	64.3		
0.20	2.03	69.6	16.0	1.09
0.30	2.02	67.0	15.7	1.09
0.40	2.01	65.2	15.6	1.10
0.45	2.00	64.3	15.6	1.10
0.50	2.00	63.1	15.6	1.11
0.60	1.98	61.1	15.6	1.12
0.70	1.97	59.4	15.7	1.14

The values of κ_{broad} have a very small effect on the accuracy of the randoms rate; the best agreement is for κ_{broad} = 0.45-0.50. The changes are again small because the randoms rate is scaled directly to the measured singles rate. The FoMs also change only slightly with κ_{broad} ; the *MSE* is minimized at

κ_{broad} = 0.40-0.60. The χ^2/N decreases monotonically with the lower values of κ_{broad} and is, therefore, irrelevant. The calculated trues rate also varies slightly, with κ_{broad} = 0.40 giving the best agreement. Since κ_{broad} = 0.45 gives the best agreement for the randoms rate, it is optimal. However, the accuracy of the calculation, as measured by these parameters, is shown to be relatively insensitive to the values of κ_{broad}.

6.3.4 Radioactivity Object Sampling and Calculation Time

The accuracy of the randoms calculation clearly depends on the sampling of the radioactivity object. However, the computation time also depends directly on the number of sample points used. Two calculation parameters, *sampling density* and *threshold*, are used to choose the activity sampling points **(Section 4.2.2)**. The sampling density determines raw number of sample points. The threshold determines which of those points to use in the calculation. It was found that the calculated randoms distributions show little variation if a few hundred to a few thousand sample points are used, depending on the activity distribution. Unsurprisingly, the larger activity distributions require the higher number of points.

In determining the best values for these parameters, the threshold is determined first, and then the sampling density is adjusted to produce the requisite total number of points. The threshold is used to remove points with low activity from the set of sample points to use in the calculation. The high activity points give the greatest contribution to the randoms. The threshold also removes image background, including apparent activity from randoms, scatter and reconstruction artifacts. For objects with highly concentrated activity distributions and high activity, such as the line and point source sources and the cylindrical phantom studies, a high threshold (20%) was used to discriminate low count background. In the line source study, a 20% threshold and a density of 500 points/ml results in ~3000 points. In the point source studies, a 20% threshold and a density of 5000 points/ml results in ~200-300 points. In a uniform cylinder, the large volume greatly increases the number of sample points. For example, a sampling density of 500 pts/ml results in ~70,000 sample points. Therefore, the sampling density was reduced to 50 pts/ml, which generated ~ 7,000 sample points.

Improper use of the threshold may cause problems for complex radioactivity distributions. For example, the contrast phantoms consist of a hot sphere inside a colder cylinder. The contrast difference between the sphere and the cylinder affects the appropriate threshold. A 20% threshold has no effect if the activity ratio is of 2:1. However, this threshold would eliminate the entire contribution of the cylinder if the activity ratio is > 5:1. Therefore, to detect a higher dynamic range of contrast, the threshold was reduced to 5% of the maximum and the density was kept to 50 pts/ml. For both contrast phantoms, this resulted in ~6000 sample points. Since the animal studies had a complex activity distribution, we used a threshold of 5% and a sampling density of 50 pts/ml.

The appropriate threshold also depends on the noise in the reconstructed radioactivity image. One study using a contrast phantom was binned into a 30 second frame. The resulting reconstructed activity image was very noisy. A threshold of 5% was inappropriate because it produced a significant number of sample points outside the subject. For this study, the threshold of the randoms calculation was increased to 20%. This problem was detected by viewing the distribution of sample points before the randoms calculation. However, for routine randoms correction of animal studies, a threshold of 5% and density of 50 pts/ml were expected to work well.

The computation times scale with the number of points. For a standard single processor computer using the standard calculation parameters, the average calculation time was found to be 0.23 seconds/sample point. Thus, for a point source with 250 points, the computation time is 58 seconds. For 7000 sample points, this becomes ~27 minutes. However, this parameter and the calculation code could be further optimized for calculation speed. As well, the code is amenable to parallel processing.

6.3.5 Standard Calculation Parameters

Therefore, the following values for the calculation parameters were used for all the studies, except where otherwise noted.

- detection efficiency correction factor, $\varkappa_{det} = 0.34$,
- photon survival scatter correction factor, $\varkappa_{broad} = 0.45$, and
- for the validation tests, the thresholds and sampling densities were adjusted according to the study: For point sources 5000 pts/ml, 20% threshold, line sources 500 pts/ml, 20% threshold; uniform cylinders 50 pts/ml, 20% threshold and contrast phantoms and animal studies, 50 pts/ml, 5% threshold.

6.4 Results

6.4.1 High Count Study Using a High Activity Line Source in Air

The results from the off-centre line source in air are listed in **Table 6-8.** The total measured delays in the 12 hour frame are far greater than those that would be obtained in a realistic animal study (*c.f.* 5.9 Mcts in the 3 hour mice study). This frame is to test for small biases between the calculated and measured randoms distributions.

At all count rates, the randoms calculation reproduces the measured randoms rates for the line source to within $\leq$ 0.8%. The 12-hour frame is the only data set that shows any significant disagreement, 5.7%, and this was caused by errors in the calculated dead-time correction due to the long scan duration. For the remainder of this analysis, the calculated randoms distributions for this data set only are scaled to the same counts as the measured randoms for comparison purposes. The trues rates, while not relevant to the accuracy of the randoms calculation, are also reproduced to $\leq$ 2.2% for all the time frames except the 12 hour frame, where the error in the trues rate is 7.5%.

Table 6-8 Measured (calculated) count rates from high radioactivity line source at one hour time intervals over a 12 hour scan.

Study/ Start Time	Total Delays (cts)	Singles (kcps)	Trues (kcps)	Randoms (kcps)	Randoms % diff	Randoms Fraction (%)
12 hour frame	459.4 M	2011 (2011)	139 (150)	10.6 (11.2)	-5.7	7
frame 0 t=0 min	266.5 M	7880 (7880)	573 (579)	74.0 (74.6)	-0.8	11
frame 1 t=60 min	127.0 M	5399 (5399)	395 (397)	35.3 (35.4)	-0.3	8
frame 2 t=120 min	60.5 M	3709 (3709)	272 (277)	16.8 (16.8)	0.0	6
frame 3 t=180 min	28.8 M	2554 (2554)	186 (185)	8.00 (8.03)	-0.4	4
frame 4 t=240 min	13.8 M	1763 (1763)	128 (128)	3.83 (3.84)	-0.3	3
frame 5 t=300 min	6.66 M	1223 (1223)	87.6 (89.1)	1.85 (1.86)	-0.5	2
frame 6 t=360 min	3.25 M	853 (853)	60.0 (60.1)	0.903 (0.906)	-0.3	1
frame 7 t=420 min	1.62 M	600 (600)	41.1 (41.2)	0.449 (0.450)	-0.2	1
frame 8 t=480 min	821 k	426 (426)	28.2 (28.3)	0.228 (0.228)	0.0	1
frame 9 t=540 min	429 k	307 (307)	19.3 (18.8)	0.119 (0.119)	0.0	1
frame 10 t=600 min	234 k	226 (226)	13.2 (13.1)	0.0650 (0.0652)	-0.3	0
frame 11 t=660 min	135 k	171 (171)	9.04 (9.16)	0.0375 (0.0374)	0.3	0

The measured 12 hour frame was used first for comparison because of the high number of counts. The SSRB rebinned randoms distributions were examined first. The measured, calculated and percent difference sinograms of two slices are shown: the central slice (**Figure 6-11),** and a slice midway between the axial centre and the axial end (**Figure 6-12).**

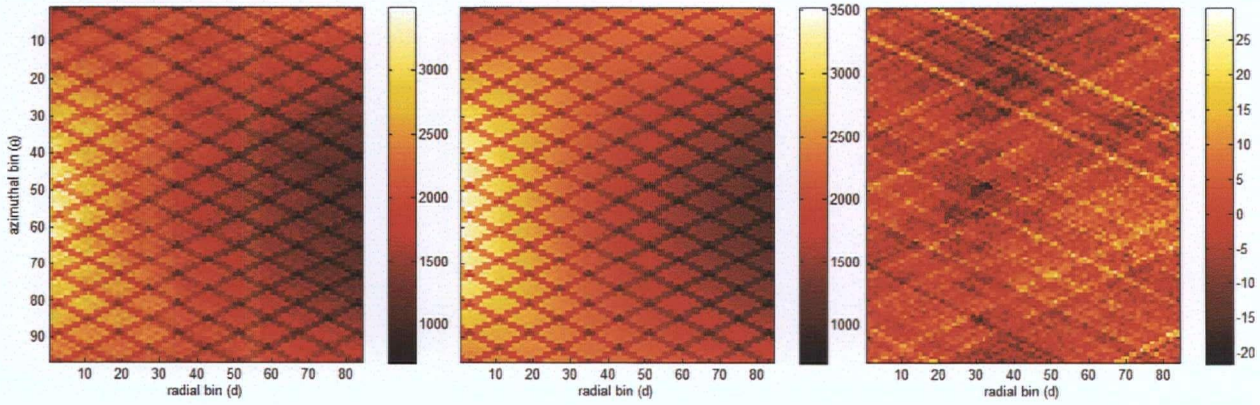

Figure 6-11 The measured (left), calculated (centre) and percent difference (right) central slice randoms sinograms for the 12 hour frame of the off-centre line source study.

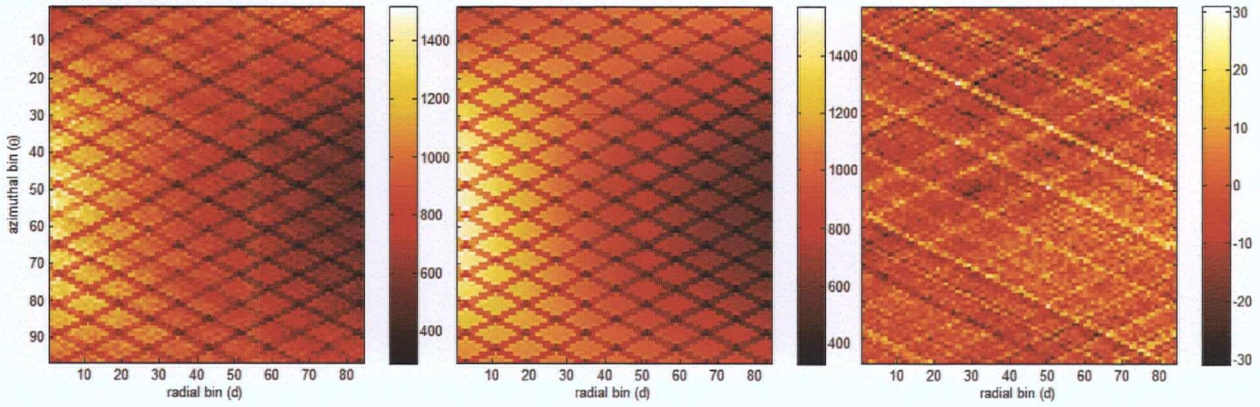

Figure 6-12 The measured (left), calculated (centre) and percent difference (right) sinograms of a slice midway between the centre and the axial end (slice 48) for the 12 hour frame of the off-centre line source study.

Both sets of randoms sinograms show the low frequency spatial variations due to smooth changes in the singles distribution caused by the off-centre source. The high frequency structure caused by the systematic variations in the detector efficiencies within the block is also apparent. Both of these features appear well reproduced by the calculation.

There are some minor differences in the low and high frequency structures, as seen in the percent difference sinograms. The most prominent features are diagonal lines caused by differences in the efficiencies of individual crystals. The lines are most prominent for the lowest count regions where the percent difference values would be the highest. Also visible in the central slice percent difference sinogram is a curved band caused by reduced counts in the measured sinogram. This dip is seen in the pixels that corresponds to the pixels in trues sinograms with the highest count rates. This feature is not seen in all slices; it is not apparent, for example, in the non-central slice in **Figure 6-12.**

The radial, azimuthal and axial profiles of the SSRB rebinned randoms sinograms are shown in **Figure 6-13** to **Figure 6-15**. These are a sample set of profiles in which the other data axes have *not* been summed. The calculated profiles show good agreement with the measured data. A few radial profiles show small differences at some radial positions. The positions of these biases mainly correspond to the location of the curved band artifact described above. Some of the axial profiles show errors where shapes of the profiles agree but are not scaled the same. These are probably caused by the random variations in individual detector efficiencies.

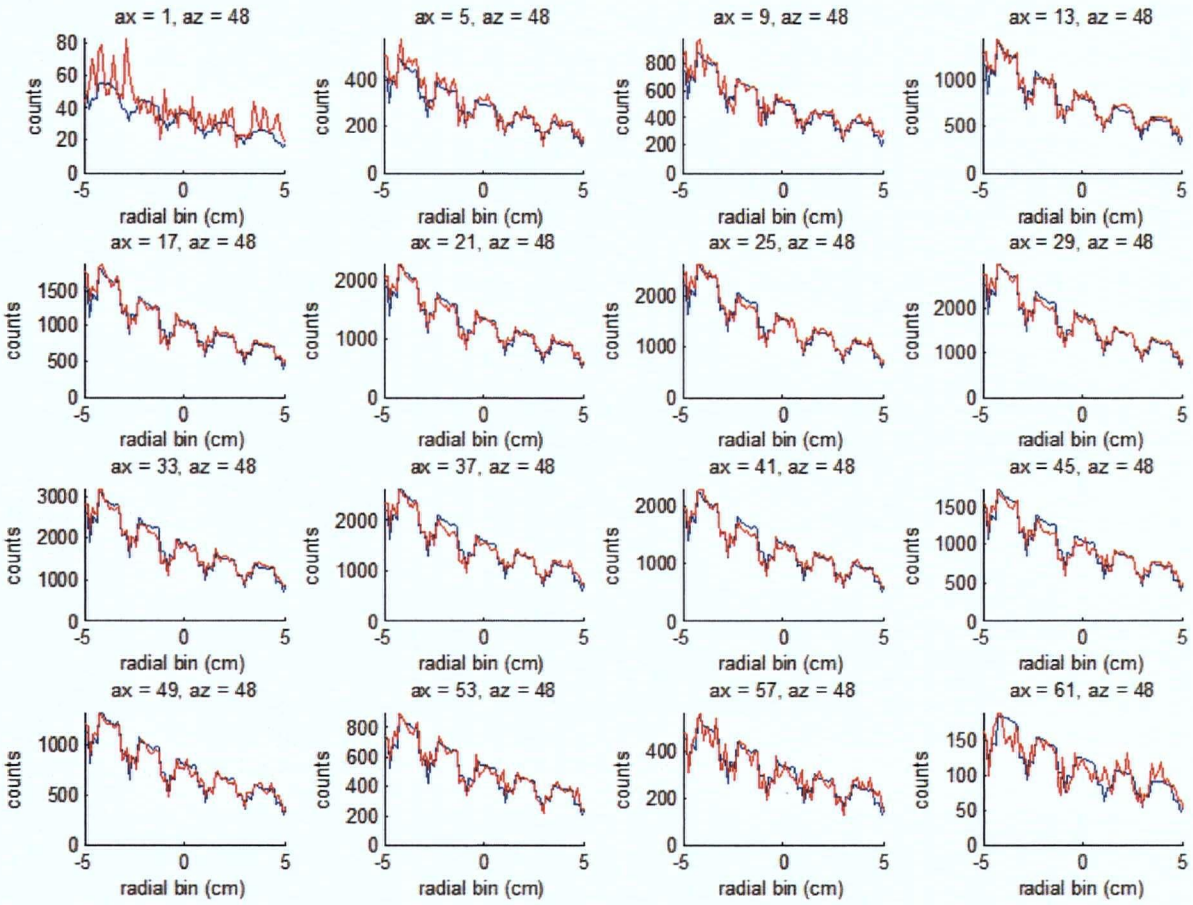

Figure 6-13 Radial profiles for azimuthal bin ("az") 48 and different axial slices ("ax")of the measured (red) and calculated (blue) randoms sinograms of the 12 hour frame of the off-centre line source study.

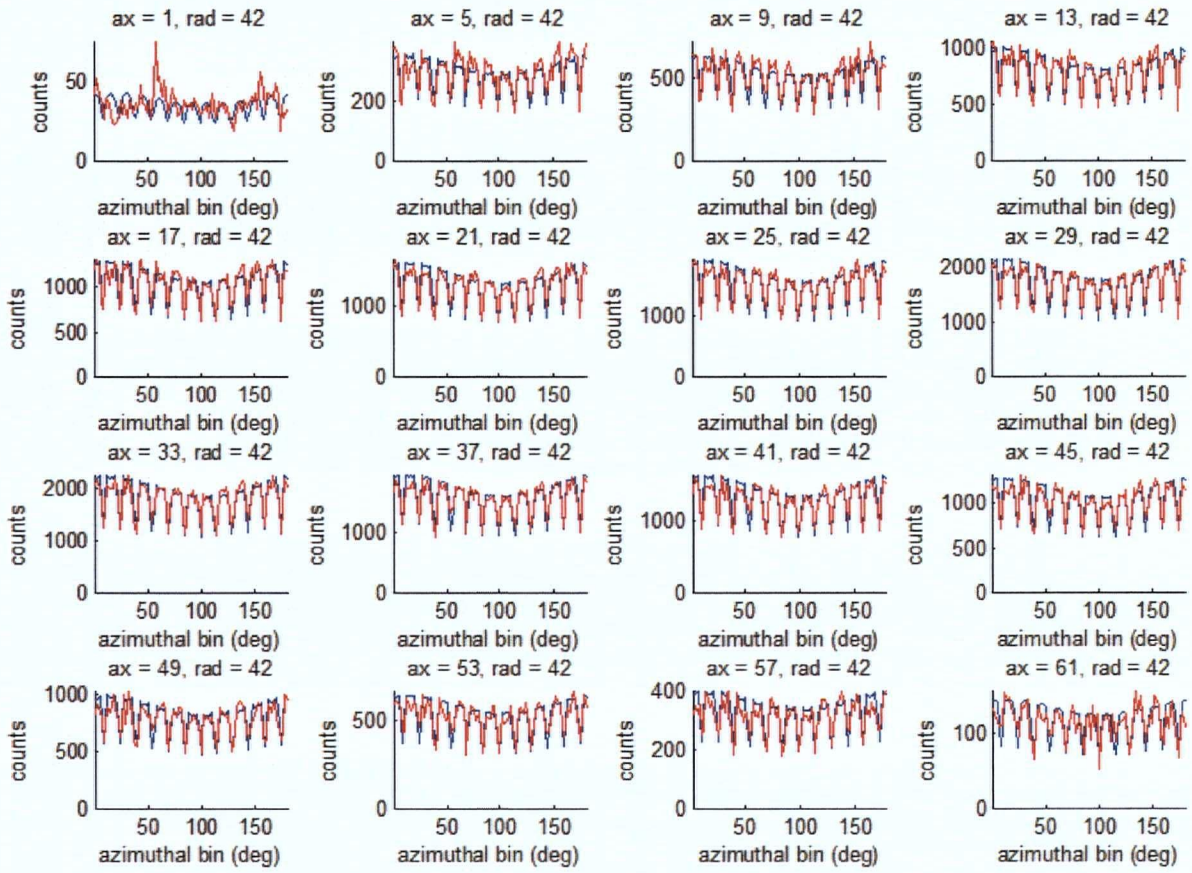

Figure 6-14 Azimuthal profiles for radial bin ("rad") 42 and different axial bins ("ax")of the measured (red) and calculated (blue) randoms sinograms of the 12 hour frame of the off-centre line source study.

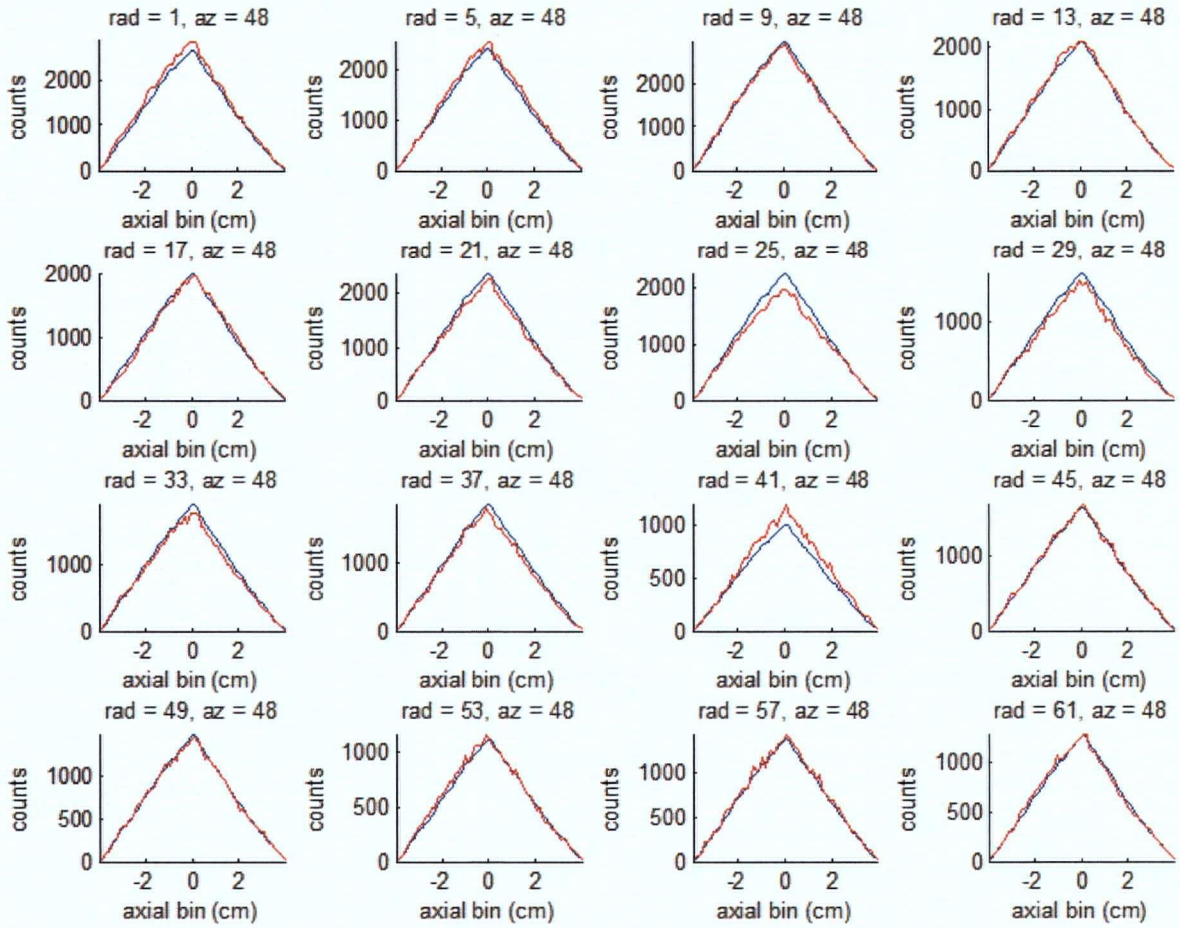

Figure 6-15 Axial profiles for azimuthal bin ("az") 48 and different radial bins ("rad") of the measured (red) and calculated (blue) randoms sinograms of the 12 hour frame of the off-centre line source study.

Figure 6-16 shows the radial, azimuthal and axial summed *count profiles*. These show excellent agreement between the calculated and randoms distributions. **Figure 6-17** shows the radial, azimuthal and axial summed *percent difference profiles* of the same data. These profiles would be flat with a value of 0% if the measured and calculated randoms distributions were in perfect agreement. Again, the data show good agreement with the largest difference seen in the summed radial profile. Here the calculation overestimates the randoms by up to 2-3% in the region that

corresponds to the dip in the measured sinograms. The azimuthal and axial profiles are nearly flat distribution, with only a minor bias in the axial direction. Comparing **Figure 6-17** with **Figure 6-16** shows that, in the axial distribution, the counts decrease significantly near the axial edges. Thus, a larger percent difference near the axial edge actually represents a very small difference in the distributions.

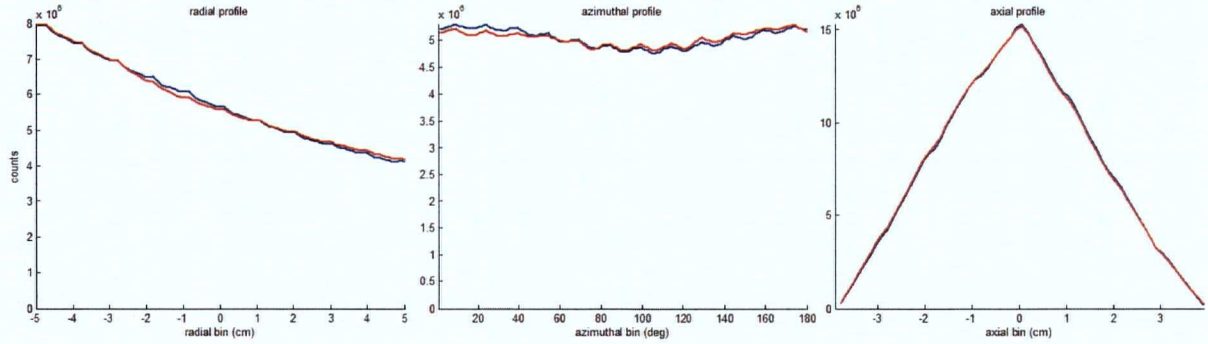

Figure 6-16 The radial (left), azimuthal (centre) and axial (right) summed count profiles of the calculated (blue) and measured (red) randoms distributions from the 12 hour frame of the off-centre line source.

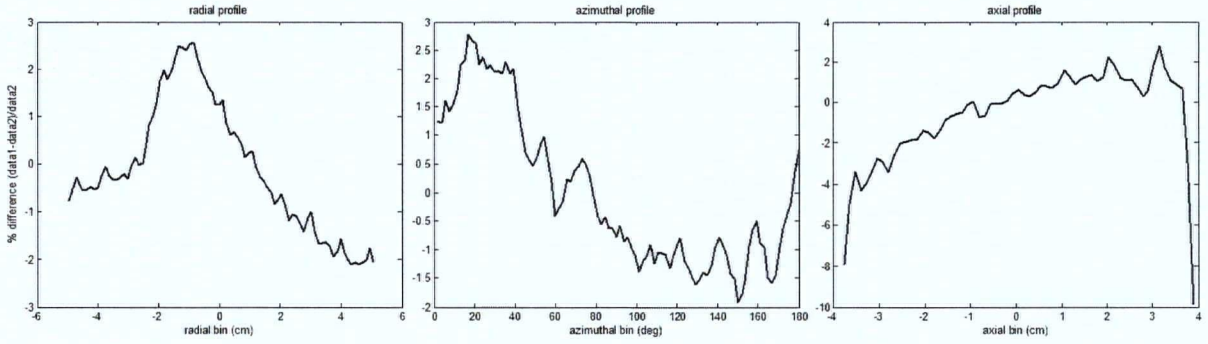

Figure 6-17 The radial (left), azimuthal (centre) and axial (right) summed percent difference (data1 = calculated, data2 = measured) profiles for the 12 hour frame of the randoms distributions of the off-centre line source.

A sample of the 3D data set was also examined. The radial count profiles of the randoms sinograms for different segments are shown in **Figure 6-18** to **Figure** 6-20**.** Again, the calculated profiles appear to agree well with the measured ones. At large oblique angles (segments ±7), there is a small anti-symmetric discrepancy in the scaling, as seen when the radial profiles are summed

over the other axes, as shown in **Figure 6-21**. These are only a small contribution to the overall randoms distributions.

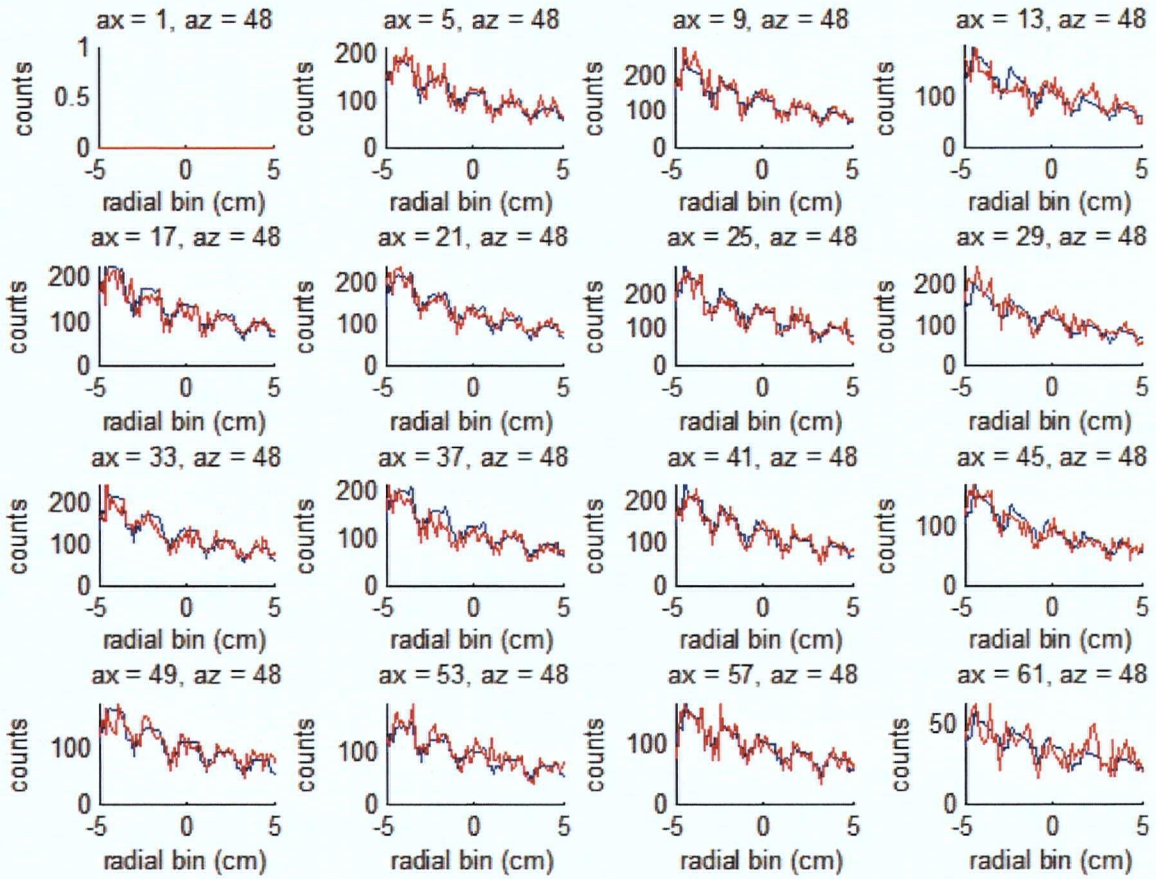

Figure 6-18 Radial profiles of the direct planes (segment 0) of the measured (red) and calculated (blue) radial profiles for azimuthal bin ("az") 48 and different axial slices ("ax"). Some profiles are missing because those oblique sinograms are not sampled in this segment.

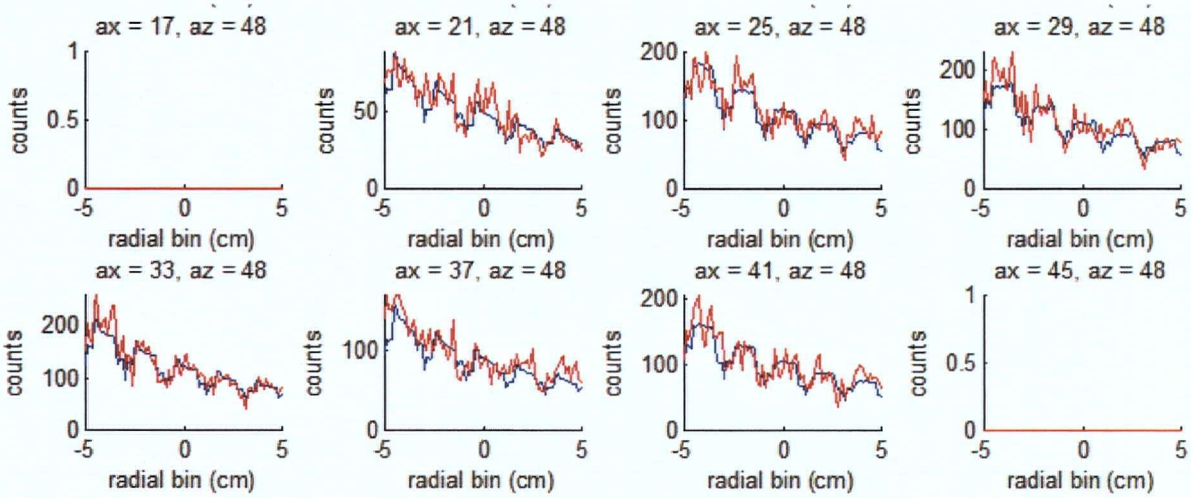

Figure 6-19 Radial profiles of the oblique planes (segment -7) of the measured (red) and calculated (blue) radial profiles for azimuthal bin ("az") 48 and different axial slices ("ax"). Some profiles are missing because those oblique sinograms are not sampled in this segment.

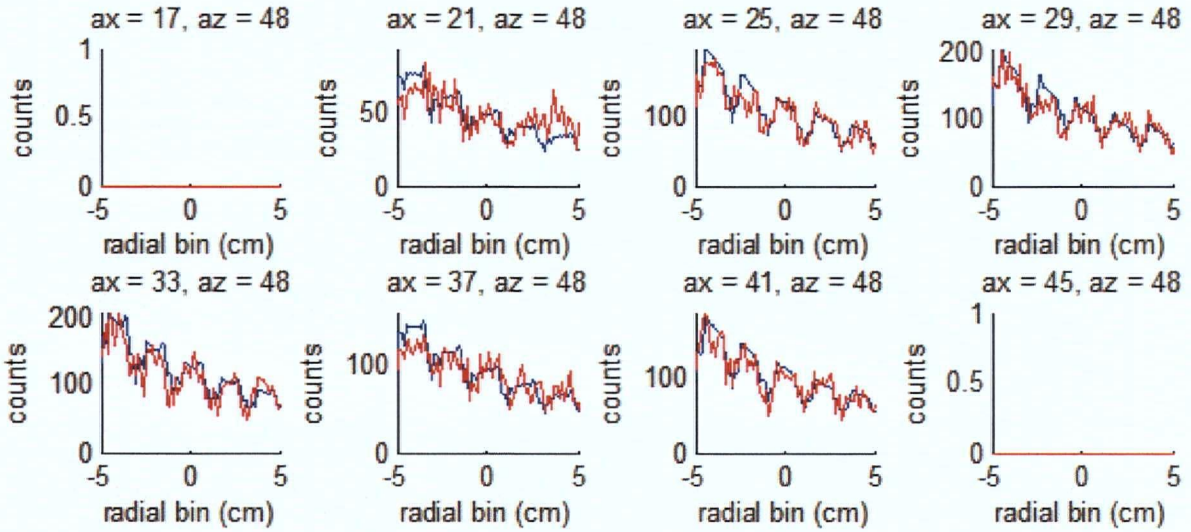

Figure 6-20 Radial profiles of the oblique planes (segment +7) of the measured (red) and calculated (blue) radial profiles for azimuthal bin ("az") 48 and different axial slices ("ax"). Some profiles are missing because those oblique sinograms are not sampled in this segment.

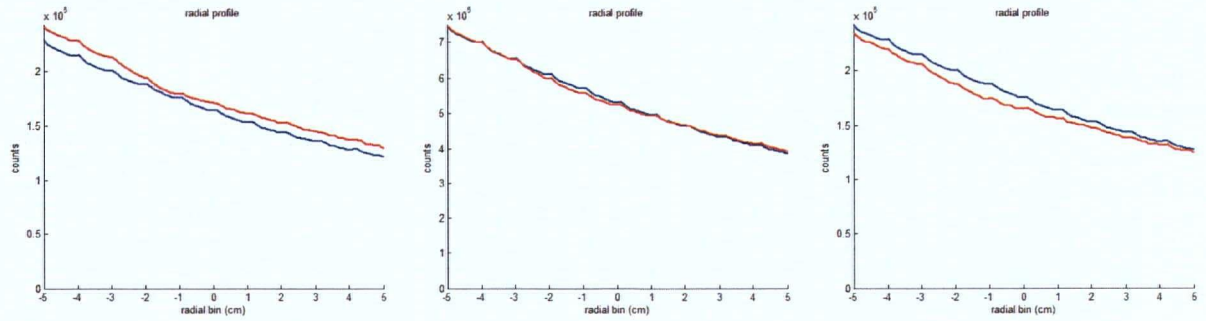

Figure 6-21 The radial summed count profiles of the measured (red) and calculated (blue) randoms distributions for segments -7 (left), 0 (centre) and +7 (right).

Quantitative figures of merit were calculated for the different time frames in this study, and the results are listed in **Table 6-9**. The main difference between the frames is the image noise. The first frames have a high number of counts, and, therefore, less image noise. For these frames, $\chi^2/N > 1$, which indicates that differences in the pixels values are non-Poisson and, therefore, due mainly to biases. Thus, the other FoMs indicate the magnitude of the biases; higher count frames give better estimates. Therefore, the low values of the *NMSE* and the very high value of the 2D correlation coefficient in the 12 hour frame suggests that the overall bias is very small. The 2D correlation coefficient is very high in the four highest count frames and does not change significantly between these frames. As the total counts decrease, the statistical fluctuations begin to dominate and the correlation decreases.

Table 6-9 FoMs comparing the measured and calculated randoms distributions from the high radioactivity line source at one hour time intervals over the 12 hour scan. The values are for the central slice sinograms. In brackets are the FoMs over all the pixels in the data set.

Study/ Start Time	Total Delays (cts)	*NMSE (%)*	*s.d (%diff)* (%)	χ^2/N	r_{2D} (%)
12 hour frame	459.4 M	0.36 (1.09)	3.7	5.85 (4.50)	98.0
frame 0 t=0 min	266.5 M	0.45 (1.55)	4.2	4.55 (3.39)	97.6
frame 1 t=60 min	127.0 M	0.56 (2.29)	4.6	2.54 (2.14)	96.9
frame 2 t=120 min	60.5 M	0.81 (3.79)	5.6	1.76 (1.55)	95.5
frame 3 t=180 min	28.8 M	1.31 (6.90)	7.1	1.36 (1.29)	92.6
frame 4 t=240 min	13.8 M	2.38 (13.3)	9.3	1.18 (1.15)	87.5
frame 5 t=300 min	6.66 M	4.71 (26.1)	13.4	1.13 (1.09)	78.3
frame 6 t=360 min	3.25 M	13.3 (50.8)	18.1	1.05 (1.05)	67.1
frame 7 t=420 min	1.62 M	17.2 (99.5)	25.4	1.02 (1.03)	53.5
frame 8 t=480 min	821 k	33.4 (188.7)	35.4	1.00 (1.02)	41.0
frame 9 t=540 min	429 k	63.6 (341.4)	48.7	1.01 (1.00)	29.4
frame 10 t=600 min	234 k	112.8 (586.7)	65.4	0.99 (1.00)	21.5
frame 11 t=660 min	135 k	192.3 (953.9)	73.0	0.98 (0.99)	14.9

However, the FoMs still have a contribution from noise. The *sd(%diff)* reflects the noise in the measured sinograms. In the measured central slice randoms sinogram of the 12 hour frame (**Figure 6-11),** the counts in most pixels range between 1500-3500, except in the areas reduced by

block structure. The lower count regions contribute more to the total image noise. From this perspective the dominant pixel value was 1500 counts, which corresponds to ~2.6% noise. This is close to the value of *sd(%diff)* = 3.7% calculated from the differences in the sinogram pixel values.

For those frames where $\chi^2/N \approx 1$ (frames ≥ 6), the difference between the calculated and measured data is dominated by the Poisson noise. Any biases are smaller than the statistical noise and is, thus, not detectable by the FOMs. This is illustrated in **Figure 6-22**, which shows the measured and calculated randoms for the central slice sinogram in time frame 6. The measured sinogram is very noisy with little visible structure, but the calculated sinogram is still smooth. The percent difference sinogram shows only noise, with no evidence of a bias. The noisy measured sinogram results in the high values of percent difference.

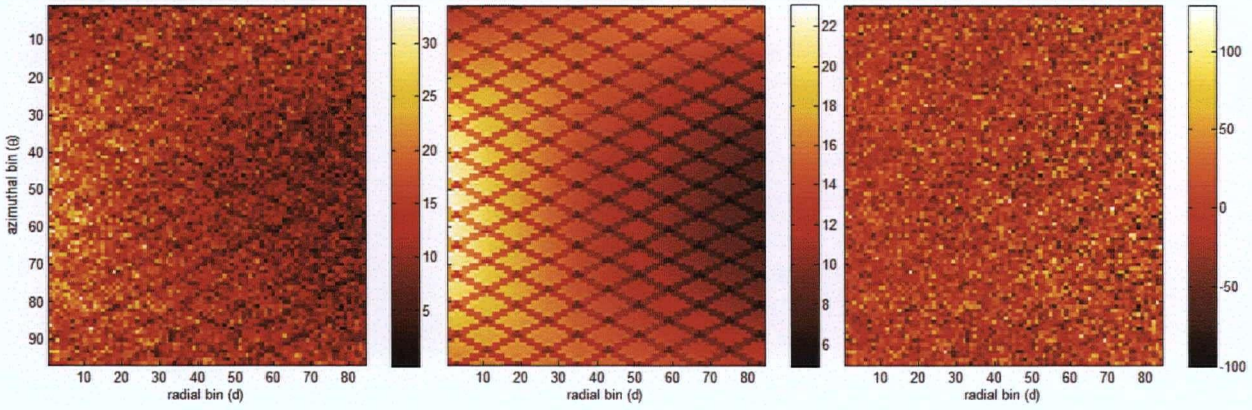

Figure 6-22 The measured (left), calculated (centre) and % diff (right) central slice randoms sinograms for frame 6. The reduced counts in the measured sinogram greatly increase the noise.

The FoM values from comparing the pixels in all the slices (in brackets) show the same systematic changes as those for the central slice. However, the values are slightly higher, due mainly to the increased noise from the other slices where the counting sensitivity is lower. This is confirmed by the reduced χ^2/N when comparing the pixels in all the slices.

The FoMs of the individual slices of the 12 hour frame were also calculated to examine their variations between slices in a high count study. **Figure 6-23** shows the values of the *NMSE* and *sd(%diff)* per slice. The *NMSE* remains flat out to nearly the axial ends on the tomograph which indicates that the values of *NMSE* are dominated by the bias and not the image noise. The *sd(%diff)* is not flat because it changes with the increasing noise in the measured slices towards the axial edge which is caused by the nearly triangular nature of the sensitivity profile, as seen in the axial count profiles (e.g. **Figure 6-16**).

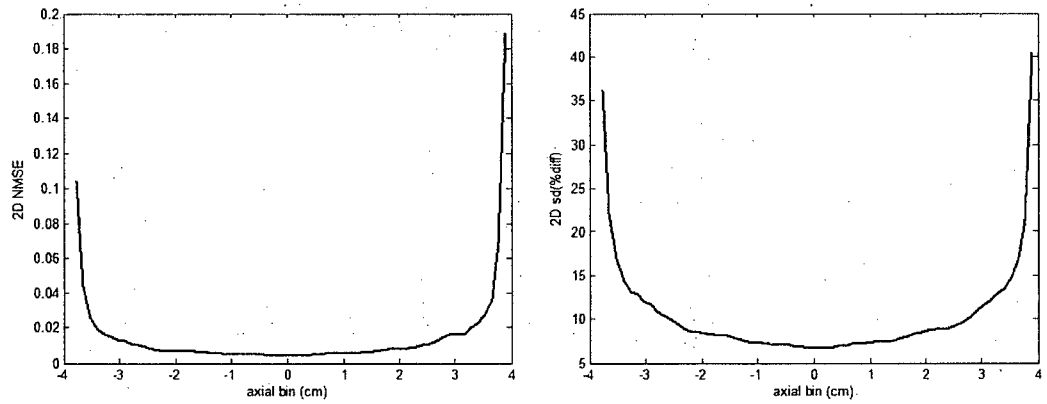

Figure 6-23 The NMSE (left) and sd(% diff) (right) per slice for the 12 hour frame. The values for *NMSE* and *sd(%diff)* are different than those in Table 6-9 because, in the profiles, the calculated data is used in the denominator of (6.3)and (6.5) to avoid "divide-by-zero" errors in the profiles.

Figure 6-24 shows the values of the χ^2/N and the 2D correlation coefficient per slice. Again, $\chi^2/N > 1$ signifies that the differences between the measured and calculated are not purely Poisson. The χ^2/N peaks in the slice containing the most counts, where the Poisson noise is least significant. The 2D correlation coefficient shows an excellent correlation for the majority of the slices, dropping off only at the edges where the noise begins to dominate.

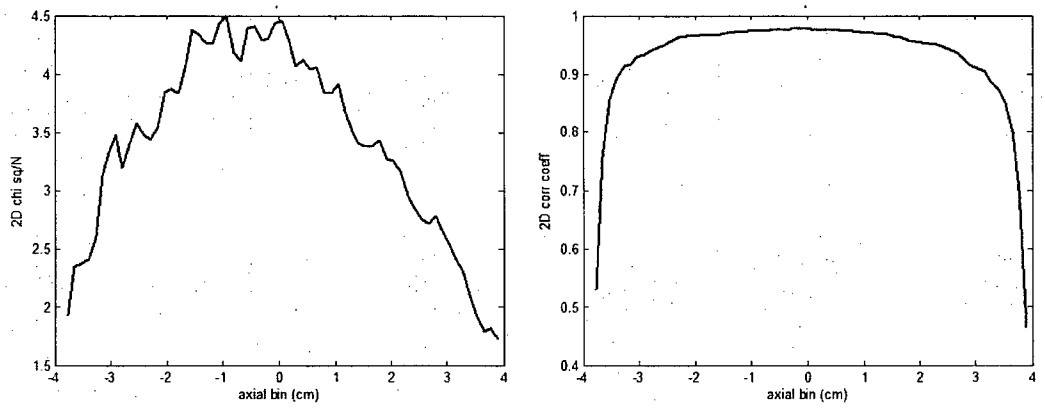

Figure 6-24 The χ^2/N (left) and 2D correlation coefficients (right) per slice for the 12 hour frame. The values for χ^2/N are different than those in Table 6-9 because, in the profiles, the calculated data is used in the denominator of (6.4) to avoid "divide-by-zero" errors in the profiles.

The effect of count rate on the randoms distribution was examined by comparing the measured randoms distributions from two different time frames. **Figure 6-25** shows the radial and axial percent difference profiles comparing the randoms distributions measured at high count rates (frame 0) with those measured at low count rates (frame 11). The source was not moved between these time frames; thus, only the acquisition count rates and the total collected counts are different. The total counts in the low count rate frame were scaled to those in the high count rate frame for comparison. There are obvious large biases in the radial and axial distributions, seen as large slopes, caused by the differences in the count rates during acquisition.

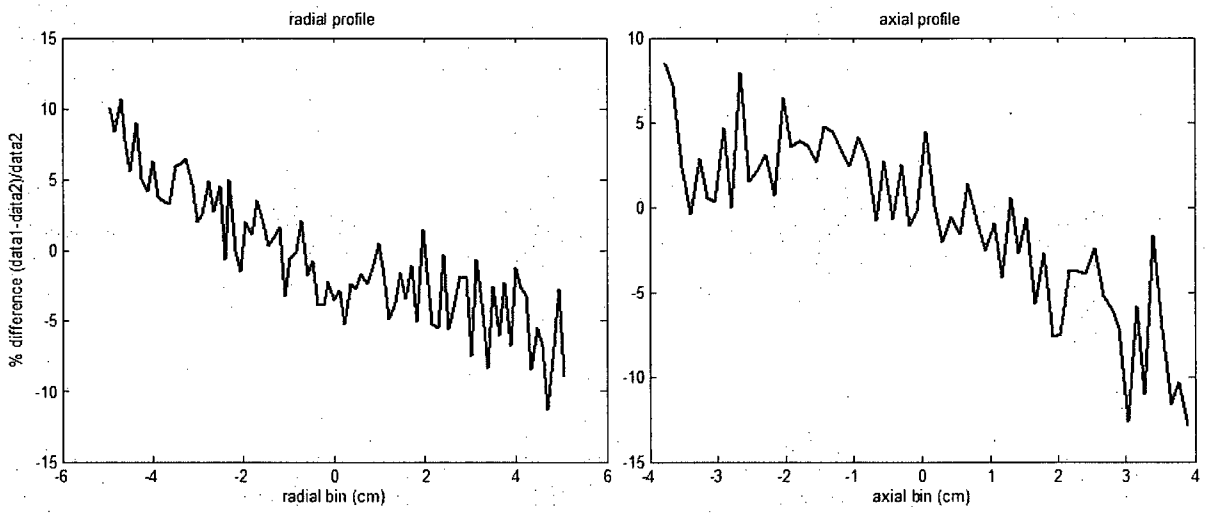

Figure 6-25 The radial (left) and axial (right) randoms summed percent difference profiles where data1 = measured frame 0, and data2 = measured frame 11. The counts in frame 11 were scaled to those in frame 0.

The most likely cause of this bias is the LSO background radioactivity activity (**Section 4.7.4**, [103]). At low count rates, the randoms caused by singles events *inside* the detectors have a significant contribution to the measured randoms.

The randoms calculation was then tested to determine if it could reproduce the randoms distributions at both high and low count rates. **Figure 6-26** shows the radial and axial summed percent difference profiles between measured and calculated distributions for both time frames 0 and 11. The biases seen in these profiles are much smaller than the differences between measured time frames 0 and 11 seen in **Figure 6-25**, especially in the radial direction. Thus, the randoms calculation is able to reproduce the effects of different acquisition count rates, probably because it takes the background radioactivity into account.

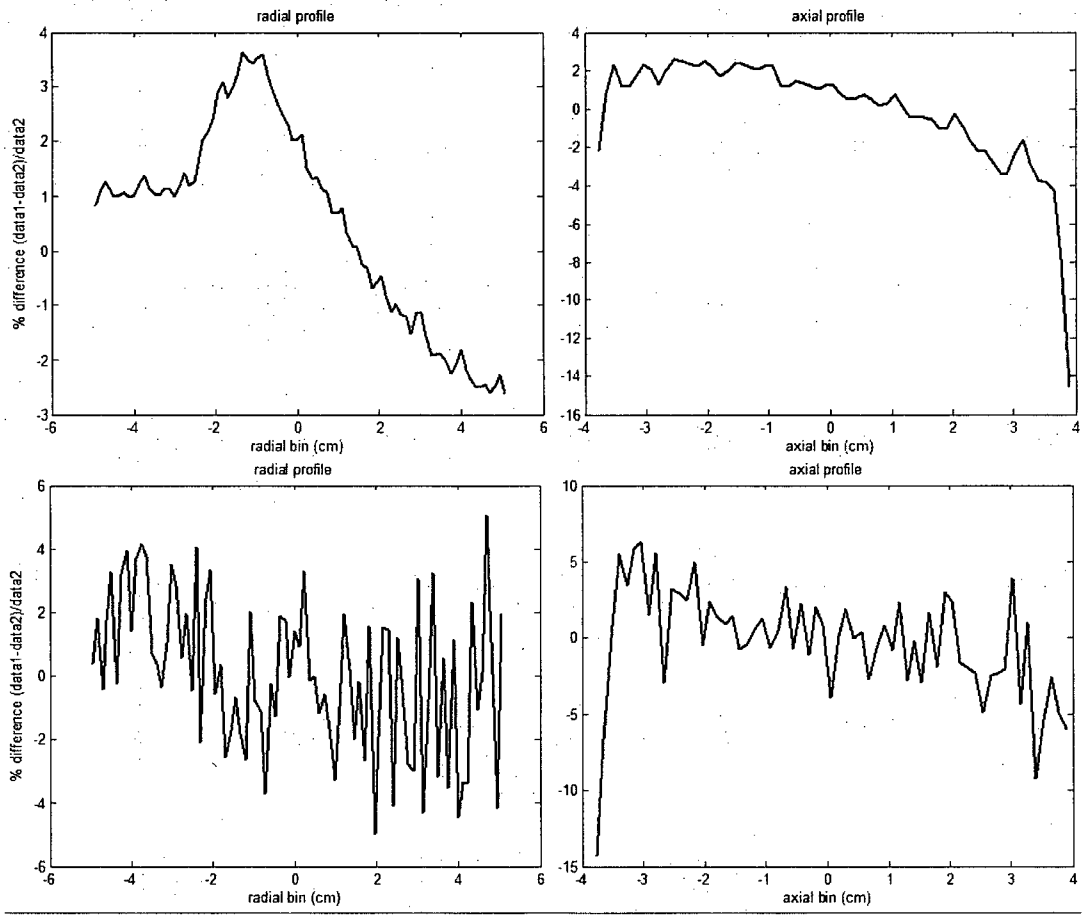

Figure 6-26 The radial (left) and axial (right) randoms summed percent difference profiles where data1 = calculated and data2 = measured randoms. The top row shows the profiles for frame 0 (high rates) and the bottom row shows the profiles for frame 11 (low rates).

6.4.2 Point Sources in Air and Water-filled cylinders

The results from the studies of point sources at various positions in air-filled and water-filled cylinders are listed in **Table 6-10**.

Table 6-10 Measured and calculated count rates from a high radioactivity point source in an air-filled and water-filled cylinder at various positions.

Point position measured (calculated)	Total Delays (Mcts)	Singles (kcps)	Trues (kcps)	Delays (kcps)	Delays % diff	Randoms Fraction (%)
1 (water)	87.8	6200 (6200)	487 (542)	48.8 (48.6)	-0.4	9.1
1 (air)	51.0	4713 (4713)	458 (473)	28.4 (28.5)	-0.4	5.8
2 (water)	26.4	2504 (2504)	199 (209)	7.34 (7.24)	1.4	3.6
2 (air)	4.62	1023 (1023)	97.0 (96.6)	1.28 (1.27)	0.8	1.3
5 (water)	53.1	4793 (4793)	232 (236)	29.5 (29.3)	0.7	11.3
5 (air)	34.2	2704 (2704)	153 (150)	9.51 (9.61)	-0.3	5.9
6 (water)	7.20	1284 (1284)	64.3 (64.4)	2.00 (2.00)	0.0	3.0
6 (air)	1.88	646 (646)	36.4 (36.1)	0.52 (0.52)	0.0	1.4
7 (water)	17.8	2744 (2744)	49.5 (33.9)	9.87 (9.81)	0.6	16.6
7 (air)	11.1	2166 (2166)	39.0 (33.8)	6.16 (6.14)	0.3	13.6
8 (water)	5.77	1144 (1144)	22.6 (17.3)	1.64 (1.64)	0.0	6.8
8 (air)	2.41	721 (721)	13.1 (11.5)	0.67 (0.67)	0.0	4.9
complex point 1	1.99	936 (936)	90.8 (91.9)	1.11 (1.11)	0.0	1.2
complex point 2	4.32	1379 (1379)	116 (124)	2.40 (2.40)	0.0	2.0

The calculation reproduces the measured delays rates to within $\leq$ 1.4% for all point source positions, for both air- and water-filled cylinders. The accuracy of the calculated randoms rates is independent of the point source location. The calculated trues rates do not accurately reproduce

the measured rates, with errors ranging from <1% to 32%, with the largest error for points in water near the axial edge. Again, this has no bearing on the accuracy of the randoms.

The measured and calculated central slice randoms sinograms for the point source at position 1 in the water-filled and air-filled cylinders are compared, respectively, in **Figure 6-27** and **Figure 6-28**. Both show good visual agreement with the block structure and low frequency variations in the randoms, but the calculated distributions are smooth. The percent difference sinograms again show the diagonal lines due to random variations in crystal efficiencies and the artifact from the dip in the measured randoms, most clearly seen in the measured sinogram of the point source in air.

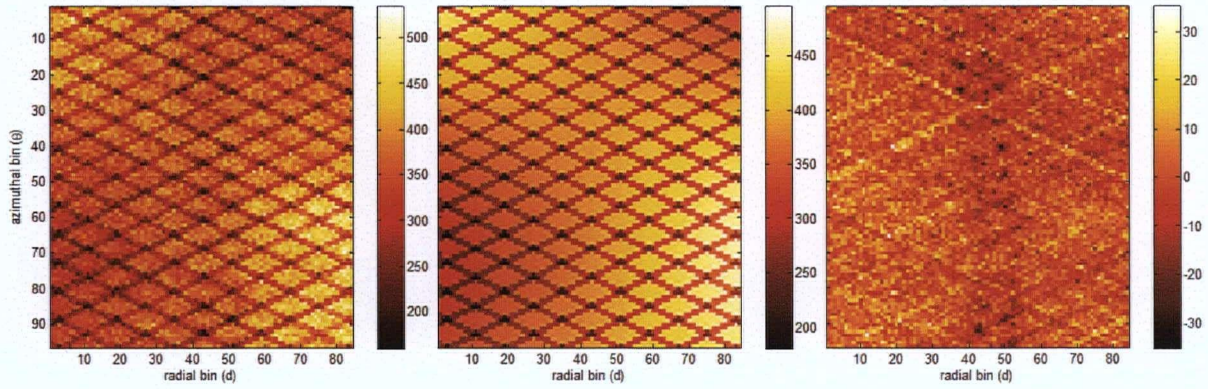

Figure 6-27 Measured (left), calculated (center) and percent difference (right) randoms sinograms for the central slice of the scan of the point source in water at position 1.

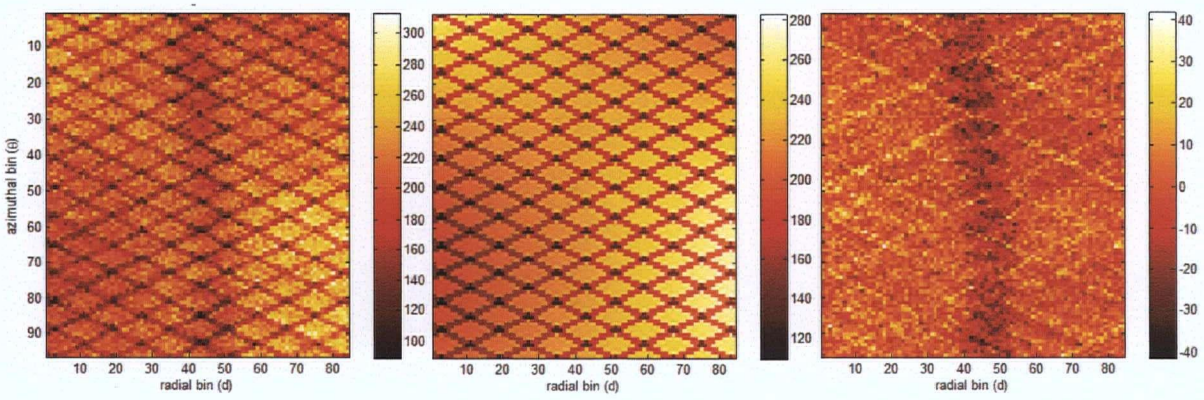

Figure 6-28 Measured (left) calculated (center) and percent difference (right) randoms sinograms for the central slice of the scan of the point source in air at position 1.

Figure 6-29 and **Figure 6-30** show the radial, azimuthal and axial summed percent difference profiles. The results generally show excellent agreement. In the radial summed count profile, the calculation overestimates the randoms in the region that corresponds to the dip in the measured sinograms by up to 5-6%. The azimuthal and axial profiles are nearly flat (if the scale of the y-axis axis is noted).

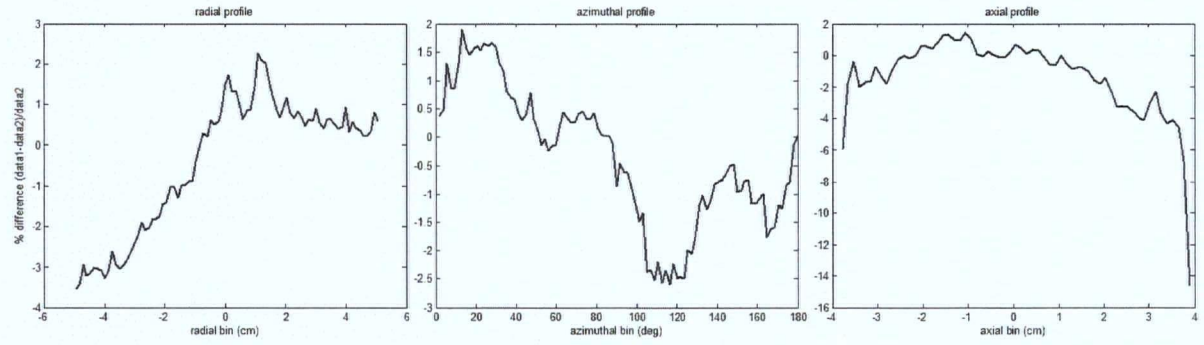

Figure 6-29 The radial (left), azimuthal (centre) and axial (right) summed percent difference (data1 = calculated, data2 = measured) profiles for the randoms distributions of the point source position 1 in water.

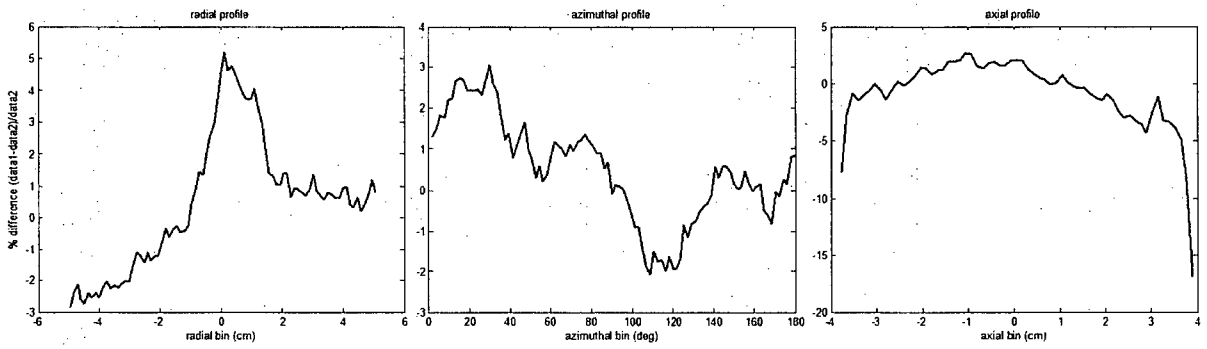

Figure 6-30 The radial (left), azimuthal (centre) and axial (right) summed percent difference (data1 = calculated, data2 = measured) profiles for the randoms distributions of the point source at position 1 in air.

The randoms sinograms for the other point source positions vary considerably in appearance. However, the calculated distributions again show similarly good agreement with the measured ones. Likewise, the summed percent difference profiles for the calculated and measured randoms for all the studies show similar results to those in **Figure 6-29** and **Figure 6-30**. The radial profiles all show a minor systematic bias causing a slight slope. The point sources in air measurements also show the artifact from the dip in the measured randoms. The axial percent difference profiles all show excellent agreement. As well, results from the studies of point sources in complex attenuation phantoms are comparable.

Table 6-11 shows the quantitative figures of merit found when comparing the measured and calculated randoms distributions for the different point source configurations. There are a variety of source configurations and total acquired counts represented in this group of studies. For those studies where $\chi^2/N \approx 1$ (lower counts), the difference between the calculated and measured data is dominated by the Poisson noise and, therefore, the bias is not detectable by the other FoMs. For those studies with $\chi^2/N > 1$ (higher counts), the statistical noise no longer dominates and the FoM become more sensitive to bias. In these studies, the low values of *NMSE* and *sd(%diff)* and the high values of the 2D correlation coefficient indicate that any biases are small.

Table 6-11 FoMs comparing the measured and calculated randoms distributions from the different point source configurations. The values are for the central slice sinograms. In brackets are the FoMs over all the pixels in the data set.

Study position/ configuration	Total Delays (cts)	*NMSE (%)*	*s.d (%diff)* (%)	χ^2/N	r_{2D} (%)
1 (water)	87.8	0.69 (2.93)	5.1	2.25 (1.85)	90.5
1 (air)	51.0	1.09 (4.34)	6.5	2.11 (1.59)	84.3
2 (water)	26.4	1.68 (8.55)	8.1	1.52 (1.37)	93.8
2 (air)	4.62	6.90 (39.51)	16.2	1.13 (1.11)	72.5
5 (water)	53.1	0.85 (4.38)	5.8	1.62 (1.53)	88.4
5 (air)	34.2	1.15 (5.9)	6.8	1.42 (1.35)	85.0
6 (water)	7.20	4.36 (26.42)	12.9	1.10 (1.10)	85.1
6 (air)	1.88	15.45 (87.59)	24.0	1.04 (1.03)	53.8
7 (water)	17.8	2.01 (11.35)	8.8	1.27 (1.22)	67.9
7 (air)	11.1	2.92 (16.79)	10.5	1.17 (1.14)	60.2
8 (water)	5.77	5.39 (32.35)	14.3	1.09 (1.07)	74.0
8 (air)	2.41	12.15 (69.65)	21.3	1.05 (1.03)	50.2

6.4.3 Uniform Cylindrical and Contrast Phantoms

The results from the cylindrical and contrast phantom studies are listed in **Table 6-12**. The calculation was able to reproduce the randoms rate to within ≤1.2%, irrespective of the high activities (and large dead-times) used in some studies. Even with the high activities, the highest randoms fraction achieved was only 15.5%. Increased radioactivity outside the axial FOV also did not affect the accuracy of the calculated randoms rates. However, this is expected because the

randoms are scaled to the measured singles rate; thus, the activity outside the AFOV results in a bias in the distribution rather than an error in the rates. The trues rates, however, are not generally in perfect agreement, and there are large errors with activity outside the AFOV.

Table 6-12 Measured and calculated count rates for cylindrical phantom studies.

Study measured (calculated)	Total Delays (Mcts)	Singles (kcps)	Trues (kcps)	Delays (kcps)	Delays % diff	Randoms Fraction (%)	Activity outside AFOV
lg cyl	30.8	2567 (2567)	138 (149)	8.56 (8.56)	0.0	5.8	-
sm cyl z = 0.0 cm	420	9626 (9626)	638 (663)	117 (118)	-1.2	15.5	0%
sm cyl z = 1.0 cm	82.3	5974 (5974)	419 (435)	45.7 (45.8)	-0.2	9.8	5%
sm cyl z = 2.0 cm	51.9	4727 (4727)	306 (335)	28.8 (28.8)	0.0	8.6	20%
sm cyl z = 3.0 cm	47.3	3167 (3167)	165 (197)	13.2 (13.2)	0.0	7.4	30%
contr phant 1	75.3	4011 (4011)	244 (258)	20.9 (21.0)	-0.5	7.9	-
contr phant 2 study 1	27.5	8651 (8651)	512 (539)	93.4 (93.3)	0.1	15.4	-
contr phant 2 study 2	316	5769 (5769)	337 (359)	43.8 (44.3)	-1.1	11.5	-
contr phant 2a	29.8	2524 (2524)	143 (163)	8.28 (8.26)	0.2	5.5	-

Figure 6-31 shows the radial, azimuthal and axial summed count profiles for the large uniform cylinder. These show excellent agreement between the calculated and randoms distributions. The same data is shown again in the radial, azimuthal and axial summed percent difference profiles in **Figure 6-32**. Here the radial and azimuthal profiles are nearly flat, but the axial profile shows a distinct slope caused by an underestimation of the randoms at the end of the phantom where there is activity outside the AFOV. Although this leads to a relatively large percent difference, the axial count profile (**Figure 6-31, right)** shows that the absolute number of counts near the axial ends is small. Although these are scaled by the sensitivity following reconstruction, the noise due to the

low counts would be much greater than the biases, so there is only a minor impact on the distributions.

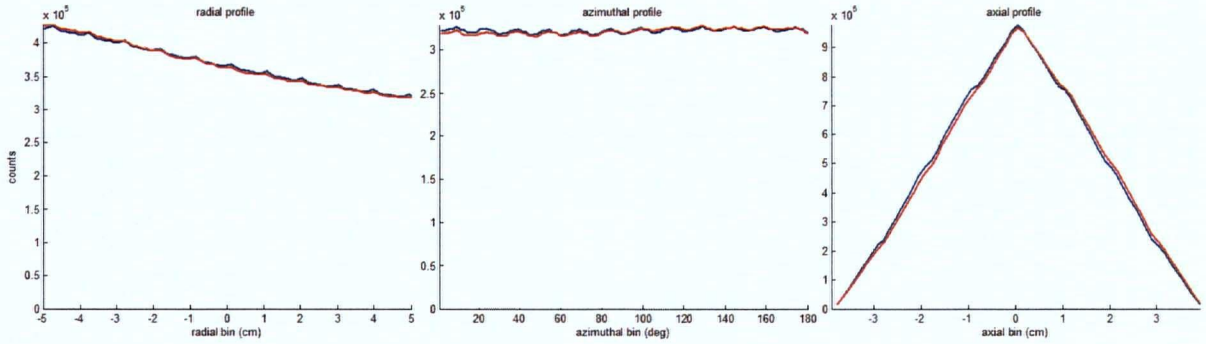

Figure 6-31 The radial (left), azimuthal (centre) and axial (right) summed count profiles of the measured (blue) and calculated (red) randoms distributions from the large uniform cylinder study.

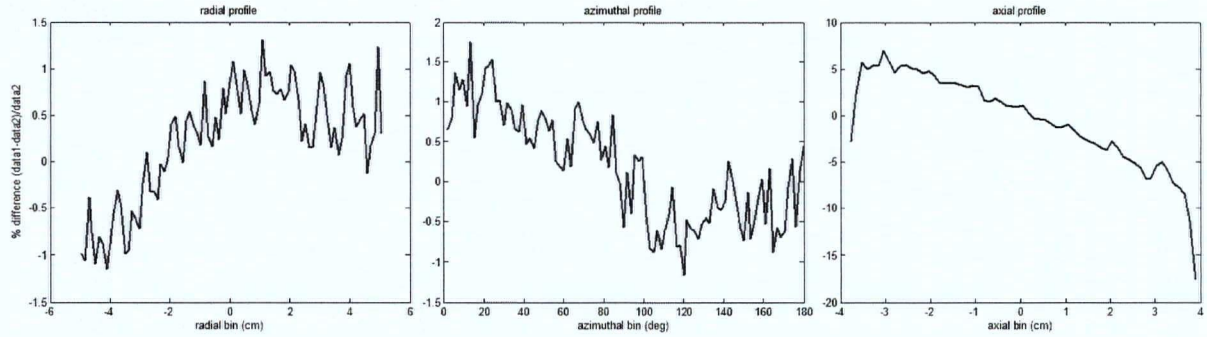

Figure 6-32 The radial (left), azimuthal (centre) and axial (right) summed percent difference (data1 = calculated, data2 = measured) profiles for the large cylindrical phantom.

The effects of activity outside the axial FOV were examined with the small cylinder. **Figure 6-33** shows the measured and calculated axial summed count profiles for the small cylinder in different axial positions. For the cylinder fully in the FOV (0.0 cm displacement), the axial distributions are nearly symmetric and there is good agreement. When the cylinder is displaced by 3.0 cm, 30% of the radioactivity is outside the AFOV. Although this changes the distribution, there is still excellent between the calculated and randoms axial distributions.

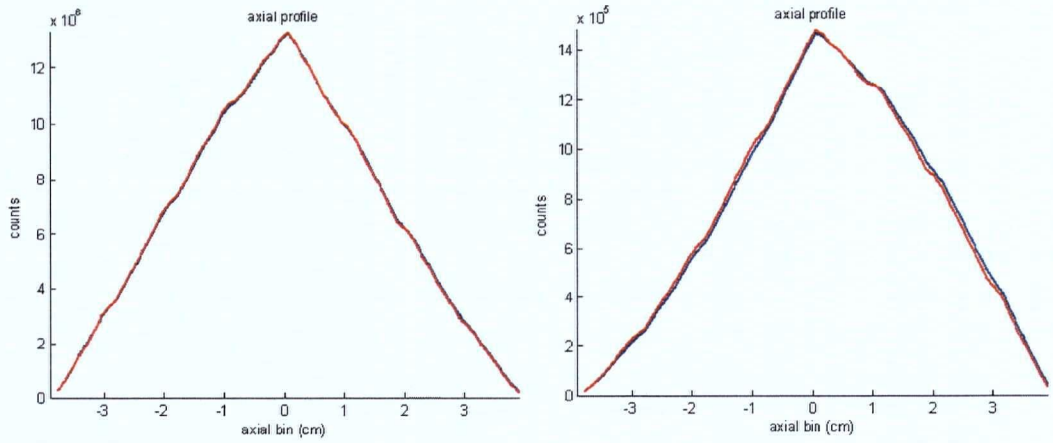

Figure 6-33 The axial summed count profiles of the measured (blue) and calculated (red) randoms distributions for the small uniform cylinder at 0.0 cm (left) and 3.0 cm (right) displacements.

The axial summed percent difference profiles of the same data are shown in **Figure 6-34**. They show the increased bias with greater activity outside the FOV. For the 3.0 cm displacement the error is ~8% at each of the axial ends. However, this percent difference is almost undetectable in the count profile (**Figure 6-33**) because the absolute number of counts is small at the axial ends.

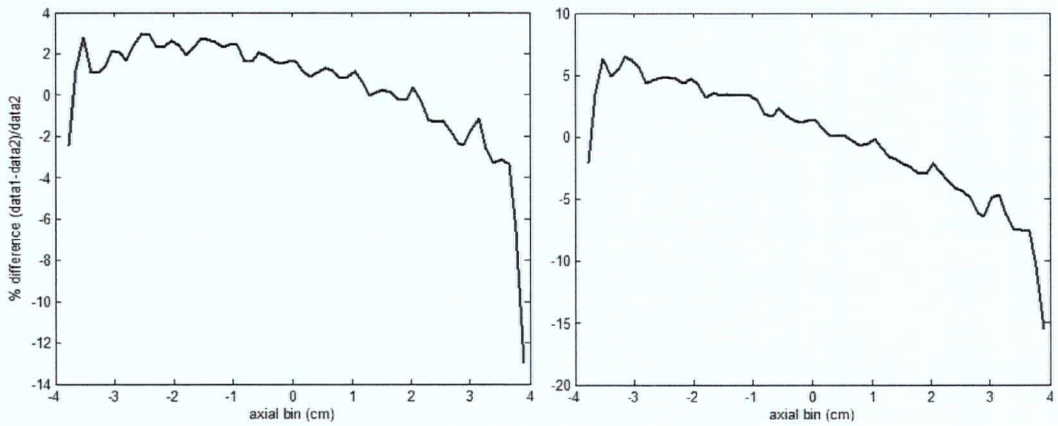

Figure 6-34 The axial summed percent difference profiles of small uniform cylinder at 0.0 cm (left) and 3.0 cm (right) displacements.

The results for the contrast phantoms showed similarly good agreement between calculated and measured randoms distributions. **Figure 6-35** show the radial, azimuthal and axial summed percent difference profiles for contrast phantom 2, study 1. These again show good agreement. The slope seen in some of the axial profiles is indicative of activity outside the FOV. The results from the other contrast phantom studies are similarly good, but also show the bias in the axial profiles due to activity outside the axial FOV.

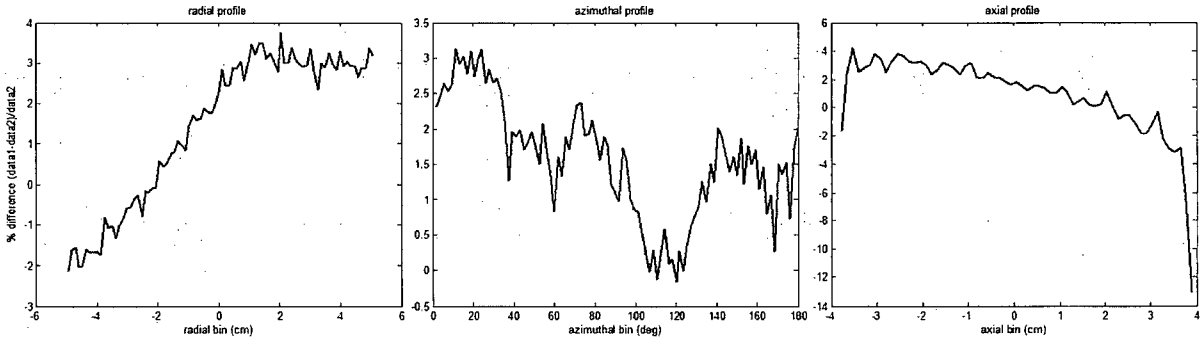

Figure 6-35 The radial (left), azimuthal (centre) and axial (right) summed percent difference (data1 = calculated, data2 = measured) profiles for contrast phantom 2, study 1. The profiles are summed over the other binning directions.

The contrast phantoms were also reconstructed using both the measured and calculated randoms corrections. The data from contrast phantom 2, study 1, had the highest randoms fraction (15%). To examine the effects of the randoms correction on image noise, this data was histogrammed into a 60 second frame to reduce the counts and increase the noise. This data was then randoms corrected using both the measured and calculated distributions and then reconstructed.

Visually, there were no apparent differences in the images that were randoms corrected by the different methods. Two count profiles were examined: one through a typical transverse slice, and the other along the long axis of the phantom. The profiles from both randoms correction methods were overlaid. **Figure 6-36** shows the profile through the transverse slice and **Figure 6-37** shows the profile through the coronal slice. In both cases, there are no significant differences between the profiles, inferring that the calculated correction introduces no detectable biases.

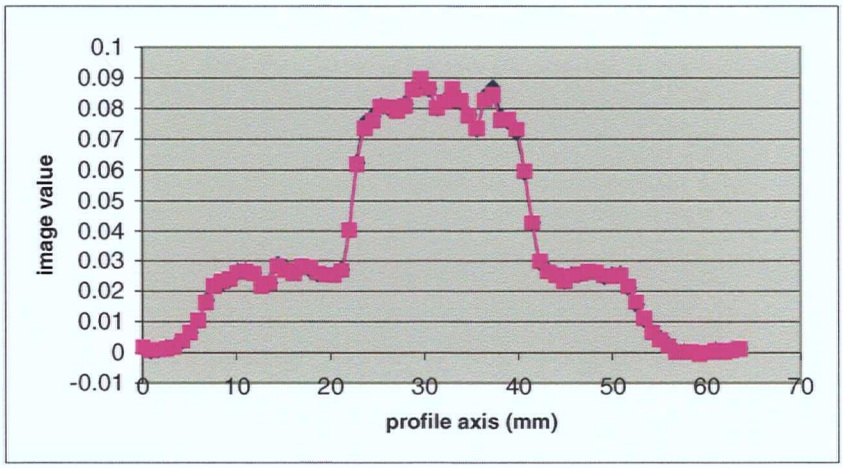

Figure 6-36 Profiles through transverse slice of the reconstructed image of contrast phantom 2 with measured (pink squares) and calculated (blue diamonds) randoms correction.

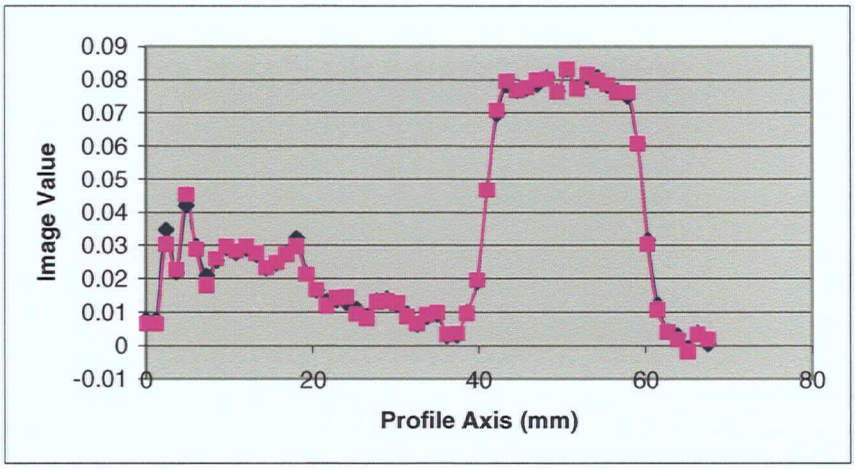

Figure 6-37 Profiles through coronal slice (long axis) of the reconstructed image contrast phantom 2 with measured (pink squares) and calculated (blue diamonds) randoms correction.

The low randoms fractions in the contrast and cylindrical phantoms experiments made them unsuitable for detecting the changes in noise due to the different methods of randoms correction. Therefore, data from an earlier scan of a uniform cylinder, with a significantly higher activity, were analyzed. This study used a uniform cylinder filled with ^{11}C which was scanned for 5 minutes. The

resulting average singles rate was 35.8 Mcps, with a trues rate of 2.6 Mcps and randoms rate of 1.2 Mcps (all values were dead-time corrected). The randoms fraction was 45%, and a total of 350 million delays were counted.

Images were reconstructed from the prompts data and after correction by both measured and calculated randoms. At these count rates, much higher than a realistic scanning situation, the dead-time corrections did not give accurate results. For this particular study the calculated randoms were scaled to the measured randoms. The noise in these image data sets was measured to determine the impact of the randoms correction method on noise. The prompts image should have the lowest noise. The image from a noiseless randoms correction should have identical noise to that in the prompts image. The subtraction of a noisy randoms distribution increases the image noise.

The image noise was measured using 16, 2 x 2 voxel ROIs placed at equal radial distances in one slice, as shown in **Figure 6-38.** For the randoms subtracted images, the noise was calculated as the ratio of the standard deviation in the ROIs of the corrected image to the mean of the ROIs in the prompts image, to account for the effect of subtracting counts on the mean value.

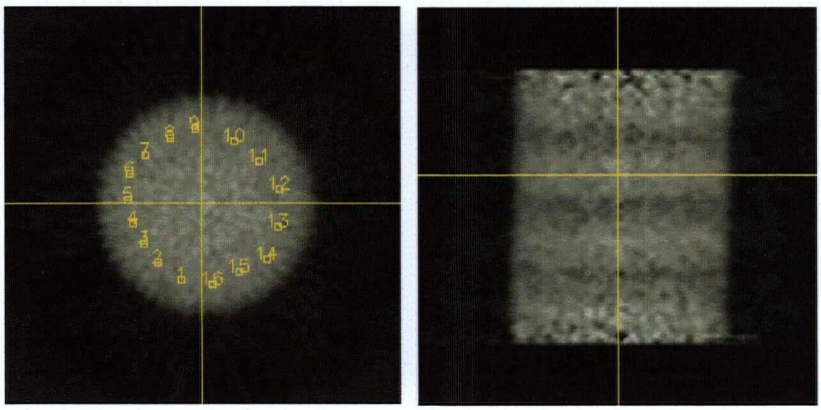

Figure 6-38 The placement of the ROIs on the hot uniform cylindrical phantom image. Note the image artifacts in the axial direction.

The resulting measured noise values in an off-centre slice (slice 24) are listed in **Table 6-13**. For this slice, the noise in the calculation corrected image is essentially identical to that in the prompts, while the image corrected by the measured delays had greater noise.

Table 6-13 The measured noise in slice 24 of the hot cylinder when the images are randoms corrected by difference methods.

Randoms Correction Method	Noise
prompts only (no subtraction)	4.8%
prompts– measured delays	5.7%
prompts – calculated randoms	4.7%

While this would appear to show the noise benefits of the calculated randoms correction, the results for all the slices were not the same. **Figure 6-39** shows the noise in all the slices of the hot cylinder for the different randoms corrections, measured using the same ROIs. In most of the slices, the delayed-corrected data shows the largest measured noise. However, for some slices the delayed-corrected noise is inexplicably lower than that from the prompts and calculation subtracted data. This cause for this discrepancy is likely related to the dead-time induced image artifacts, which are apparent in the **Figure 6-38**. These visual artifacts were not seen in a later study which was identical, except that the activity had decayed and the count rates were significantly lower. As well, although the randoms fraction in this data is high, the noise is low due to the large number of measured delays so the variations in the measured noise values may be simply random. However, in most slices the noise in the calculation subtracted images is usually close to that in the prompts, irrespective of the noise in the delays subtracted images.

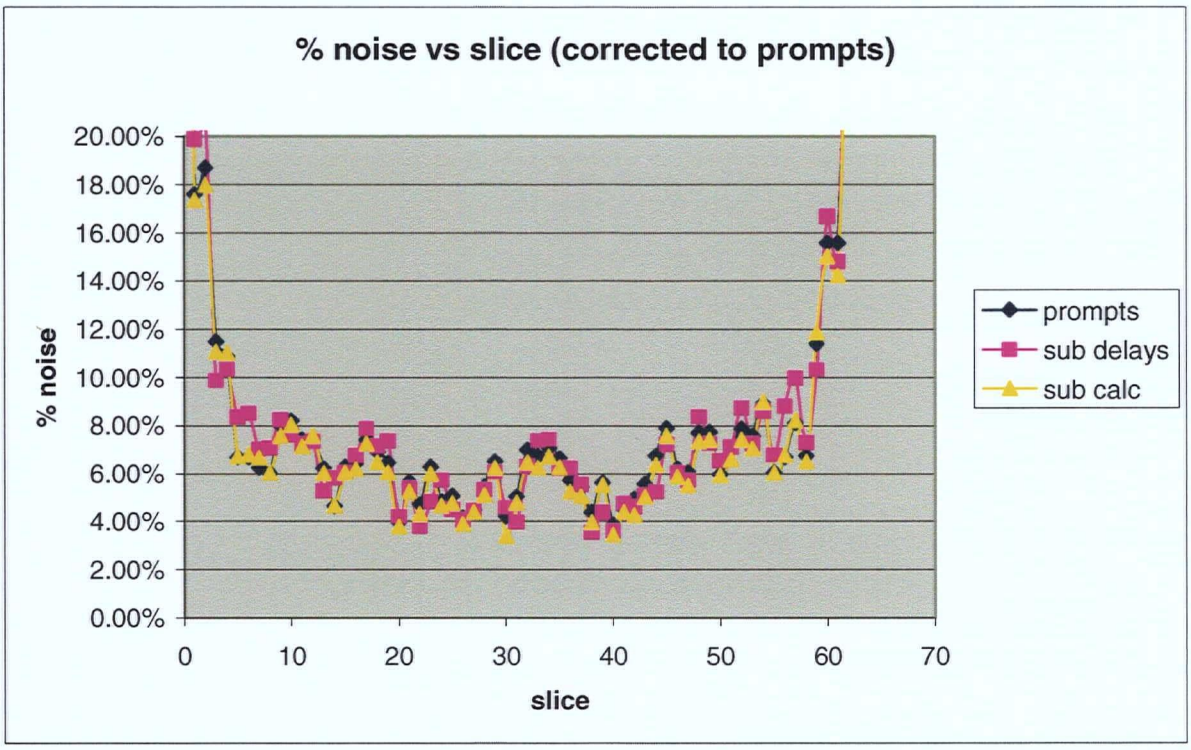

Figure 6-39 The measured noise in the slices of the hot phantom for different randoms corrections.

6.4.4 Animal Study

The results from the mouse study are listed in **Table 6-14**. Again, the calculation reproduces the measured randoms rates to within 0.4%. The trues rates agree to within 5%.

Table 6-14 Measured and calculated average count rates from the two mouse study.

Total Delays (Mcts)	Singles (kcps)	Trues (kcps)	Delays (kcps)	Delays % diff	Randoms Fraction (%)
5.9	618 (618)	37.1 (39.0)	0.539 (0.541)	-0.4	1.4

The measured and calculated central slice and summed slice sinograms are shown in **Figure 6-40** and **Figure 6-41.** Again, the general features of the measured randoms sinograms are well

reproduced. The percent difference sinogram for the summed slice sinogram shows only minor differences, mainly from the effects of random detector efficiency variations.

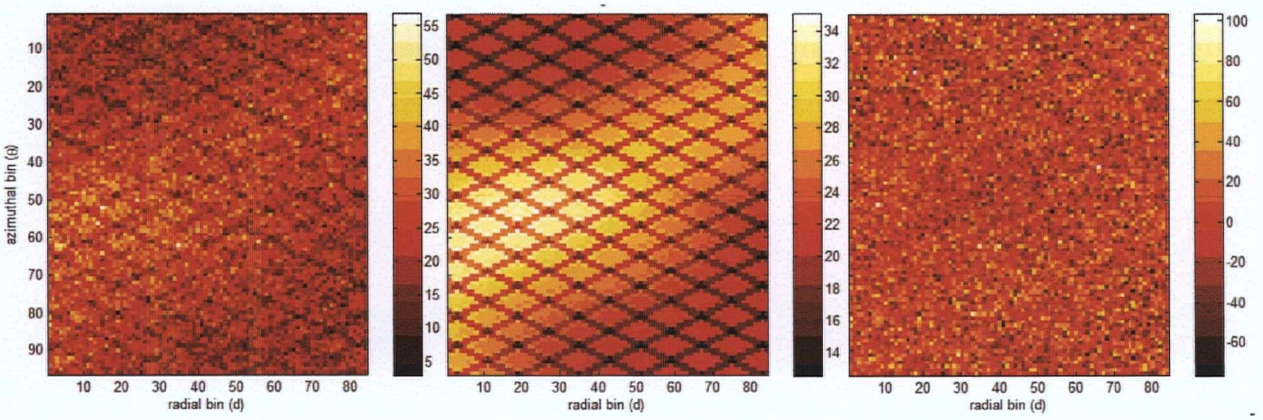

Figure 6-40 Measured (left) and calculated (centre) and percent difference (right) randoms sinograms for the central slice of the two mouse study. Note that the measured and calculated sinograms do not have the same scale.

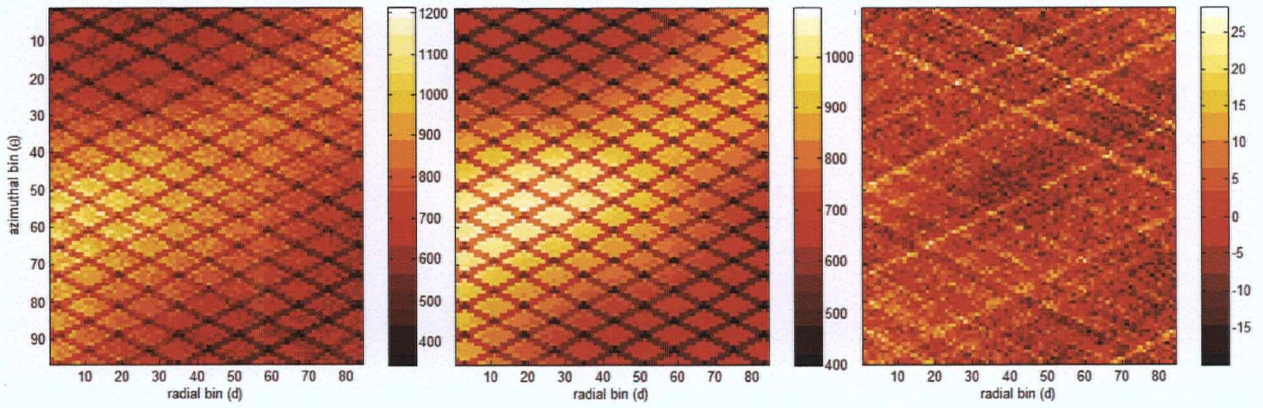

Figure 6-41 Measured (left) and calculated (centre) and percent difference (right) randoms sinograms for the summed slice of the two mouse study. Note that the measured and calculated sinograms do not have the same scale.

The radial, azimuthal and axial summed count profiles are shown in **Figure 6-42** and the summed percent difference profiles are shown in **Figure 6-43**. Again, the overall fit is very good. The small

slope seen in the percent difference axial profiles is indicative of a small amount of radioactivity outside the FOV (see **Figure 6-8.**)

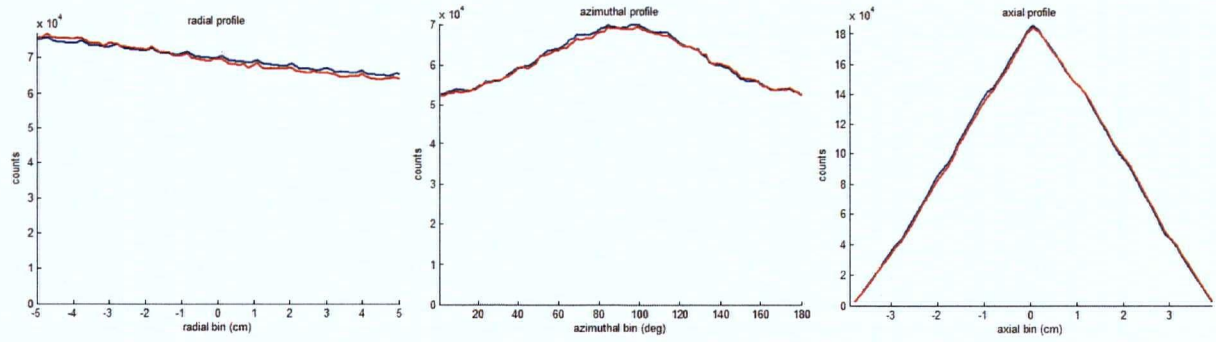

Figure 6-42 The radial (left), azimuthal (centre) and axial (right) summed count profiles of the measured (blue) and calculated (red) randoms distributions from the two mouse study.

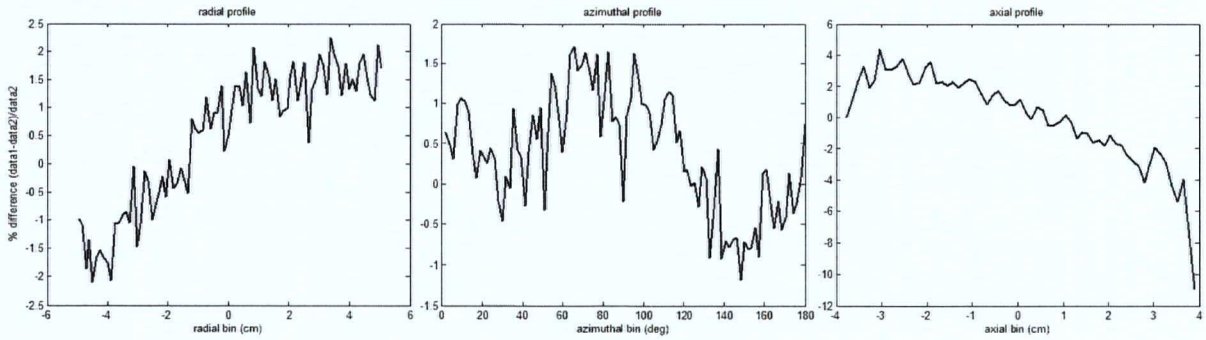

Figure 6-43 The radial (left), azimuthal (centre) and axial (right) summed percent difference (data1 = calculated, data2 = measured) profiles for the mice study.

The calculated FoMs for the sinograms in this study are given in **Table 6-15.** In the central slice sinogram, $\chi^2/N \approx 1$, so the FoMs are dominates by Poisson noise. For the summed slice sinogram, $\chi^2/N > 1$, so the low values of the *NMSE* and *sd(%diff)* and the high value of the 2D correlation coefficient indicate the biases are very small.

Table 6-15 The values of the FoMs between measured and calculated randoms distributions in the mouse study for the central slice sinogram and the summed slice sinogram.

slice	*NMSE*	*sd(% diff) (%)*	χ^2/N	r_{2D} (%)
central	4.8	13.5	1.06	67.5
summed	0.37	3.8	2.55	95.9

The mice study data was then corrected by both the measured and calculated randoms and images were reconstructed. Profiles through both images are shown in **Figure 6-44** and **Figure 6-45**. These profiles show good agreement indicating that the calculated randoms correction does not introduce a significant bias into the reconstructed images.

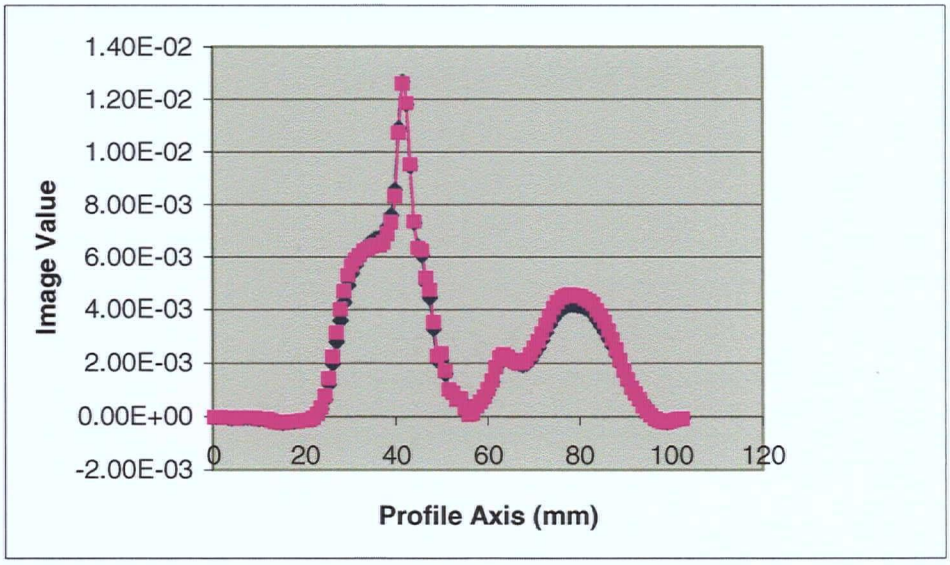

Figure 6-44 Profiles through transverse slice of the reconstructed mice image using measure (pink squares) and calculated (blue diamonds) randoms correction.

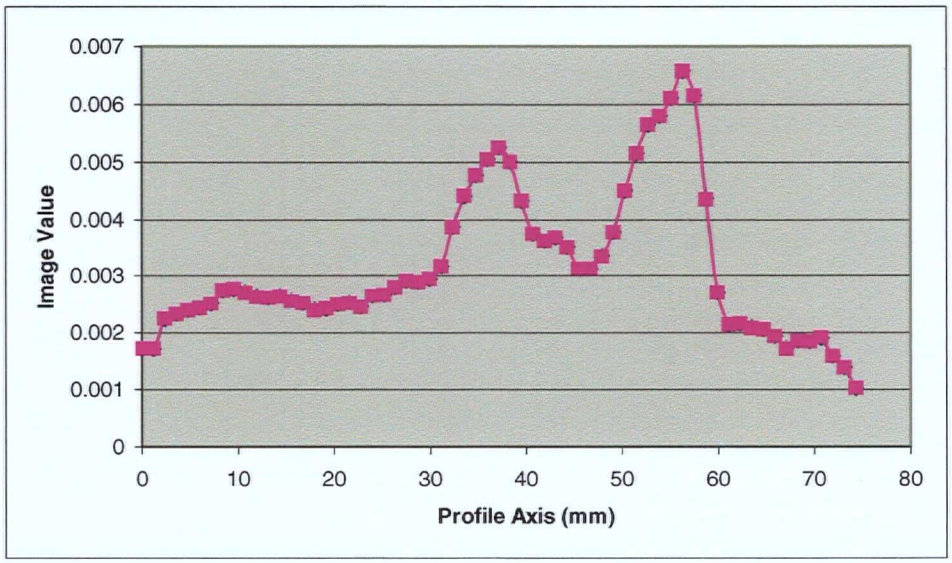

Figure 6-45 Profiles through coronal slice (long axis) of the reconstructed mice image using measure (pink squares) and calculated (blue diamonds) randoms correction.

The measured and calculated randoms sinograms from the mouse study were also reconstructed into images of the randoms distributions using FORE and 2D-FBP. Representative transverse and coronal slices of the measured, calculated and subtracted images are shown, respectively, in **Figure 6-46** and **Figure 6-47.** They show an excellent agreement in the overall shape of the randoms image. However, the randoms image reconstructed from the calculated sinograms is far less noisy and has higher contrast than the image from the measured randoms. When the images are subtracted, the resulting image shows no structure, only noise for this slice. This indicates that there is no detectable bias between the methods in this example. The coronal images likewise agree, but show some possible reconstruction artifacts.

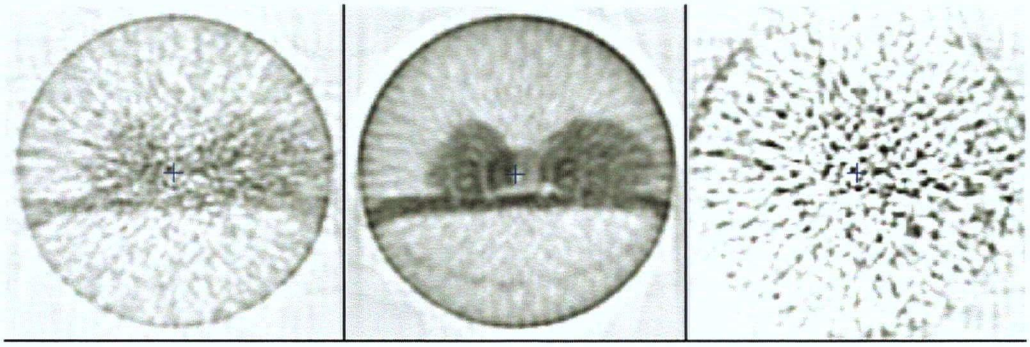

Figure 6-46 Reconstructed randoms central transverse slice images from measured (left) and calculated (centre) randoms sinograms. Also shown is the subtraction image (right).

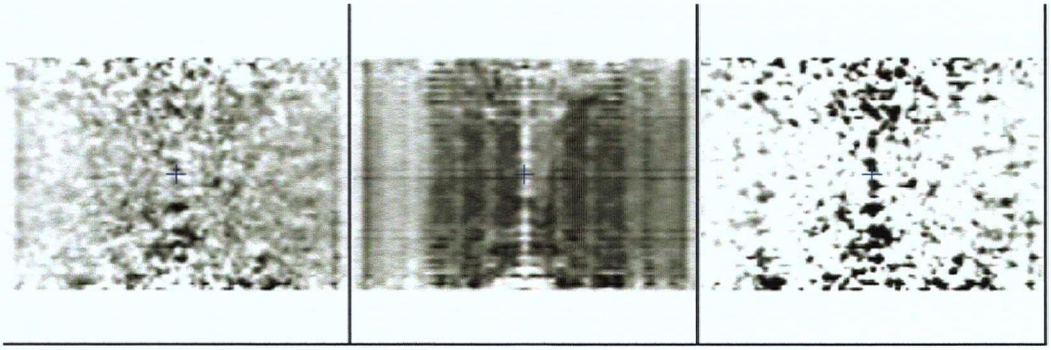

Figure 6-47 Reconstructed randoms coronal images from measured (left) and calculated (centre) randoms sinograms. Also shown is the subtraction image (right).

Chapter 7

Discussion and Summary

7.1 Discussion of Results

7.1.1 Chapter Overview

Chapter Six described the studies performed to test the accuracy of the model-based randoms correction against measured randoms distributions from phantom and animal scans. The results were analysed by comparing measured and calculated randoms rates and randoms distributions. As well, images reconstructed from data corrected using measured and calculated randoms were compared.

Chapter Seven provides a discussion of the results the validation tests and a summary of this work. The chapter begins with a discussion of the results of the validation testing. Then, possible improvements to the model-based calculation method are described. Next, suggestions for future work using this method are given, including a discussion on implementation for other tomographs. The chapter ends with a summary of the accomplishments of this work.

7.1.2 Accuracy of Calculated Global Rates

The randoms calculation reproduced the measured global randoms rates to within $\leq$ 1.4% for essentially all the phantom and animal studies. The accuracy of the calculated randoms rates is almost entirely attributable to scaling by the measured global singles rates. This parameter provides an empirical factor that negates the absolute errors in the calculated solid angle, detector efficiency, photon survival and other parts of the singles calculation by forcing the global singles rates to be correct.

Nonetheless, the accuracy of the calculated randoms rates also depends the computation of the randoms from the singles, and on the dead-time and decay corrections. The corrections used in the randoms calculation were found to give accurate results for studies with singles rates $\leq$ 9.6 Mcps and dead-times $\leq$ 63%; higher singles rate and the dead-times were not studied. These rates are already much higher than those in the representative animal study; which had an average singles rate of only 618 kcps over a three hour scan. However, the decay correction was only accurate when the LSO background singles rate was taken into account.

The only large discrepancy in randoms rates was for the 12 hour frame of the line source study (4.7%). The likely cause of this disagreement is an error in the dead-time correction factor calculated by the MicroPET for scans of such long duration. The dead-time correction factor value is derived from the average singles rate over the entire frame duration. The dead-time correction calculated by the MicroPET was earlier found to have problems when the duration of the time frame is much longer than the half-life of the radionuclide [109]. Since animal studies generally do not have long frame durations, this is not problematic. One possible factor could be the background singles from LSO background, which has the largest effect when the source activity is low [103]. It is unclear whether the MicroPET calculation takes this into account. A newer version of the MicroPET dead-time correction may improve this aspect of its performance.

The calculated trues rates were compared to the measured rates to assess the accuracy of the model-based calculation in reproducing the magnitude of the trues. The differences between measured and calculated trues rates ranged from <1% to 32%. The error in the trues rates for the animal study was only 5%. Not surprisingly, the largest errors were for point sources near the axial ends of the tomograph. This was compounded by the small values of trues rates near axial edge; small absolute differences in rates translate into large relative differences. Studies with point sources near axial edge in water were especially inaccurate because photons have the longest path in attenuating material and the effects of attenuation and scatter are the greatest. As well, scatter has a larger effect on coincidence events than singles events. Activity outside the AFOV also causes significant error in the calculated trues rate.

Since the present photon detection model is not optimized for calculating trues, the accuracy is not expected to be as good as that for the randoms. Specifically, the calculation does not take the path of the annihilation partner photons into detailed account, especially near the axial edge of the tomograph. As well, the exact detector(s) that the partner photons hit are not calculated; thus, the crystal efficiency variations cannot be included in the trues calculation. As well, any inaccuracy in the photon detection model is compounded by the required detection of two photons, and the scaling to the measured singles rates enhances this error for the trues. For example, an error in the

estimation of the detection efficiency is squared for the detection efficiency for two photons. Taking these issues into account, it was expected that the accuracy of the calculated trues would be ~10-20%, and to be worst near the edge of the axial FOV. Future improvements in the photon detection model (**Section 7.2**) could potentially lead to a more accurate calculation of the trues.

7.1.3 Accuracy of Calculated Randoms Distributions

The accuracies of the spatially variant calculated randoms distributions were also measured for many different sources configurations. The studies showed excellent visual agreement between the measured and calculated randoms sinograms; however, the calculated sinograms were completely smooth, while the measured ones were generally very noisy. The calculated sinograms were able to replicate all the features of the measured sinograms: the high frequency "block structure" due to systematic variations in crystal efficiency within a detector block, and the low frequency variations due to the non-uniform singles distribution. The point sources at different positions in the FOV showed a variety of randoms distributions, which the calculation was able to reproduce. The calculation also worked well for the more complex activity and attenuation phantoms.

The most noticeable difference between the measured and calculated sinograms was seen as a few randomly positioned diagonal lines in the percent difference sinograms. These produce the largest discrepancies in the percent difference sinograms. The lines were caused by random variations in the singles efficiencies of individual crystals. The singles calculation models only systematic efficiency variations within the detector blocks. Random differences between individual crystal efficiencies are not measured nor included in the model. These differences only affect a few pixels; thus, they do not have a major impact in the overall randoms contribution. The low number of counts in the affected pixels, caused by the lower efficiency of the edge crystals, enhances the percent difference seen in the sinograms.

The other noticeable difference between the measured and calculated sinograms is the curved line (or band) of reduced counts ("dip") in the measured randoms at the LORs that correspond to the LORs with the highest count rates in the trues sinograms. This feature is most noticeable in the

analysis of the line and point sources in air, where the trues are concentrated in a few LORs. In the radial summed percent difference profiles, this artifact has a magnitude of up to 5-6%. For sources in water, the scatter broadens the trues sinograms and the magnitude of the artifact is reduced. This feature may also be seen in the randoms sinograms of extended sources, such as uniform cylinders, but it is much more diffuse. Nevertheless, this count reduction is not seen in slices of the randoms distribution that contain few counts in the trues distribution (**Figure 6-12**).

This artifact is not reproduced by the randoms calculation and the cause of the artifact is not clear. Since the randoms distributions are based on a smooth singles distribution, such a sharp feature is not likely due to the singles distribution. The possibility of it being caused by dead-time was investigated. A high count study using a low activity ^{68}Ge point source was done at low count rates. The measured randoms sinograms from this study showed the same artifact. However, a detailed Monte Carlo simulation of an identical point source configuration in the MicroPET was done using GATE [108]. The simulated randoms distribution did not reproduce this artifact [109]. The possibility of this artifact being caused by the tomograph coincidence processor or the histogramming software requires investigation. If this is a problem with the delayed coincidence processing, the calculated correction may be more accurate than the measured correction in studies where is artifact is pronounced.

The comparison of the count and percent difference profiles also showed remarkably good agreement between measurement and calculation for all studies. In the high count 12 hour line source study, the individual radial, azimuthal and axial profiles were directly compared in both 3D data sets and rebinned data. In the other studies, the comparison of summed profiles was required to reduce the noise so that biases could be detected. For most studies, the biases in the summed radial profiles were within as about ± 2-3% across the entire radial FOV. The point source studies had the worst bias in the radial profiles because of the dip artifact (for example. **Figure 6-29** and **Figure 6-30**). The results were also with ± 2-3% for the azimuthal and axial profiles, except when activity outside the axial FOV increased the bias in the axial profiles. However, it should be noted that summed profiles could potentially mask some systematic biases.

The calculated figures of merit were of some use in detecting and quantifying the bias. The value of χ^2/N identified the studies for which the differences were not purely Poisson, and were therefore due to bias. The magnitude of the bias for these studies was then estimated from the *NMSE* and other FoMs. For these all studies, the bias measured by the FOMs appeared to be small.

The good agreement of the randoms calculation appeared to be independent of object size, for the phantoms that were studied. This demonstrates that the scaling to the measured singles rates takes the global effects of object size into account.

7.1.4 Effects of Count Rates and Radioactive Background

Changes in the singles and randoms distributions due to high count rates were not detected in the validation studies. However, changes in the randoms distributions at low count rates were found. These were due to randoms caused by the background activity in the LSO. For low count rate studies, the accuracy of the randoms calculation depended on an accurate measurement of the detector singles rates in the absence of activity in the tomograph FOV. When this effect was included, the calculation produced a randoms distribution in agreement with the measurements.

7.1.5 Effects of Radioactivity outside the AFOV

The effects of radioactivity outside the axial FOV were assessed using uniform cylindrical phantoms. For the large phantom, the activity outside the FOV caused a slope in the axial percent difference profile which amounted to a bias of ± 5% at the edges of the axial FOV (**Figure 6-32**). The scaling to the singles ensures that the percent difference at the centre slice is ≈ 0%, and the errors are largest at the axial ends. For the small cylinder, the largest axial bias is ± 8% at the edges, when 30% of the activity is outside the AFOV.

While these are relatively large differences, the total effect on the image is small. The total true and random counts in the end planes are the lowest of any planes because of the triangular shape of the axial counting sensitivity (for example, **Figure 6-31, right**). During reconstruction, these planes are scaled by the inverse of the counting sensitivity in the images so the bias might be

enhanced. However, because the resulting image noise in these planes is very high, biases in the randoms correction of this magnitude are likely to be insignificant compared to the noise.

7.1.6 Effects of the Calculated Randoms Correction on Reconstructed Images

For both contrast phantoms and the mouse study, the use of the calculated randoms correction did not introduce any appreciable bias into the reconstructed images, as seen by the profiles. However, there was also no apparent difference in the image noise. The calculated randoms sinograms clearly show much lower noise than the measured randoms. The reconstructed image of the calculated randoms distribution of the mice study was also significantly less noisy than the image from the measured randoms (**Figure 6-46**). Therefore, it is expected that the smoothness of the calculated sinograms should translate into reduced image noise, and improved contrast-to-noise levels.

Thus, the high activity cylindrical phantom data was used to determine the impact of the calculated randoms correction on image data. This data had a large randoms fraction (45%), so that the randoms contribute more to the image data and the effects of the randoms correction would be more apparent. The results, though showing some improvements, were not easy to interpret because of the image artifacts, most likely caused by the high dead-time. Some measurements of image noise were also done on the lower, but still high, count rate scans of the contrast phantoms with a randoms fraction of 15%. These images showed no dead-time related artifacts, but the measurements showed no discernable change in image noise. The count rates and randoms fractions in these studies are much higher than those attained in typical animal scans. The short coincidence timing window and high sensitivity of this tomograph result in very low randoms fractions. Therefore, it may be concluded that, for realistic studies performed on this tomograph, the calculated randoms correction would have no discernable impact on the noise. This is not because of inadequacies in the method, but simply due to the small contribution of the randoms to the image data. However, the low noise properties of this method might have a greater impact if used on larger tomographs for whole-body human studies where the randoms fractions are much higher.

7.2 Possible Improvements to the Single Photon Detection Calculation

7.2.1 Introduction

A number of improvements to the randoms calculation have been suggested by the validation tests. Each improvement could have an impact on the accuracy, but also on the computational efficiency. The importance of each is dependent on the tomograph being modeled and the acquisition parameters used.

7.2.2 Detector Binning

In tomographs with large numbers of crystals, the burden of calculating the solid angle and especially, the photon survival, to each crystal could cause unreasonably large calculation times. Since the singles distribution changes slowly, a coarser sampling of the tomograph could be used, where a single detector bin would represent a few crystals. The calculated singles distribution could be interpolated to the true number of crystals before the block structure is applied and the randoms distributions are calculated.

7.2.3 Detector Solid Angle Calculation

In the model-based calculation, the solid angle is calculated as if all the photons interact at a fixed surface of the detectors. A more accurate calculation of the solid angle could be done by integrating the intersection of a rectangular photon beam with the crystal from the front face to the back of the scintillator block. This calculation would include the complex effects of varying beam intensity due to attenuation in the crystal. The contributions to multiple crystals and the effects of the block cuts would be included in the calculation. This change especially improves the accuracy of the calculation near the axial edges of the tomograph where the photon beam may intersect only a few partial crystals. However, the method of solid angle calculation would greatly increase the computational burden. Such an improvement would be added only if the accuracy of the present calculation is found to be inadequate.

An improvement in the solid angle calculation could also be done for the collinear annihilation partner photons used in the calculation of the true coincidences. Presently, the beam spread of the

partner photons is not computed, nor is the detection by specific crystals. This leads to errors in the calculated trues rates and distributions. If the individual crystals that detect the partner photons are identified, the crystal efficiency variations could be used in the trues calculation to improve the accuracy.

7.2.4 Broad-beam and Window Fraction Correction Factors

As described in **Section 4.6.1**, the present photon survival calculation uses a single, average value for the broad-beam correction $\varkappa_{broad}$. In general, build-up factors depend on the product μx and should vary for every photon path. Since the photon survival calculation explicitly determines μx, a path-dependent broad-beam correction factor could be easily implemented if necessary. The path dependent value of $\varkappa_{broad}$ may be estimated from **(4.24)** and **(4.25)** using the values of $\mu_{obj}x_{obj}$ for a given path found by the photon survival calculation **(4.8)**. This modification is not expected to increase computational burden. Such a correction would probably be of greatest benefit in the photon detection model for whole-body tomographs, where the photon paths are longer and the build-up factors vary more.

A path-dependent detection efficiency correction factor might also be investigated. Since, the detector efficiency calculation explicitly determines μx for the photon path in each crystal; $\varkappa_{det}$ could be made to vary with μx, mainly to account for changes in the Compton-absorption probability. Again, this would likely not significantly increase computational burden but could marginally increase the accuracy of the detection model for all tomographs. This could be implemented in conjunction with changes in the solid angle calculation (**Section 7.2.3**).

7.2.5 Single Photon Scatter Distribution

The present model-based calculation assumes that the amount of single photon scatter and its effects on the singles distribution are small. In larger tomographs this is not true, and a more detailed correction for the effects of single photon scatter on the singles distribution may be necessary. One possible method would be to calculate the distribution of object-scattered single photons about their unscattered path (**Section 4.6.3**). While this might improve the accuracy of

the calculated singles distribution, there would probably be an enormous penalty in the required computation times, because of the complexity of this calculation.

7.2.6 Crystal Efficiency Variations

The present single photon detection model uses a simple model of detector efficiencies that takes into account only systematic variations, but not individual detector efficiencies. A more accurate method would use measured individual crystal singles efficiencies. These values may be extracted from the component-based normalization data or from measuring the energy spectra of individual crystal block elements. Using individual singles efficiencies in the calculation would reduce the effects of the random efficiency variations on the calculated randoms distributions. Implementing this change in the algorithm would be trivial and the impact on computation times would be negligible. However, the measurements of singles efficiencies could be problematic and may require extensive measurements and analysis. As well, the detector efficiency model would require regular updating.

7.2.7 Radioactivity Outside of the Axial Field of View

The randoms calculation assumes that all of the radioactivity distribution that contributes to the measured singles rates is present in reconstructed radioactivity image. The contribution from singles originating in radioactivity not in the image is not calculated. In practice, this occurs when significant radioactivity is present outside the axial field of view. The effect of activity outside the AFOV is greater for tomographs with larger ring diameters.

The calculated randoms correction could easily correct for this if multiple bed positions are scanned. The reconstructed image data from multiple views would be knitted together, and activity sample points would be generated in this extended volume. The singles distribution would then be calculated, and the randoms distribution computed, for multiple bed positions separately. If scans are done using only a single bed position, other strategies would be required.

7.3 Future Directions for this Work

7.3.1 Introduction

This work demonstrates that the model-based randoms calculation is a valuable, viable method for performing accurate and noiseless randoms correction. Further testing might be done to determine the performance of the method under a greater range of conditions. As well, the present method may be adapted for use on other tomographs.

7.3.2 Other Measurements

While the previous testing was able to establish the basic accuracy of the model-based calculation, further tests may be helpful. Given the short coincidence timing window and high sensitivity of the MicroPET, it was difficult to achieve high randoms fractions. Higher randoms fractions could be reached by using higher activity sources; however, the detector dead-time may become an issue. Higher randoms fractions could also be achieved simply by using a longer coincidence timing window. For example, studies acquired using T_{CTW} = 12 ns would have double the random coincidences compared to acquisition with the standard 6 ns. This would allow the testing of this method in the presence of higher randoms fraction and would better show the effects of the calculated correction on noise. However, this would be somewhat artificial. The calculated randoms correction method would be better tested by adapting it for use on a whole body scanner and testing it on such as system.

This method is applicable to evolving tracer distributions. The validation tests only involved measuring static radionuclide distributions. The application of this randoms correction should be tested for dynamic studies by calculating the randoms corrections for individual time frames.

7.3.3 Extension to other Tomographs

The testing and validation of this method has only been performed on one type of small animal scanner. In theory, this method is applicable to any coincidence imaging system. A natural extension of this work would be to adapt the method and test it on other tomographs. The geometric aspects of the model-based randoms calculation should scale with the tomograph size.

The noiseless character of this randoms correction would be of the greatest benefit when used for whole body imaging of human subjects. Therefore, this method should be applied to whole body PET imaging.

A number of issues would need to be addressed when adapting this method for larger scanners and subjects. First, the singles and randoms sensitivities are strongly dependent on the ring diameter and axial FOV [109]. Activity outside the axial FOV also causes more singles in whole body scanners, which may be problematic for this method. Also scatter and attenuation become more significant when imaging larger subjects. As well, the increased ring diameter increases both the displacement of the scattered single photons, which may reduce the validity of using a simplistic broad-beam model for single photon scatter. These, and other differences, may require modifications to the single photon detection model. Potential solutions to these some of these issues are described in **Section 7.2**.

7.3.4 Other Uses for this Work

Although this work has focussed on randoms correction, a number of derivative uses for the methods and tools developed during the research have been suggested. These include expanded uses for the model-based simulation and for the analysis tools that were developed

This randoms correction method uses a newly developed model-based simulation. In the present application, the simulation is data driven; that is, it is based on, and scaled to, measured data. However, this model-based simulation algorithm could potentially be used for other simulation research, in place of slower Monte Carlo simulations for some applications. However, much more work would be required to improve the accuracy for trues calculation and produce accurate results when scaling to absolute values in the activity object rather than measured count rates.

The CODEX suite of analysis tools (**Section 5.1.3**) was developed as part of the testing and validation work for the randoms correction calculation. These tools could potentially be used for visualization and analysis with any image data set, measured or simulated. Since they employ a graphical user interface, they are simple to use. These tools were developed and coded in

MATLAB so they could also be easily ported to multiple computer platforms. There has already been an expression of interest in possibly incorporating the CODEX tools with another set of software used in imaging research.

7.4 Summary and Conclusion

A new method of randoms correction for PET has been presented. This is a singles-based method that uses the calculated singles distribution from a model-based simulation involving the preliminary reconstructed radioactivity and attenuation data. The calculated singles are scaled to the measured global singles rate. The spatially variant randoms distributions are calculated from the singles, decay corrected and subtracted from the measured prompts sinograms. This method is a logical extension of the model-based calculations presently used in scatter corrections and normalization.

The calculated randoms has a number of benefits over the measured delay subtraction method. First, the model-based correction requires no measurement of the delayed coincidence channel. This reduces the load on the coincidence processor during acquisition and potentially decreases the coincidence dead-time during acquisition. As well, since no delayed coincidences are collected, the size of the data set is reduced by a factor of two if delayed coincidence data is stored separately in histogram mode. Since this new method does not make any use of delayed coincidence events, this goal is clearly achieved. In addition, other singles-based randoms corrections require the measurement, storage and processing of detector singles events. The model-based method only requires the measured global average singles rate for scaling. This again reduces the measurement and storage requirements compared to some other singles-based methods. As well, since the singles rates are calculated for every crystal, the model-based method avoids the biases in single-based methods that use the measured singles from large groups of detectors.

Another anticipated benefit is that the calculated randoms distributions should be smooth. This property leads to less noise in the randoms corrected data and, consequently, less noise in the reconstructed images. Inspection of the calculated randoms sinograms clearly shows they are

smooth. The images reconstructed from the calculated randoms sinograms are much less noisy than images from the corresponding measured randoms sinograms. However, measurements of the noise in reconstructed images did not show any significant reduction when the calculated randoms correction was used because the random fraction of the data was too low.

The accuracy and reproducibility of the calculated randoms distribution is also an important issue. Comparison between the measured and calculated randoms distributions showed only minimal bias. In general, the bias was much smaller than the noise in the measured distributions. The accuracy of the calculated randoms was also found to be nearly independent of the value of the empirically measured calculation parameters. However, it was also found that the inclusion of a correction for the LSO background was necessary for accurate results, especially for low activity studies. The reproducibility of the calculated randoms distributions depends on the number of sample points used. A large set of sample points also minimizes any biases caused by the noise in the preliminary activity image. Thus, the model-based randoms correction was shown to work for a small animal scanner.

This method could also bring its advantages to human, whole body PET imaging. The smooth randoms distributions would reduce the noise in the corrected image data. As well, the reduced data acquisition and storage demands would lessen the load on the acquisition and processing hardware. In general, this randoms correction method could potentially benefit all PET imaging.

BIBLIOGRAPHY

[1] Webb S, ed. *The Physics of Medical Imaging.* Institute of Physics Publishing Bristol and Philadelphia, 1988.

[2] Cho Z-H, Jones JP, Singh M, *Foundations of Medical Imaging.* Wiley, New York, 1993.

[3] Hounsfield GN. A method of, and apparatus for, examination of a body by radiation such as X-ray or gamma radiation. British Patent No. 1283915, London, 1972.

[4] Ter-pogossian M, Phelps M, Hoffman EJ, et al. A positron emission transaxial tomograph for nuclear imaging (PETT). *Radiology* 114:89-98, 1975.

[5] Pais, A. *Niels Bohr's Times* Oxford University Press, p.27 1991.

[6] Pointon BW. *SPECT: Physics and Instrumentation for Technologists.* Canadian Association of Medical Radiation Technologists (CAMRT). Ottawa, 1997.

[7] Ter-Pogossian MM, The origins of Positron Emission Tomography. *Semin Nucl Med.* 12:140-149, 1992.

[8] Ruth TJ. Private communication.

[9] Friedlander G, Kennedy JW, Macais ES, Miller JM. *Nuclear and Radiochemistry 3rd Ed.* Wiley. New York, 1981. pp.78, 467-469.

[10] Charlton M, Humberson JW. *Positron Physics.* Cambridge University Press, Cambridge, UK., 2001. pp.3-11, 264-274.

[11] Levin CS, Hoffman EJ. Calculation of positron range and its effect on the fundamental limit of positron emission tomography system spatial resolution. *Phys Med Biol.* 44:781-799, 1999.

[12] Duxbury DM, Ott RJ, Flower MA, Erlandsson K., Reader AJ. Preliminary results from the new large-area PETRRA positron camera. *IEEE Trans. Nucl Sci.*46:1050-1054, 1999.

[13] Bailey DL, Young H, Bloomfield PM, Meikle SR, Glass D, Myers MJ, Spinks TJ, Watson CC, Luk P, Peters AM and Jones T. ECAT ART - a continuously rotating PET camera: performance characteristics, initial clinical studies, and installation considerations in a nuclear medicine department. *Eur. J Nucl. Med.* 24:6-15, 1997.

[14] Patton JA, Turkington TG. Coincidence imaging with a dual-head scintillation camera. *J Nucl Med.* 40:432-441, 1999.

[15] Zanzonico P. Positron Emission Tomography: A review of basic principles, scanner design and performance, and current systems. *Semin Nucl Med.*34:87-111, 2004.

[16] Humm JL, Rosenfeld A, Del Guerra A. From PET detectors to PET scanners. *Eur J Nucl Med Mol Imaging.* 30: 1574-1597, 2003.

[17] Wienhard K, et al. The ECAT HRRT: performance and first clinical application of the new high resolution research tomograph. *IEEE Trans Nucl Sci.* 49:104-110, 2002.

[18] Laforest R, Longford D, Siegel S, Newport D, Yap J. Performance evaluation of the MicroPET-Focus 120. *IEEE Nucl Sci Symp Conf Rec.* 5: 2965-2969, 2004.

[19] Melcher CL. Scintillator Crystals for PET. *J Nucl Med.* 41:1051-1055, 2000.

[20] Adapted from refs 9, 10 and from Cherry SR, Sorenson, JA, Phelps ME. *Physics in Nuclear Medicine, 3rd Edition.* Saunders, Philadelphia, PA, 2003. p 340.

[21] Melcher CL, Schweitzer JS. Cerium Doped Lutetium oxyortho-silicate: A fast and efficient new scintillator. *IEEE Trans Nucl Sci.* NS-39:502-505, 1992.

[22] Watson CC, Casey M, Eriksson L, Mulnix T, Adams D, Bendriem B. NEMA NU 2 performance tests for scanners with intrinsic radioactivity. *J Nucl Med.* 45:822-826, 2004.

[23] Yamamoto S, Horii, H, Hurutani M, Matsumoto K, Senda M. Investigation of single, random and true counts from natural radioactivity in LSO-based clinical PET. *Annals of Nucl Med.* 19:109-114, 2005.

[24] Casey ME, Nutt R. A multi-slice two-dimensional BGO detector system for PET. *IEEE Trans Nucl Sci.* NS-33:760-763, 1986.

[25] National Electrical Manufacturers Association; *NEMA Standards Publication NU 2-2001: Performance Measurements of Positron Emission Tomographs.* Rosslyn, VA: National Electrical Manufacturers Association; 2001.

[26] Daube-Witherspoon ME, Karp JS, Casey ME, et al. PET performance measurements using the NEMA NU 2-2001 standard. *J Nucl Med.* 43:1398-1409, 2002.

[27] Moses WW, Derenzo SE. Empirical observation of resolution degradation in positron emission tomographs using block detectors [abstract]. *J Nucl Med.* 34 (suppl):101P, 1993.

[28] Cherry SR, Sorenson, JA, Phelps ME. *Physics in Nuclear Medicine, 3rd Edition.* W.B. Saunders Company, Philadelphia, PA, 2003. pp 325-359.

[29] Strother SC, Casey ME, Hoffman EJ. Measuring PET scanner sensitivity: relating countrates to image signal-to-noise ratios using noise equivalent counts. *IEEE Trans Nucl Sci.* 37:783-788, 1990.

[30] Rahmim A, Lenox M, Reader AJ, Michel C, Burbar Z, Ruth TJ, Sossi V. Statistical list-mode image reconstruction for the High Resolution Research Tomograph. *Phys Med Biol.* 49:4239-4258, 2004.

[31] Fahey F. Data acquisition in PET imaging. *J Nuc Med Technol.* 30:39-49, 2002.

[32] Defrise M, Kinahan P, Data acquisition and image reconstruction for 3D PET, Chapter 2 in Bendriem B and Townsend DW, eds. *The Theory and Practice of 3D PET,* Kluwer Academic Publishers, Boston, 1998. pp 11-53.

[33] Bruyant PP. Analytic and iterative reconstruction algorithms in SPECT. *J Nucl Med.* 43:1343-1358, 2002.

[34] Defrise M, Kinahan PE, Michel C. Image reconstruction algorithms in PET, Chapter 4 in Positron Emission Tomography Basic Science and Clinical Practice, eds. Valk PE, Bailey DL, Townsend DW, Maisey MN, Springer, London, 2003.

[35] Shepp LA, Vardi Y. Maximum likelihood reconstruction for emission tomography. *IEEE Trans Med Imaging.* M1-1:113-122, 1982.

[36] Lange K, Carson R. EM Reconstruction algorithms for emission and transmission tomography. *J Comput Assist Tomogr.* 8:306-316, 1984.

[37] Hudson HM, Larkin RS, Accelerated image reconstruction using ordered subsets of projection data, *IEEE Trans Med Imag.* 13, 601-809, 1994.

[38] Politte DG, Snyder DL. Corrections for accidental coincidences and attenuation in maximum-likelihood image reconstruction for positron-emission tomography. *IEEE Trans Med Imaging.* 10: 82-89, 1991.

[39] Hogg D, Thielemans K, Mustafovic S, Spinks TJ, A Study of Bias for various Iterative Reconstruction Methods in PET, *2002 IEEE Nuclear Science Symposium Conference Record.* 3:1519-1523, 2002.

[40] Qi J, Leahy R, Resolution and noise properties of MAP reconstruction for fully 3-D PET. *IEEE Trans Med Imag.* 19:493-506, 2000.

[41] Kinahan PE and Rogers JG. Analytic 3D image reconstruction using all detected events. *IEEE Trans. Nucl. Sci.* 36: 964-968, 1990.

[42] Defrise M, Kinahan PE, Townsend DW, Michel C, Sibomana M, Newport D. Exact and approximate rebinning algorithms for 3D PET data. *IEEE Trans Med Imag.* 16:145-158, 1997.

[43] Daube-Witherspoon ME, Muehllehner G. Treatment of axial data in three-dimensional positron emission tomography. *J Nucl Med.* 28:1717-1724, 1987.

[44] Zaidi H, Hasegawa B. Determination of the attenuation map in emission tomography. *J Nucl Med.* 44:291-315, 2003.

[45] Jones W, Vaigneur K, Young, J, et al. The architectural impact of single photon transmission measurements on full-ring 3D positron tomography. *IEEE Nucl Sci Symp Med Imaging Conf Rec.* 2:1026-1030, 1995.

[46] Watson CC, Jones WF, Brun T, et al. Design and performance of a single photon transmission measurement for the ECAT ART. *IEEE Nucl Sci Symp Med Imaging Conf Rec.* 2:1366-1370, 1997.

[47] Kinahan PE, Townsend DW, Beyer T, et al. Attenuation Correction for a Combined 3D PET/CT Scanner. *Med Phys.* 25:2046-2053, 1998.

[48] Xu EZ, Mullani NA, Gould KL, et al. A Segmented Attenuation Correction for PET. *J Nucl Med.* 36:1680-1688, 1991.

[49] Meikle SR, Dahnbom M, Cherry SR: Attenuation correction using count-limited transmission data in positron emission tomography. *J Nucl Med.* 34:143-150, 1993.

[50] Bailey D, Gilardi MC, Grootoonk, et al., Quantitative Procedures in 3D PET in Bendriem B, Townsend DW, eds. *The Theory and Practice of 3D PET.* Kluwer Academic Publishers, Boston, 1998. pp 55-109.

[51] Hoffman EJ, Guerrero TM, Guido G, Digby WM, Dahlbom M. PET system calibrations and corrections for quantitative and spatially accurate images. *IEEE Trans Nucl Sci.* 36:1108-1112, 1989.

[52] Bai B, Li Q, Holdsworth CH, et al. Model-based normalization for Iterative 3D PET Image Reconstruction. *Phys Med Biol.* 47:2773-2784, 2002.

[53] Badawi R, Lodge MA Marsden P. Algorithms for calculating detector efficiency normalization coefficients for true coincidences in 3D PET. *Phys Med Biol*. 43:189-205, 1998.

[54] Casey ME, Gadagkar H, Newport D. A component based method for normalization in volume PET. In: Grangeat P and Amans J-L, eds. *Proceedings of the 3rd International Conference on Fully Three-Dimensional Image Reconstruction in Radiology and Nuclear Medicine,* Aix-les-Bains, 1995. pp. 67-71.

[55] Zaidi H. Comparative evaluation of scatter correction techniques in 3D positron emission tomography. *Eur L Nucl Med.* 27:1813-1826, 2000.

[56] Bergstrom M, Eriksson L, Bohm C, Blomqvist G, Litton j. Correction for scattered radiation in a ring detector positron camera by integral transformation of the projejections. *J Comput Assist Tomogr.* 7:42-50, 1983.

[57] Shao L, Karp JS. Cross-plane scatter correction-point source deconvolution in PET. *IEEE Trans Nucl Med Imaging.* 10:234-239, 1991.

[58] Bailey D, Meikle SR. A convolution subtraction scatter correction method for 3D PET. *Phys Med Biol.* 39:411-424, 1994.

[59] Ollinger JM. Model-based scatter correction for fully 3-D PET. *Phys Med Biol.* 41:153-176, 1996.

[60] Watson CC, Newport D, Casey ME. A single scatter simulation technique for scatter correction. in *3D PET in Three-Dimensional Image Reconstruction in Radiation and Nuclear Medicine*, Kluwer Academic Publishers, Netherlands, 1996. pp. 255-268.

[61] Watson CC. New, faster image-based scatter correction for 3D PET. *IEEE Trans Nucl Sci.* 47:1587-1594, 2000.

[62] Daube-Witherspon ME, Carson RE. Unified deadtime correction model for PET. *IEEE Trans Nucl Med Imaging.* 10:267-275, 1991.

[63] Hoffman EJ, Huang SC, Phelps ME. Quantitation in positron emission tomography: 1. Effect of object size. *J Comput Assist Tomogr.* 3:299-308, 1979.

[64] Hoffman EJ, Huang SC, Plummer D, Phelps ME. Quantitation in positron emission tomography: 6. Effect of nonuniform resolution. *J Comput Assist Tomogr.* 5:987-999, 1982.

[65] Rousset OG, Ma Y, Evans AC. Correction for Partial Volume Effects in PET: Principle and Validation. *J Nucl Med.* 39:904-911, 1998.

[66] Pajevic S, Daube-Witherspoon ME, Bacharach SL, Carson RE. Noise characteristics of 3-D and 2-D PET images. *IEEE Trans Med Imag.* 17:9-23, 1998.

[67] Hoffman EJ, Huang SC, Phelps ME, Kuhl DE, Quantitation in positron emission computed tomography: 4. Effect of accidental coincidences. *J Comput Assist Tomogr.* 5:391-400, 1981.

[68] Badawi R, Marsden PK, Cronin BF, Sutcliffe JL Maisey MN. Optimization of noise-equivalent count-rates in 3D PET. *Phys Med Biol.* 41:1755-1776, 1996.

[69] Karp JS, Kinahan PE, Muehllehner. Effect of increased axial field of view on the performance of a volume PET scanner. *IEE Trans Med Imag.* 12:299-306, 1993.

[70] Reader AJ, Zhao S, Julyan P, Hastings DL, Zweit J. Adaptive correction of scatter and random events for 3D backprojected PET data. *IEEE Trans Nucl Sci.* 48:1350-1356, 2001.

[71] Sashin D, Spinks TJ, Grootoonk S, Jones T. Smoothing of random data to reduce noise in 3D PET. *Conference Record of the 1992 IEEE Nuclear Science Symposium and Medical Imaging Conference.* 3:973-975, 1992.

[72] Hoffman E, Huang S-C, Phelps M, Kuhl D. Quantitation in positron emission computed tomography. 4. Effect of accidental coincidences. *J Comput Assist Tomograph.* 5:391-400,1981.

[73] Casey ME and Hoffman EJ. Quantitation in positron emission computed tomography. 7. A technique to reduce noise in accidental coincidence measurements and coincidence efficiency calibration. *J Comput Assist Tomograph.* 10:845-850,1986.

[74] Badawi R, Miller M, Bailey D, Marsden P. Randoms variance reduction in 3D PET. *Phys Med Biol.* 44:941-954, 1999.

[75] Mumcuoglu EU, Leahy RM, Cherry SR, Zhou Z. Fast gradient-based methods for Bayesian reconstruction of transmission and emission PET images. *IEEE Trans Med Imaging.*13:687-701, 1994.

[76] Mumcuoglu EU, Leahy RM, Cherry SR. Bayesian reconstruction of PET images: Methodology and performance analysis. *Phys Med Biol.* 41:1777-1807, 1996.

[77] Brasse D, Comtat C, Trebossen R, Tararine M, Nguyen QT, Bendriem B. Correction for the Random Coincidences in Dual-Head Gamma Camera Imaging. *IEEE Trans Nucl Sci.* 48:864-871, 2001.

[78] Vandenberghe S, Asseler YD, Koole M, Bouwens L, Van de Walle R, Lemahieu I, Dierckx RA. Randoms correction for gamma camera based PET list-mode reconstruction. *Conference Record IEEE Medical Imaging Conference 2001.* San Diego, CA; 4:2031-2035, 2001.

[79] Smith RJ, Karp JS. A practical method for randoms subtraction in volume imaging PET from detector singles countrate measurements. *IEEE Trans Nucl Sci.* 43:1981-1987, 1996.

[80] Stearns CW, McDaniel DL, Kohlmyer SG, Arul PR Geiser BP, Shanumugan V. Random coincidence estimation from single events rates on the Discovery ST PET/CT scanner. *Proceedings of the 2003 IEEE Nuclear Science Symposium and Medical Imaging Conference.* Portland, OR. IEEE 5:3067-3069, 2003.

[81] Rokitta O, Casey ME, Wienhard K, Pietrzyk. P. Random correction for positron emission tomography using singles counts rates. *Proceedings of the IEEE Nuclear Science Symposium and Medical Imaging Conference.* Lyon, France: IEEE 3: 17/37-17/40, 2000.

[82] Brasse D, Kinahan PE, Lartizien C, Comtat C, Casey M, Michel C. Correction methods for random coincidences in fully 3D whole-body PET: Impact on data and image quality. *J Nucl Med.* 46:859-867, 2005.

[83] Comtat C, Kinahan PE, Defrise M, MIchel C, Townsend DW. Simulating whole-body PET scanning with rapid analytic methods. *Proceedings of the 1999 IEEE Nuclear Science Symposium and Medical Imaging Conference.* Seattle, WA. IEEE 3: 1260-1264, 1999.

[84] for example, Siegel JA, Wu RK, Maurer AH. The buildup factor: Effect on absolute volume determination. *J Nucl Med.* 26:390-394, 1985. and references.

[85] Cherry SR, Dahlbom M, Hoffman EJ. Three dimensional positron emission tomography using a conventional multi-slice tomograph without septa. *J Comput Assist Tomogr.* 15:655-668, 1991.

[86] Jonsson, C and Larsson, SA. A spatially varying Compton scatter correction for SPECT utilizing the integral Klein-Nishina cross section. *Phys Med Biol.* 46:1767-1783, 2001.

[87] Thompson CJ. The problem of scatter correction in positron volume imaging. *IEEE Trans Med Imaging* 12:124-132, 1993.

[88] Sossi V, Krzywinski MI, Cohen P, Mankoff DA, DeRosario J, Ruth TJ. . Effect of count rate on contrast in the ADAC MCD camera. *IEEE Trans Nucl Sci.* 46:1907-1911, 1999.

[89] Sossi V, Pointon B, Boudoux C, et al. NEMA NU-2 2000+ performance measures on an ADAC MCD camera. *IEEE Trans Nucl Sci.* 48:1518-1523, 2001.

[90] Sossi V, Pointon B, Cohen P, et al. Effect of shielding the radioactivity on the outside the field of view on image quality. *IEEE Trans Nucl Sci.* 47:1561-1566, 2000.

[91] Pointon BW and Sossi V. Towards model-based scatter correction for 3D dual head coincidence imaging. *J Nucl. Med.* 44(5):275P, 2003.

[92] Pointon B, Sossi V. Towards model-based randoms correction for 3-D dual head coincidence imaging. *Conference Record IEEE Medical Imaging Conference 2003.*4:2799-2803, 2003.

[93] *read_asipro.m*, © 2003 Raymond F. Muzic, Jr.

[94] Sossi V, Ruth T. Micropet imaging: in vivo biochemistry in small animals. *J Neural Transm* 112:319-330, 2005.

[95] Cherry SR, Shao Y, Silverman RW, Meadors K, Siegel S, Chatziioannou A, Young JW, Jones W, Moyers JC, Newport D, Boutefnouchet A, Farquhar TH, Andreaco M, Paulus MJ, Binkley DM, Nutt R, Phelps ME. MicroPET: a high resolution PET scanner for imaging small animals. *IEEE Trans Nucl Sci.* 44:1161-1166, 1997.

[96] Tai Y C, Chatziioannou A, Siegel S et al. Performance evaluation of the MicroPET P4: a PET system dedicated to animal imaging. *Phys Med Biol.* 46:1845-1862, 2001.

[97] Concorde Microsystems Inc. Micropet Manager, Version 2.2.4.0, 2006.

[98] Concorde Microsystems Inc. ASIPro Version 6.2.5.0., Acquisition, Sinogram and Image Processing™ Version 2.2.4.0, 2006.

[99] Knoess C, Siegel S, Smith A, et. al. Performance evaluation of the MicroPET R4 PET scanner for rodents. *Eur J Nucl Med Mol Imaging.* 30: 737-747, 2003.

[100] Mok S-P, Wang C-H, Chen J-C and Liu R-S. Performance evaluation of the High Resolution Small Animal PET Scanner. *Biomed Eng Appl Basis Comm.* 15:143-149, 2003.

[101] Weber S and Bauer A. Small animal PET: aspects of performance assessment. *Eur J Nucl Med Mol Imaging.* 31:1545-1555, 2004.

[102] Bailey DL, Jones T, Spinks TJ. A method for measuring the absolute sensitivity of positron emission tomographic scanners. *Eur J Nucl Med.* 18:374–379, 1991.

[103] Goertzen A, Suk JY, Thompson C.J On the imaging of very weak sources in an LSO PET scanner. *Conference Record IEEE Medical Imaging Conference 2006.* to be published.

[104] Andrew Goertzen, Private communication.

[105] Attenuation coefficient and relative scatter probabilities are taken from SimSET data. See Kaplan MS, Harrison RL Vannoy SD. Coherent scatter implementation in SimSET. *IEEE Trans Nucl Sci.* 45:3064-3068, 1998.

[106] David Bailey, Siemen's Pre-clinical solutions, private communication, 2005.

[107] Harrison RL, Haynor DR, Gillispie SB, Vannoy SD, Kaplan MS, Lewellen TK. A public-domain simulation system for emission tomography: photon tracking through heterogeneous attenuation using importance sampling. *J Nucl Med.* 34:60P, 1993.

[108] Jan S, Santin G, Strul D, et al. GATE: a simulation toolkit for PET and SPECT. *Phys. Med. Biol.* 49:4543-4561, 2004.

[109] Eric Vandervoort, personal communication.

[110] Badawi RD, Kohlmeyer SG, Harrison RL, Vannoy SD, Lewellen TK. The effect of camera geometry on singles flux, scatter fraction, and trues and randoms sensitivity for cylindrical 3D PET – a simulation study. *IEEE Trans Nucl Sci.* 47:1228-1232, 2000.